Studying the effect of boundary layer suction

using design tools based on finite difference and integral methods

March 14, 2012

Nico C.A. van den Berg

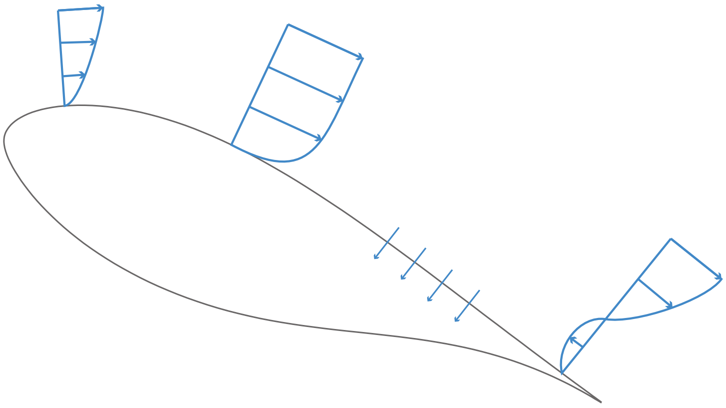

Delft University of Technology

Studying the effect of boundary layer suction

using design tools based on finite difference and integral methods

Master of Science Thesis

For obtaining the degree of Master of Science in Aerospace Engineering
at Delft University of Technology

Nico van den Berg

March 14, 2012

Faculty of Aerospace Engineering · Delft University of Technology

Delft University of Technology

DELFT UNIVERSITY OF TECHNOLOGY
FACULTY OF AEROSPACE ENGINEERING
AERODYNAMICS CHAIR

The undersigned hereby certify that they have read and recommend to the Faculty of Aerospace Engineering for acceptance the thesis entitled **"Studying the effect of boundary layer suction"** by **Nico van den Berg** in fulfillment of the requirements for the degree of **Master of Science**.

Dated: March 14, 2012

Supervisors:

prof. dr. ir. drs. H. Bijl

prof. dr. ir. J.L. van Ingen

dr. ir. L.L.M. Veldhuis

dr. ir. B.W. van Oudheusden

ir. R. Campe

Abstract

With the increasing interest for renewable energy resources in the last couple of decades, the possible benefits of flow control is brought under more and more attention. Boundary layer suction (or blowing) is one type of control that has proven its applicability in various fields. Being able to predict these effects on the boundary layer and airfoil properties can save both money and time in early design stages. At the moment, this prediction is still unsatisfactory and not well validated. This is especially true for turbulent boundary layers with suction. For this reason, the main objective is to provide new ways to model boundary layer suction on airfoils by using different computational techniques. Next to this, the results should be compared with other design tools as well as with analytical and experimental data for validation.

To succeed in the objectives, the finite difference approach as used in the book series of professor Cebeci has been modified to model boundary layer suction. Solving the boundary layer equations by using finite difference techniques instead of integral methods provide more flexibility and less empirical closures. To simulate boundary layer suction and its effects on the boundary layer and airfoil properties, a panel method (inviscid) is coupled with the boundary layer calculation. The corrections for mass transfer at the wall include a different wall boundary condition, another transition prediction method, corrections to the turbulence model and several changes to the output relations (displacement thickness and drag coefficient). This led to the development of the design tool ACTITRANS2D that is capable of predicting the effect of a certain mass transfer distribution.

From a comparison of ACTITRANS2D with analytical laminar flat plate results it can be seen that the tool works good for laminar flows with or without suction. The possible turbulence models are hard to validate since it is difficult to approximate the conditions at which the turbulent flat plate measurements were performed. From analysis of airfoils with various surface mass transfer distributions it can be seen that suction can indeed have significant benefits, dependent on the goal that is pursued. By comparing with the measurement data on the AF 0901 profile, it can be observed that ACTITRANS2D can qualitatively predict the effect of a certain mass transfer distribution although absolute values can be different.

In essence, a new design tool became available that is capable of predicting the effect of boundary layer suction on airfoil and boundary layer properties. To provide better validation, it would be useful to perform measurements on a turbulent flat plate boundary layer with and without suction. Furthermore, the case where the boundary layer becomes separated from

the surface can not be modeled well. This because the boundary layer equations are not valid anymore and convergence can not be achieved. To see what happens in these cases, other computational techniques should be used. This could be RANS, LES or even DNS to see the effect of suction on the flow structure. However, this will open a relatively new research area of which little is known yet.

Preface

This work is the final part to obtain a Master of Science degree at the Delft University of Technology. The report presents the work performed during my thesis study carried out in close cooperation with Actiflow B.V. under supervision of dr. ir. L.L.M. Veldhuis and dr. ir. B.W. van Oudheusden. It concerns a study to model and predict the effect of boundary layer suction by using different computational techniques.

Already at early age I got fascinated by the beauty of flight. Probably encouraged by the hot air balloon launch site near my parents house or the holidays by airplane. At high school it became clear that studying aerospace engineering at the Delft University of Technology suited my interests best. Now, after five and a half years of study I am writing my last words as an aerospace engineering student with both relief and satisfaction. A great time in Delft has come to an end and new challenges are about to be faced. Without the help and support of my parents, friends and girlfriend, this would definitely be a lot harder. **Thank you all**.

There are two other parties that need to be thanked for making this research possible. First of all, on the Actiflow B.V. side, Eric Terry and Roy Campe for giving me the opportunity, freedom and resources to perform my thesis research. Furthermore I would like to thank all my colleagues (Roland, Tim, Tom, Gael, Vincent, Oscar, Jeroen, Marieke, Wieteke and Rahul) for providing a pleasant working environment.
At the Delft University of Technology side, the meeting group composed of prof. dr. ir. J.L. van Ingen, dr. ir. L.L.M. Veldhuis, dr. ir. B.W. van Oudheusden, ir. L.L.M. Boermans and ir. R. Campe, for the fruitful discussions we had that gave me a lot of new ideas and insights.

Nico van den Berg
Breda, February 23, 2012

Table of contents

Abstract i

Preface iii

Nomenclature vii

List of figures xiii

List of tables xv

1 Introduction 1
- 1.1 Background 1
- 1.2 Boundary layer suction 3
- 1.3 Motivation 5
- 1.4 Synopsis 6

2 Potential flow computation 7
- 2.1 Theory 7
- 2.2 Panel methods and exact solutions 10

3 Boundary layers with mass transfer 15
- 3.1 In the footsteps of Ludwig Prandtl 15
- 3.2 Defining the boundary layer 17
- 3.3 Boundary layer equations 20
- 3.4 Solution strategies 22
  - 3.4.1 Finite difference method 22
  - 3.4.2 Integral techniques 26
  - 3.4.3 Standard and inverse methods 29
  - 3.4.4 Viscous effects in potential method 31
- 3.5 Transition methods 34
- 3.6 Modeling the eddy viscosity 36
- 3.7 Sink drag 40
  - 3.7.1 A separate drag? 40
  - 3.7.2 General 42

4 Code architecture ActiTrans2D 43
4.1 Airfoil specification . . . 44
4.2 Panel method . . . 44
4.3 Interface function . . . 44
4.4 Boundary layer calculation . . . 44
4.5 Viscous effects . . . 44
4.6 Relaxation . . . 45
4.7 Output . . . 45

5 Flat plate validation 47
5.1 Laminar flat plate . . . 47
5.2 Turbulent flat plate . . . 52

6 Airfoils with transpiration 57
6.1 Effect transpiration distributions: NACA 0012 . . . 57
6.1.1 Case description . . . 57
6.1.2 Results . . . 59
6.1.3 Discussion . . . 66
6.1.4 Convergence and wake velocity profiles . . . 68
6.2 Test case: NACA 4418 . . . 70
6.2.1 Case description . . . 70
6.2.2 Boundary layer characteristics . . . 71
6.2.3 Pressure coefficient distribution . . . 74
6.2.4 Convergence . . . 75
6.3 Test case: AF 0901 . . . 77
6.3.1 Case description . . . 77
6.3.2 Airfoil properties . . . 78
6.3.3 Boundary layer properties . . . 81
6.4 Test case: FFA-W3-241 . . . 84
6.4.1 Case description . . . 84
6.4.2 Airfoil properties . . . 85

7 Conclusions and recommendations 89

A Block Diagrams Code Structure 93

B NACA Body Creation and Repaneling 97

C Hess−Smith panel method 101

D Conformal Mapping 103

E Momentum Integral Equation with Mass Transfer 107

F Asymptotic Suction Laminar Flat Plate 109

Bibliography 111

Nomenclature

Abbreviations

AF	Actiflow
BLS	Boundary layer suction
CFD	Computational fluid dynamics
DNS	Direct numerical simulation
FFA	Swedish institute for aeronautic research
LES	Large eddy simulation
NACA	National advisory committee for aeronautics
OPEC	Organization of petroleum exporting countries
RANS	Reynolds averaged navier stokes

Greek symbols

α	Angle of attack	[°]
γ	Intermittency factor	[–]
δ	Boundary layer thickness	[m]
δ^*	Displacement thickness	[m]
η	Similarity variable	[–]
θ	Momentum thickness	[m]
κ	von Kármán constant	[–]
μ	Dynamic viscosity	[kg/ms]
ν	Kinematic viscosity	$[\mathrm{m}^2/\mathrm{s}]$

ν_t	(Kinematic) eddy viscosity	$[\mathrm{m}^2/\mathrm{s}]$
ξ	Dimensionless x−coordinate	$[-]$
ρ	Density	$[\mathrm{kg}/\mathrm{m}^3]$
τ	Shear stress	$[\mathrm{N}/\mathrm{m}^2]$
ψ	Stream function	$[\mathrm{m}^2/\mathrm{s}]$

Latin symbols

C_d	Two dimensional drag coefficient	$[-]$
C_{d_s}	Sink drag coefficient	$[-]$
C_f	Skin friction coefficient	$[-]$
C_l	Two dimensional lift coefficient	$[-]$
C_q	Suction flow coefficient	$[-]$
F	Dimensionless suction velocity	$[-]$
f	Dimensionless stream function	$[-]$
H	Shape factor	$[-]$
h	Distance	$[\mathrm{m}]$
k^+	Roughness Reynolds number	$[-]$
l	Mixing length	$[\mathrm{m}]$
M	Mach number	$[-]$
m	Pressure gradient parameter	$[-]$
N	Number of panels	$[-]$
p	Pressure	$[\mathrm{N}/\mathrm{m}^2]$
Re	Reynolds number	$[-]$
u,v	Velocity components in x− and y−direction	$[\mathrm{m}/\mathrm{s}]$
x,y	Cartesian coordinates	$[\mathrm{m}]$
y^+	Wall coordinate viscous sublayer	$[-]$
v_w	Transpiration velocity	$[\mathrm{m}/\mathrm{s}]$

Indices

∞	At infinity
e	At the edge of the boundary layer
l	Lower
te	At the trailing edge
tr	At boundary layer transition
u	Upper
w	At the wall

Other

$+$	Wall units
$-$	Averaged quantity
$'$	Fluctuation quantity

List of figures

1.1 Relation flow control goals. Based on Gad-el-Hak [2000]. 2
1.2 Application boundary layer suction on wind turbine blades. From Birsanu [2011]. 2
1.3 Prandtl's slotted cylinder. From Terry [2004]. 3
1.4 Evolution boundary layer suction. From Campe [2004]. 4
1.5 Report road map. 6

2.1 Panel distribution on the airfoil surface (from Cebeci [1999]). 8
2.2 Airfoil and wake paneling including singularity distributions as well as a trailing edge zoom (from Drela [1989b]). 9
2.3 Pressure coefficient distribution airfoil I at $\alpha = 8^o$. 11
2.4 Pressure coefficient distribution airfoil II at $\alpha = 12^o$. 11
2.5 Inviscid lift polar both airfoils. 12
2.6 Lift coefficient convergence. Airfoil II at $\alpha = 8^o$, number of panels varied. . 13

3.1 Boundary layer close to separation. Taken from a translation of the famous Prandtl 1904 paper – Prandtl [1904]. 15
3.2 Interpretation inviscid and viscid case. 17
3.3 Displacement and momentum thickness (from White [2006]). 18
3.4 Boundary layer condition. 18
3.5 Bubble (left) and computation (right) from Veldman [2010]. 29
3.6 Including viscous effects. 31
3.7 Closing the finite trailing edge. 33
3.8 Wazzan's transition prediction. 35
3.9 Two turbulent eddies travelling through a flow field. Based on Pope [2000]. . 36
3.10 Schematic division turbulent boundary layer. 37
3.11 Control volume situation I. 41
3.12 Control volume situation II. 41

4.1 Main code architecture. 43

5.1 Laminar flat plate displacement thickness distribution. 48
5.2 Laminar flat plate momentum thickness distribution. 48
5.3 Laminar flat plate shape factor distribution. 49
5.4 Laminar flat plate skin friction coefficient distribution. 49
5.5 Laminar flat plate velocity profiles. 50

5.6 Laminar flat plate shape factor distribution. Increased number of panels. . . . 51
5.7 Velocity profile comparison between ACTITRANS2D and McQuaid [1967] – Smooth flat plate, $k^+ = 0$. 53
5.8 Velocity profile comparison between ACTITRANS2D and McQuaid [1967] – Transitionally rough flat plate, $k^+ = 30$. 53
5.9 Velocity profile comparison between ACTITRANS2D and McQuaid [1967] – Fully rough flat plate, $k^+ = 90$. 54
5.10 Velocity profile comparison between ACTITRANS2D and Favre et al. [1961]. . 55
5.11 Skin friction comparison between ACTITRANS2D and theory. 56

6.1 Pressure coefficient distribution and NACA 0012 geometry. 59
6.2 Displacement thickness. Constant region, increased turbulent suction block. . 60
6.3 Momentum thickness. Constant region, increased turbulent suction block. . . 60
6.4 Skin friction coefficient. Constant region, increased turbulent suction block. . 61
6.5 Displacement thickness. Varying region, constant turbulent suction block. . . 61
6.6 Momentum thickness. Varying region, constant turbulent suction block. . . . 62
6.7 Skin friction coefficient. Varying region, constant turbulent suction block. . . 62
6.8 Displacement thickness. Varying region, constant laminar suction block. . . . 63
6.9 Momentum thickness. Varying region, constant laminar suction block. 63
6.10 Skin friction coefficient. Varying region, constant laminar suction block. . . . 64
6.11 Displacement thickness. Slot suction block. 64
6.12 Momentum thickness. Slot suction block. 65
6.13 Skin friction coefficient. Slot suction block. 65
6.14 Convergence history. $R_e = 3 \cdot 10^6$, $\alpha = 6^o$, 240 panels (total). 69
6.15 Wake velocity profiles. $R_e = 3 \cdot 10^6$, $\alpha = 0^o$, 200 panels (total). 69
6.16 Boundary layer velocity profiles at several locations on the upper surface. . . . 71
6.17 Displacement thickness comparison upper surface. 72
6.18 Momentum thickness comparison upper surface. 72
6.19 Shape factor comparison upper surface. 73
6.20 Skin friction coefficient comparison upper surface. 74
6.21 Pressure coefficient comparison. 75
6.22 Convergence history. $R_e = 6 \cdot 10^6$, $\alpha = 8^o$, 240 panels (total). 76
6.23 Three dimensional view AF 0901. From Bink [2010]. 77
6.24 Lift coefficient curve AF 0901 – Clean configuration. 79
6.25 Drag coefficient curve AF 0901 – Clean configuration. 79
6.26 Lift-drag polar AF 0901 – Clean configuration. 80
6.27 Lift coefficient curve AF 0901 – fixed transition upper side. 81
6.28 Boundary layer velocity profiles at several locations on upper surface. 82
6.29 Shape factor comparison upper surface. 82
6.30 Skin friction coefficient comparison upper surface. 83
6.31 Pressure coefficient comparison. 83
6.32 Geometry comparison AF 0901 versus FFA-W3-241. 85
6.33 Lift coefficient curve FFA-W3-241. 85
6.34 Drag coefficient curve FFA-W3-241. 86
6.35 Lift-drag polar FFA-W3-241. 87

A.1 Airfoil configuration block. 93
A.2 Panel method architecture. 93
A.3 Interface block. 94
A.4 Boundary layer method. 94
A.5 Include viscous effects. 95
A.6 Relaxation principles. 95
A.7 Output parameters. 95

B.1 NACA 4412 including camber line discretized with equally spaced segments. . 98
B.2 NACA 23012 including camber line discretized with equally spaced segments. 98
B.3 Influence the NACA 4418 geometry after creating zero trailing edge thickness. 99
B.4 Half cosine distribution on a NACA 4418 profile. 99
B.5 NACA 4418 profile with 100 panels. 100

D.1 Cylinder parameters in $\zeta-$plane that is mapped to an airfoil in the $Z-$plane (Masatsuka [2009]). 105

List of tables

2.1 von Kármán—Trefftz airfoil parameters 10
2.2 Indication of the relative error (E) in percent between the exact lift coefficient and the panel methods from XFOIL and ACTITRANS2D. Left table represents airfoil I and right table airfoil II. 13

3.1 Laminar boundary layer. 18

6.1 Case description 57
6.2 Lift coefficient, drag coefficient and transition location for various transpiration distributions. 66
6.3 Case description 70
6.4 Case description 78
6.5 Case description 84

CHAPTER
ONE

Introduction

With the rising quest for renewable sources of energy in the last couple of decades, the topic of flow control is brought under more and more attention. This thesis research investigates a certain type of flow control – boundary layer control.
The aim of the first chapter is to get more acquainted with this subject and to place the research in a certain context. To start, some background information will be present and the technique of boundary layer suction (BLS) will be covered. After this, the motivation for this thesis research will be highlighted and the structure of the report will be explained.

1.1 Background

To place this thesis research in a certain context, it is necessary to provide some background information. This will be the topic of section 1.1.

Flow control

First of all, BLS can be considered as a type of flow control. Flow control can be defined as about everything we do to manipulate the flow – Veldhuis [2010]. Its goals are often strongly related and compromises should be made frequently. A schematic can be seen in figure 1.1. Generally, BLS is used for two purposes – keeping the flow laminar by postponing transition and to avoid or delay separation.
The main driver behind flow control is probably best described by the following sentence:

> *The potential benefits of realizing efficient flow control systems range from saving billions of dollars in annual fuel costs for land, air and sea vehicles to achieving economically and environmentally more competitive industrial processes involving fluid flows.*
>
> **Mohamed Gad-el-Hak**

With this in mind, Actiflow B.V. is brought into play. Its research on BLS is the topic of the next paragraph.

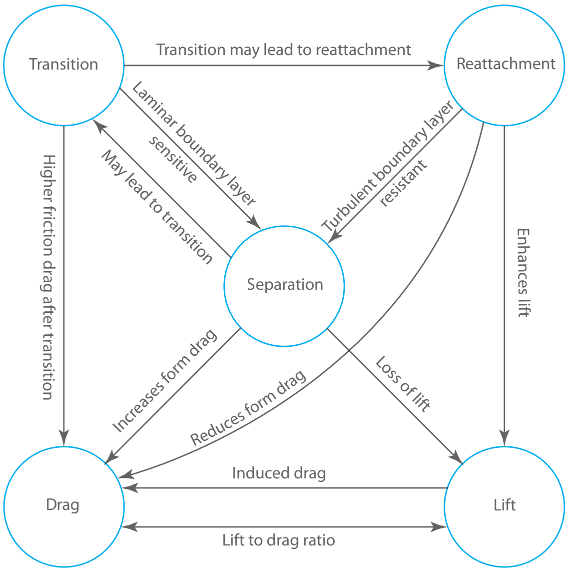

Figure 1.1: Relation flow control goals. Based on Gad-el-Hak [2000].

Actiflow research

Actiflow B.V.[1][2] was started with the main intention to apply active flow control techniques to improve performance of aerodynamic bodies. Since then, a wide range of applications with boundary layer suction were developed. Some examples include a special diffuser on the Ferrari 599X to generate extra down force and the implementation of a suction device in a large wind tunnel to remove the disturbing effects caused by the wall presence on the main flow. Even the possibility to apply BLS on sailboats has been investigated. This experience together with the global demand for innovative solutions in wind energy led to the wind turbine project. Since 2007, the company started with the focus on the design of newly shaped wind turbine blades with boundary layer suction. They even obtained a European patent on it (number WO2009054714 or EP2053240). In short, this patent contains a way of applying passive suction on wind turbine blades by using centrifugal forces. Passive suction was chosen

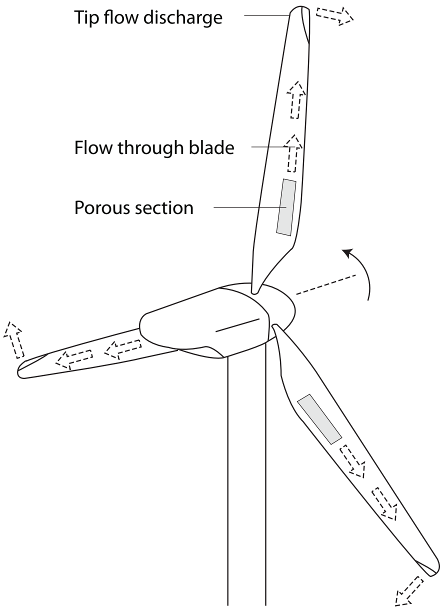

Figure 1.2: Application boundary layer suction on wind turbine blades. From Birsanu [2011].

---

[1] Actiflow B.V., founded in 2005 as a spin off company of the Delft University of Technology, is specialized in combining aerodynamics and product design. Its customers vary from large multinationals to small start up companies where the served industries range from the building industry to the medical industry, from automotive to aerospace and from oil and gas to wind energy.

[2] **Actiflow B.V.** | Zinkstraat 22 | 4823AD Breda | The Netherlands | Telephone: +31 (0) 765 422 220 | Fax: +31 (0) 765 411 788 | Email: contact@actiflow.com | www.actiflow.com.

due to its simplicity, the relatively low maintenance required and the fact that there is no need for costly systems such as fans and actuators.
In order to improve the aerodynamic performance, boundary layer suction is applied on the blade suction side where separation can be postponed by removing the low momentum flow in the boundary layer. A schematic overview of the application can be seen in figure 1.2.
Within this framework, Actiflow B.V. performed wind tunnel tests on a newly designed profile[3] to proof the working concept of BLS on a wind turbine blade.

1.2 Boundary layer suction

Controlling the boundary layer by means of suction is not new. Ludwig Prandtl already used the concept in 1904 on a slotted cylinder as seen in figure 1.3. In this experiment, a cylinder was used with a small slot at about 45^o from the vertical. Through this slot, air was sucked away to show that the flow could be attached longer to the upper surface. Although Prandtl used suction to prevent flow separation, it took about four decades until the first experiments were performed to delay transition.

Figure 1.3: Prandtl's slotted cylinder. From Terry [2004].

In this section, the fundamentals, history and fields of application will shortly be covered.

Fundamentals

In general, by applying suction through the surface, the boundary layer becomes more stable. This can be seen from the laminar boundary layer equation by writing it at the wall with a vertical velocity component and using the fact that the no slip condition remains valid:

$$u\frac{\partial u}{\partial x} + v\frac{\partial u}{\partial y} = -\frac{1}{\rho}\frac{\partial p}{\partial x} + \nu\frac{\partial^2 u}{\partial y^2}$$

$$v_w\frac{\partial u}{\partial y} + \frac{1}{\rho}\frac{\partial p}{\partial x} = \nu\frac{\partial^2 u}{\partial y^2} \qquad \text{for suction: } v_w < 0$$

Hence, using suction stimulates a more convex and more stable laminar boundary layer as well as counteracting the effect of an adverse pressure gradient. Note that in deriving the boundary layer equations (section 3.3), the vertical velocity component is assumed to be small $O\left(\frac{1}{\sqrt{Re}}\right)$. To let the outer flow be independent of v_w, a same order of magnitude should be assumed.
The purpose of using suction in a laminar boundary layer is mainly to decrease the drag of an object. Transition can be delayed and hence the friction drag can be reduced significantly. Furthermore, the displacement thickness is reduced and laminar separation can be avoided (reducing the form drag – the pressure drag due to flow separation).
In a turbulent boundary layer, suction is mainly used to increase the maximum lift coefficient by postponing separation. Note that by using suction, the boundary layer becomes thinner

---

[3] AF 0901 profile designed by Zwang [2009].

and a 'more inviscid' case is reached. Again, the form drag can be reduced by delaying separation but the friction drag will go up due to the larger velocity gradient near the wall. Important to point out is that the possible savings by using BLS do not come for free. By removal of the fluid, a momentum flux is removed from the flow leading to an additional drag called the sink drag. A description of this drag is found in section 3.7.

History

In figure 1.4, the evolution of BLS throughout history can be seen. Note that it is assumed that it all started with the experiment of Ludwig Prandtl back in 1904. Since then, numerous airplanes were equipped with a boundary layer suction device. It took until 1990 to demonstrate its use on a transport jet aircraft. An interesting observation can be made in the timespan 1960-1985. In the sixties, the relatively low price for aviation fuel and the high costs for installing suction devices led to a period where the research on flow control was down. Later on, research on boundary layer suction revived due to the higher fuel costs that resulted from the OPEC oil embargo and the increased environmental awareness. The research became more important due to the possible gains in aerodynamic performance.
In time, the technological advancement has increased due to the arrival of new materials, better design methods and production techniques.

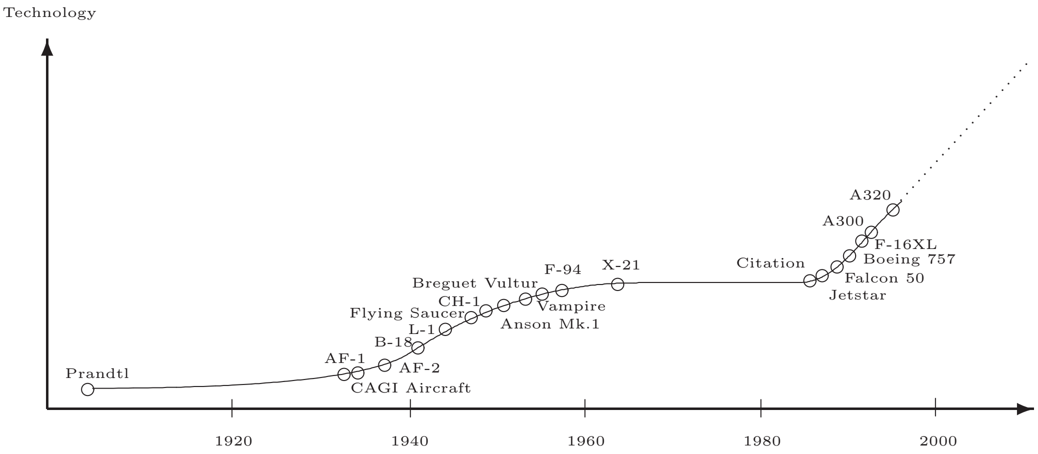

Figure 1.4: Evolution boundary layer suction. From Campe [2004].

Fields of application

Due to the possible gains of using BLS, it is of interest in several fields. Some of them will be highlighted in this paragraph together with a short introduction.

- **Race cars**: More downforce possible at the front and rear wing by delaying or avoiding separation.
- **Wind turbines**: High maximum lift coefficient attainable that is important at the inboard region of a blade since it may reduce the blade area. To maximize the power, a high value for the lift over drag ratio should be obtained which can be achieved by using suction.

- **Commercial aircraft**: Better aerodynamic performance leading to a larger range and higher capacity. The fuel costs will drop but the maintenance costs will increase.
- **Military aircraft**: By the possibility to delay stall, better manoeuvrability can be achieved and steeper turns can be taken. Also the runway length to take off can be reduced.
- **Wind tunnels**: In most wind tunnels, the air is moving around a fixed object, in reality, an object moves through the air. At the walls of this wind tunnel, a boundary layer can develop which would not be there in reality. To minimize the effect of it by suppressing this boundary layer, a suction device could be installed on the walls.

1.3 Motivation

Being able to predict the effect of a certain suction distribution on the airfoil properties is of great importance for both industry and the academic world. A lot of money and time can be saved if design tools are available that are able to reasonably predict the effect of boundary layer suction. Using these tools, the advantages and disadvantages of a certain distribution will get to the surface in an early design stage without the need to perform extensive wind tunnel tests.

At the moment, the effect of boundary layer suction is modeled by using integral techniques to calculate the boundary layer (XFOIL, MSES and other related tools). As this may work fine for laminar boundary layers, it is known that the formulation for a turbulent boundary layer (with or without mass transfer) is still questionable. This mainly result from the fact that empirical closure relations are needed to close the set of (ordinary differential) equations.

With this in mind, a new strategy is chosen to model boundary layer mass transfer. In this thesis research, a finite difference method – based on the approach of the Cebeci[4] book series – will be used to simulate this effect and to compare it with the integral techniques. In general, finite difference methods offer more flexibility than integral methods by solving the boundary layer equations directly in their partial differential form at the cost of more computational time.

By extending the approach of prof. Cebeci for mass transfer, ACTITRANS2D is born. To verify the credibility of the tool and if the adjustments are implemented well, it is validated by comparing it with flat plate results (analytical and experimental), airfoil wind tunnel data and RFOILSUCV2 (based on integral techniques corrected for mass transfer). It has to be noted that measurement data is scarce, especially for turbulent boundary layers with suction.

The aim of this thesis research is to study the effect of boundary layer suction on the boundary layer and airfoil properties as well as to create a valuable alternative to current design tools. This thesis research should bring us a step further in the understanding and prediction of applying boundary layer suction (or blowing) on airfoils.

Next to this, an important driver for this thesis research is the author's personal interest in this exciting branche of fluid dynamics.

---

[4] Distinguised alumnus at the NC state university. Received his doctorate in Mechanical Engineering in 1964 and received numerous awards including fellow of the American Institute of Aeronautics and Astronautics. He also received the presidential science award from Turkey. His research concerns boundary layer computation, turbulence modeling and interaction of viscid and inviscid flows. In short, a respected person in the fluid dynamics community with more than fourty years of experience.

1.4 Synopsis

This thesis report is composed of seven chapters of which the introduction is the first. To organize the contents in the mind of the reader, a report road map is attached and can be found in figure 1.5. The contents of the successive chapters is shortly outlined below.

- **Chapter two:** Description of panel methods to compute the potential flow together with a comparison to exact theory.
- **Chapter three:** Covers ways to compute the boundary layer with mass transfer.
- **Chapter four:** A brief description of the design tool ACTITRANS2D by explaining the code architecture and a short note to each element.
- **Chapter five:** Contains a validation with respect to flat plate results to check the implementations in ACTITRANS2D.
- **Chapter six:** Simulation of several airfoils with boundary layer suction. It contains a comparison between measurement data, ACTITRANS2D and RFOILSUCV2.
- **Chapter seven:** Conclusions of the present study and recommendations for further research will be given.

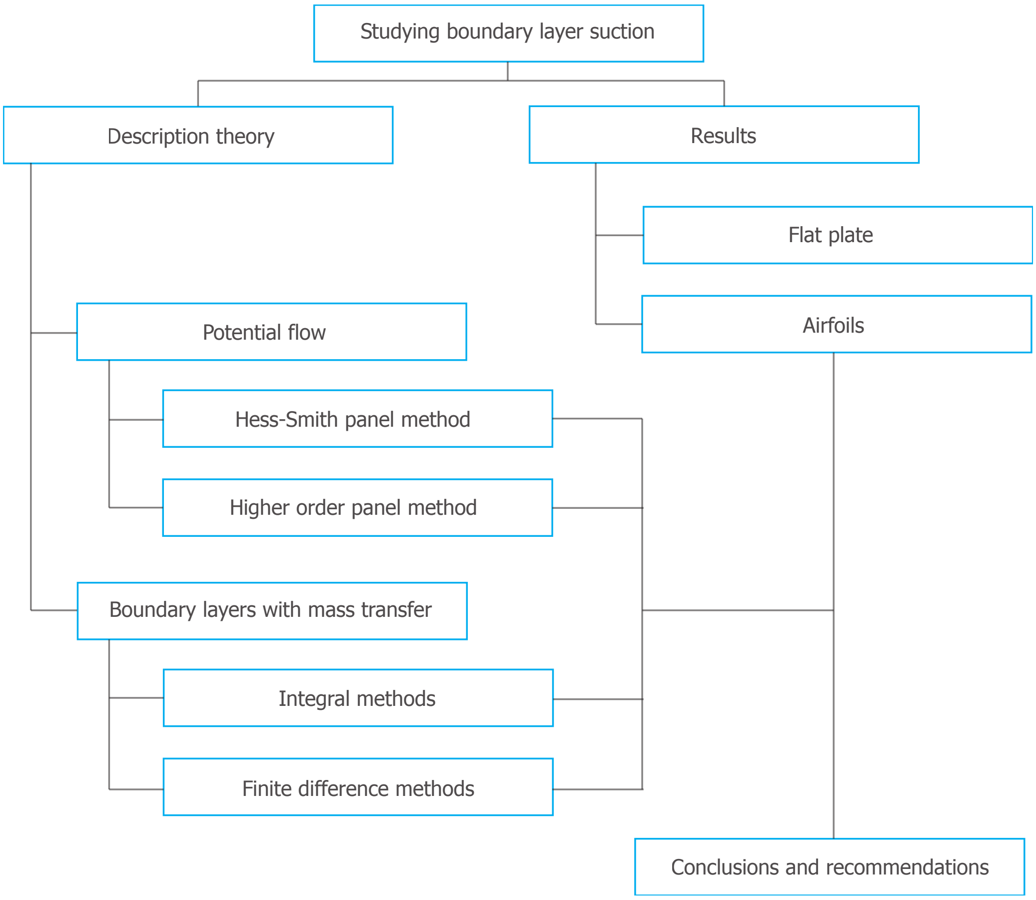

Figure 1.5: Report road map.

CHAPTER
TWO

Potential flow computation

In the past, numerous variations in panel methods have been developed, each with its own strengths and weaknesses. In general, things that vary between each method are the type of panels (flat, parabolic or different), singularity distribution (sources, doublets or vortices) and the boundary condition (body surface is streamline – set streamfunction constant (Dirichlet) or impose zero normal velocity (Neumann)).

Methods with constant singularity distribution (on each panel) are usually referred to as 'low-order methods' and linearly (or higher order) singularity distributions on each panel are often called 'high-order methods'. A large variety of options exist between the methods. The Hess–Smith panel method is a classical one and developed around 1960-1970. It makes use of flat panels, constant source distribution on each panel and a constant vortex strength on the complete airfoil to satisfy the Kutta condition. A concise description can be found in section 2.1.

The reason that it is used in the code ACTITRANS2D is because of its simplicity and flexibility to extend it with viscous effects through a transpiration model. Also, much literature is available for this panel method and some examples of FORTRAN or MATLAB programs are available on the web or in books. This method is clearly a 'low-order method' and a study on the accuracy versus a 'high-order method' (from XFOIL) and exact theory is available in section 2.2. Using this comparison, useful things about the accuracy between the different panel method types can be said and critical regions can be indicated.

2.1 Theory

This section will describe the panel methods that are used in ACTITRANS2D and XFOIL in a concise matter. It assumes that the reader has some basic knowledge about elementary flows as described in Anderson [2007] chapter 3.

Hess–Smith

In this method, the airfoil contour is represented by a finite number of straight line elements. This is represented in figure 2.1. In this method, the velocity in each point is composed of the uniform flow and the disturbance due to the source and vortex flows imposed on the surface.

The crux of the method is to let the body be a streamline in the total flow. This means:

$$\psi = \text{constant} \qquad \text{or} \qquad \frac{\partial \phi}{\partial n} = 0 = \text{zero normal velocity} \tag{2.1}$$

To solve the Laplace equation with this approach, the normal and tangential velocities are computed at each control point (mid panel) by summation of all induced velocities from the sources (q_j) and vortices (τ_j) at all panels. By using the flow tangency condition (zero normal velocity in the control point) and the fact that in the Hess–Smith panel method the source strength is assumed to be constant over each panel and the vorticity strength is constant on all panels, one can write the system as (Cebeci et al. [2005a]):

$$\sum_{j=1}^{N} A_{ij}^{n} q_j + \tau \sum_{j=1}^{N} B_{ij}^{n} + V_\infty \text{sin}\,(\alpha - \theta_i) = 0 \qquad i = 1, 2, ..., N \tag{2.2}$$

For a detailed description of all terms, see appendix C. The Kutta condition is implied by assuring that the flow is leaving the airfoil smoothly. Because the normal velocity is set to zero, this constraint reduces to setting the tangential velocities at the trailing edge equal to each other.
Using the above relations and the Kutta condition, the system can be written in matrix format as:

$$A\mathsf{x} = \mathbf{b} \tag{2.3}$$

where x contains the unknown panel source strengths and vorticity strength. This system can be solved by using built in MATLAB routines. For a detailed description, one is referred to appendix C.

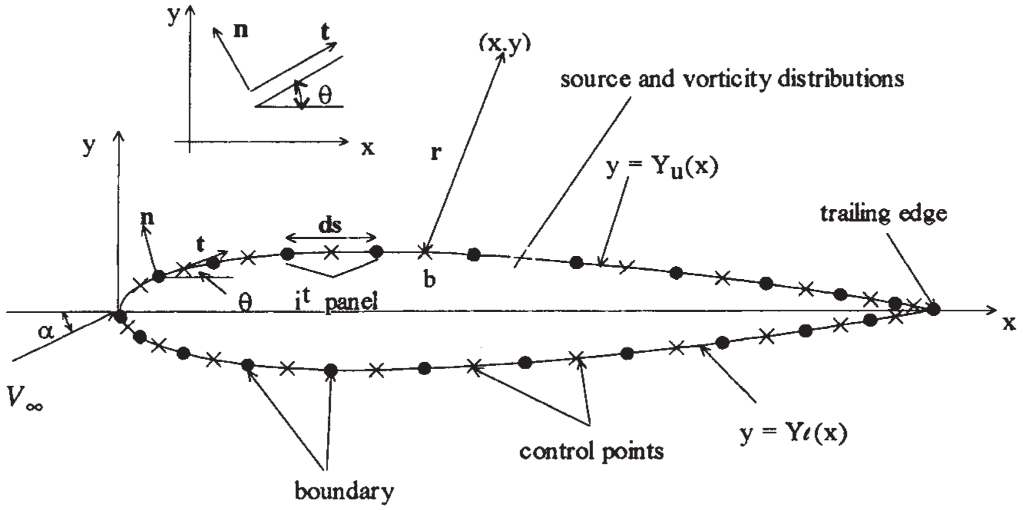

Figure 2.1: Panel distribution on the airfoil surface (from Cebeci [1999]).

XFOIL

In XFOIL, the inviscid flow is computed by superimposing of uniform flow, a vortex sheet of strength γ on the airfoil surface and a source sheet of strength σ on the airfoil surface and wake. Using the source sheet, viscous effects can be modeled by using a transpiration model.

Using this idea and the description of these elementary flows as described in Anderson [2007] chapter 3, the streamfunction can be written as equation 2.4. Here, s is the coordinate along the source or vortex sheet, (x, y) are the coordinates of a point and r is the magnitude of the vector between s and (x, y). Furthermore, θ is the angle of vector r and u_∞ and v_∞ are the velocity components of the free stream velocity.

$$\psi(x, y) = u_\infty y - v_\infty x + \frac{1}{2\pi}\int \gamma(s) \ln r(s; x, y)\, \mathrm{ds} + \frac{1}{2\pi}\int \sigma(s)\, \theta(s; x, y)\, \mathrm{ds} \tag{2.4}$$

The wake trajectory and airfoil contour are discretized in flat panels. N on the airfoil and N_w in the wake. Each panel thus has a linear vorticity distribution and a constant source strength (and hence it is called a 'high-order method'). A schematic can be seen in figure 2.2.

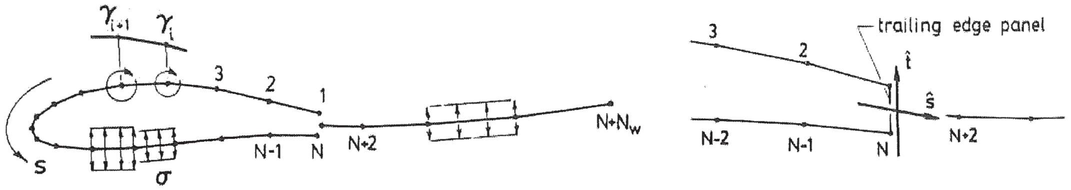

Figure 2.2: Airfoil and wake paneling including singularity distributions as well as a trailing edge zoom (from Drela [1989b]).

To model a finite trailing edge, an extra panel with uniform source and vortex strength is placed across the trailing edge (see figure 2.2). Discretizing equation 2.4 and applying the Kutta condition $(\gamma_1 + \gamma_N = 0)$ yields a linear $(N + 1)$ x $(N + 1)$ system that can be solved for the unknown singularity strengths.

2.2 Panel methods and exact solutions

An elegant way to validate the Hess–Smith panel method implementation is by comparing it with analytical results based on conformal mapping. Strictly speaking, a conformal map is a transformation between two domains with angle preservation. Usually, a mapping function between two complex planes is considered.

In appendix D, the conformal mapping theory will be explained and in this section, a comparative study will be performed between the exact theory and the panel methods used in XFOIL and ACTITRANS2D.

In the conformal mapping technique, a solution for lifting cylinder flow is created by superimposing a doublet, uniform and vortex flow in a complex plane. By translation of the cylinder in the complex plane and making use of a proper transformation, potential flow solutions for certain types of airfoils can be reconstructed.

The von Kármán–Trefftz transformation will be applied that is able to specify a finite trailing edge angle. This will lead to more realistic airfoils as opposed to the Joukowsky transformation (special case of the von Kármán–Trefftz transformation) where only cusped trailing edge airfoils can be analyzed.

Using the relations from appendix D, a MATLAB program has been set up that determines the airfoil properties and compares it with the results from the inviscid panel methods from XFOIL and ACTITRANS2D. This comparison will be the topic of the next paragraph.

Comparative study

To create a comparison between the exact theory as described in appendix D and the panel methods from XFOIL (high order) and ACTITRANS2D (low order), two airfoils are generated by transforming a cylinder via the von Kármán–Trefftz map. The parameters of these cylinders can be found in table 2.1.

Table 2.1: von Kármán–Trefftz airfoil parameters

Variable	Airfoil I	Airfoil II
κ	0.0	0.25
ϵ	0.16	0.40
τ	8.0	25.0
l	0.25	0.25
n_x	151	261

As can be seen, airfoil I is symmetric (no camber), thinner than airfoil II, consists of a sharper trailing edge and has less panels along the surface. This choice is to show that it works for a variety of airfoils. Important to point out is that to perform a valid comparison between the panel methods and theory for each airfoil, the same panel distribution along the surface has to be set.

The panels are distributed by first creating a circle in the ζ-plane (see appendix D) using a uniform step in θ (equal parts). Now, the circle coordinates follow from:

$$\begin{aligned} \xi_i &= a \cdot \cos(\theta_i - \beta) + \xi_\mu \qquad \text{where } i = 1, 2, ..., n_x \\ \eta_i &= a \cdot \sin(\theta_i - \beta) + \eta_\mu \end{aligned}$$

Via the von Kármán–Trefftz transformation, the airfoil coordinates $Z = x + iy$ will follow. By adapting n_x, more or less panels can be chosen. Based on the calculation of the inviscid velocity at the airfoil's surface, the pressure coefficient can be determined. Using this variable, the lift coefficient can also be determined by integration along the surface. The pressure coefficient comparison can be seen in figure 2.3 for airfoil I and in figure 2.4 for airfoil II. Zooms are created in both figures to get a better look at the regions where the most severe changes in pressure coefficient occur.

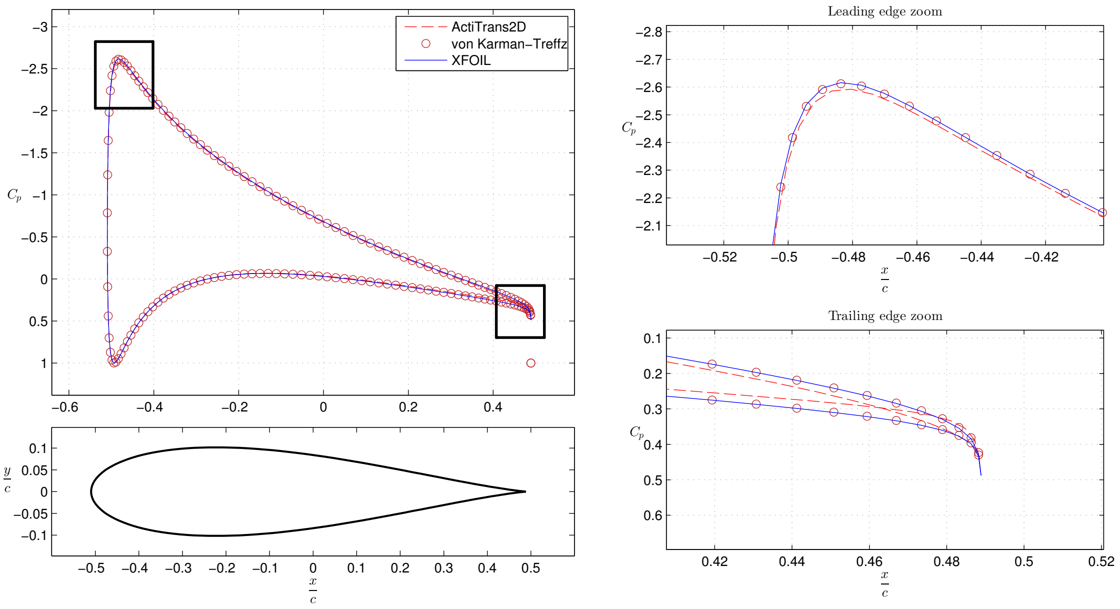

Figure 2.3: Pressure coefficient distribution airfoil I at $\alpha = 8^o$.

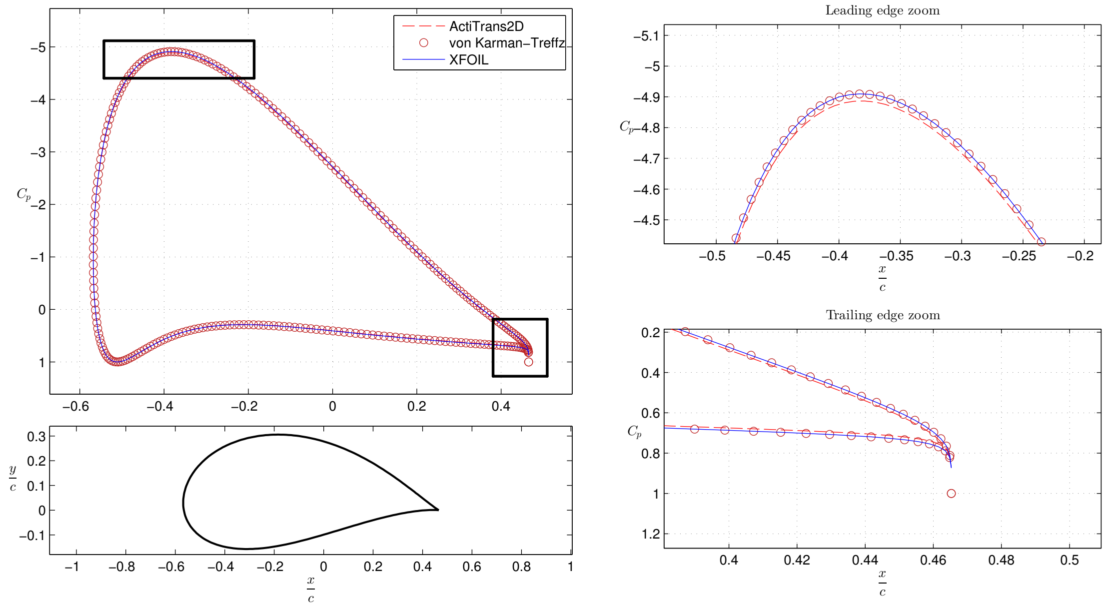

Figure 2.4: Pressure coefficient distribution airfoil II at $\alpha = 12^o$.

Observing both figures, it can be seen that airfoil I has a more sharp pressure peak at the leading edge. This is the result from a sharper leading edge shape as compared to airfoil II. The panel method from XFOIL is quite accurate at both airfoils as compared with exact theory. The panel method from ACTITRANS2D is less accurate, especially at the leading and trailing edge regions. Notice that for airfoil I, the pressure coefficient in the trailing edge region is different than the exact theory. For airfoil II, it seems better and resembles exact theory.

To resolve the issue at the sharp trailing edge at airfoil I, the number of panels was increased, repaneling was performed according to the half cosine distribution (as explained in appendix B) and the point where the Kutta condition is satisfied was varied. Although the kink in the pressure distribution at the trailing edge slightly changes, these measures will not resolve the problem.

Other reasons for this kink could be that for sharp trailing edges, panels on the upper and lower side get too close to each other and cause numerical problems (hence it would be beneficial to 'cut off' the trailing edge and use a finite trailing edge thickness). Most likely, the problem lies in the nature of the panel method that has been used. In XFOIL, linear vorticity strength on each panel is applied as opposed to ACTITRANS2D, where constant sources on each panel is applied with only a single vortex strength to satisfy the Kutta condition. The values for the corresponding lift coefficient are graphically represented in figure 2.5. Note that the differences are quite small and therefore table 2.2 is presented with the relative error with exact theory. The relative error is for almost all cases within 0.5%. With increased panel number for airfoil II, the relative error decreases to a significant smaller value for the 'high-order' method than for the 'low-order' method.

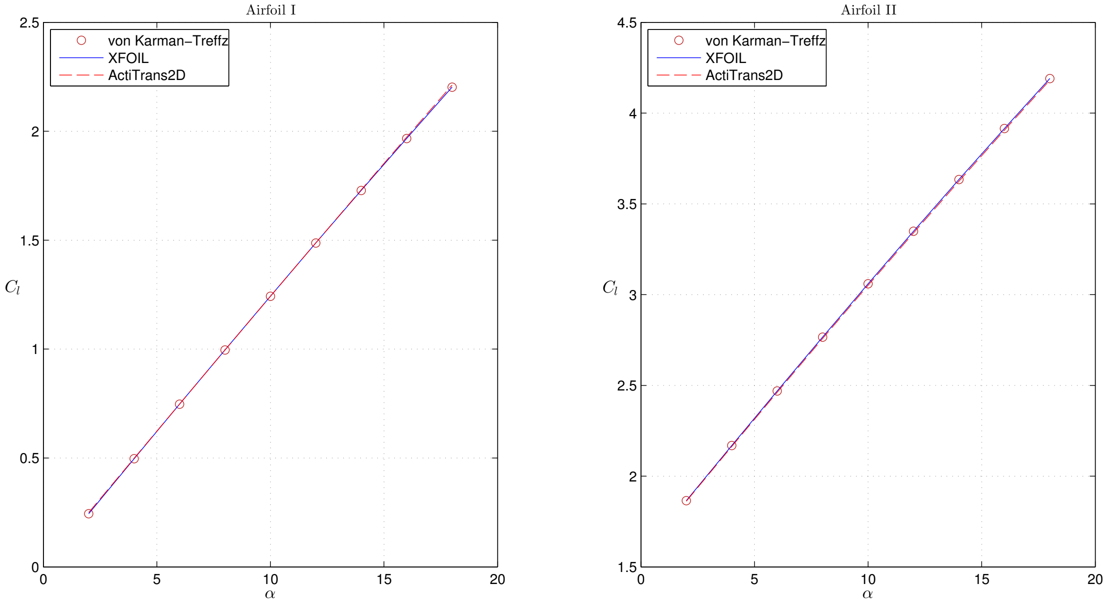

Figure 2.5: Inviscid lift polar both airfoils.

Now, a useful numerical test is to examine the solution convergence for increasing panel density for each method. This test has been performed for airfoil II at an angle of attack of 8^o. A visualization of the results can be found in figure 2.6.

Table 2.2: Indication of the relative error (E) in percent between the exact lift coefficient and the panel methods from XFOIL and ACTITRANS2D. Left table represents airfoil I and right table airfoil II.

	XFOIL	ACTITRANS2D
α	E(%)	E(%)
2	0.123	2.250
4	0.060	0.483
6	0.040	0.054
8	0.030	0.050
10	0.040	0.024
12	0.027	0.054
14	0.029	0.174
16	0.031	0.310
18	0.027	0.450

	XFOIL	ACTITRANS2D
α	E(%)	E(%)
2	0.005	0.182
4	0.005	0.240
6	0.000	0.267
8	0.004	0.278
10	0.003	0.278
12	0.003	0.269
14	0.006	0.250
16	0.005	0.230
18	0.005	0.205

The calculation of the lift coefficient with XFOIL has only be performed up till 200 panels since the maximum number of panels is restricted to 281. Notice that the convergence of the conformal mapping and the panel method from XFOIL ('high-order') is faster than the 'low-order' Hess–Smith panel method from ACTITRANS2D. To illustrate, the blue line becomes nearly horizontal at a lower number of panels than the red dashed line. It can be reasonably assumed that convergence is obtained when 200 panels or more are taken along the complete surface.

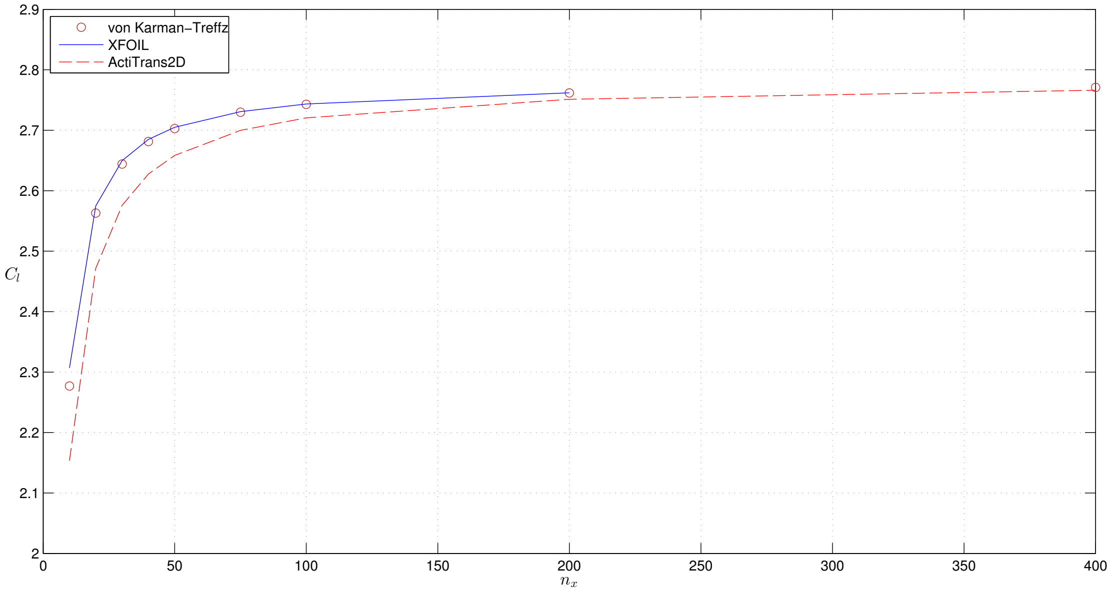

Figure 2.6: Lift coefficient convergence. Airfoil II at $\alpha = 8^o$, number of panels varied.

CHAPTER
THREE

Boundary layers with mass transfer

In this chapter, the way in which the boundary layer is treated is explained together with the changes that are necessary to include surface mass transfer. It covers historical thoughts as well as modern ways to solve for the boundary layer.

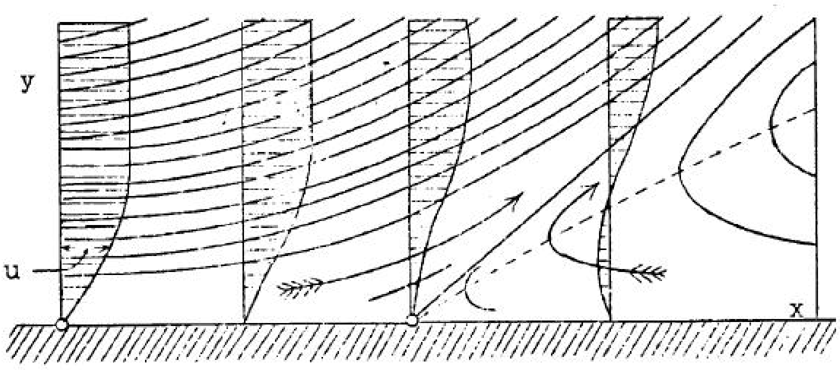

Figure 3.1: Boundary layer close to separation. Taken from a translation of the famous Prandtl 1904 paper – Prandtl [1904].

3.1 In the footsteps of Ludwig Prandtl

To find the origin of the term boundary layer, we should go back to the year 1904 where Ludwig Prandtl presented a paper on his ideas of the boundary layer concept. At first, he used both the terms transition layer and boundary layer. In his 1904 paper, he referred to boundary layer only once but it was this term that survived, mainly because of its use in papers by Prandtl's students (Anderson [2005]).

Prandtl was born 4 February 1875, in Freising, Bavaria (Germany) and grew up as an only child. Although primarily interested in solid mechanics throughout his life, this work was overshadowed by his great contributions to the study of fluid flows. In 1901, Prandtl became a professor of mechanics in the mechanical engineering department at the Technische Hochschule in Hannover where he developed his boundary layer theory. Soon after his famous presentation in 1904[5] he moved to the prestigious University of Göttingen to become director of the Institute for Technical Physics. As described by Théodore von Kármán (a student of Prandtl and another key person in the fluid dynamics community), Prandtl was 'an engineer by training', who had the ability to turn physical phenomena into simple mathematical form. Ludwig Prandtl died in 1953 but his work will live on as long as fluid dynamics is studied and applied.

It was his idea in which he claimed that due to the friction, the fluid immediately adjacent to the surface should stick to the surface (the no-slip condition) and that the effects of friction are only felt in a thin region near the surface (the boundary layer). Although his famous paper was very short, he derived the boundary layer equations (see section 3.3) by reducing the Navier-Stokes equations. The major mathematical breakthrough is that the boundary layer equations have a completely different mathematical behaviour (parabolic) than the Navier-Stokes equations (elliptic). In elliptic problems, the complete flowfield must be solved simultaneously together with the boundary conditions implied on the complete boundary of the flow. Parabolic problems on the other hand can be solved by marching downstream step by step subject to specified inflow conditions and boundary condition at the edge of the boundary layer.

In spite of the important work of Prandtl and others (for example Heinrich Blasius) the fluid dynamics community paid only little attention. It was when von Kármán derived his momentum integral equation – by integrating the boundary layer equations along the boundary layer (see subsection 3.4.2) that provides the direct applicability to a large number of practical problems – when they began to receive more attention.

By now, physicists and engineers have written hundreds of books about boundary layer theory of which the best know is Schlichting and Gersten [2000]. Hermann Schlichting was also a student of Prandtl and this book contains technical material of which the roots go back to Prandtl's famous presentation.

---

[5] Third International Mathematics Congress – Heidelberg (Germany) – August 1904. His presentation was only ten minutes long, but it was all that was needed to describe his revolutional ideas that changed the world of fluid dynamics.

3.2 Defining the boundary layer

Continuing with the ideas of Prandtl, this section will cover the most important parameters to describe the boundary layer. It will cover the concept of displacement and momentum thickness, the shape factor and the skin friction coefficient, respectively. A graphical interpretation of the inviscid case as compared to the viscid case can be seen in figure 3.2. This figure shows that the displacement thickness is the distance by which an external streamline is displaced by the presence of the boundary layer (derived in equation 3.55).

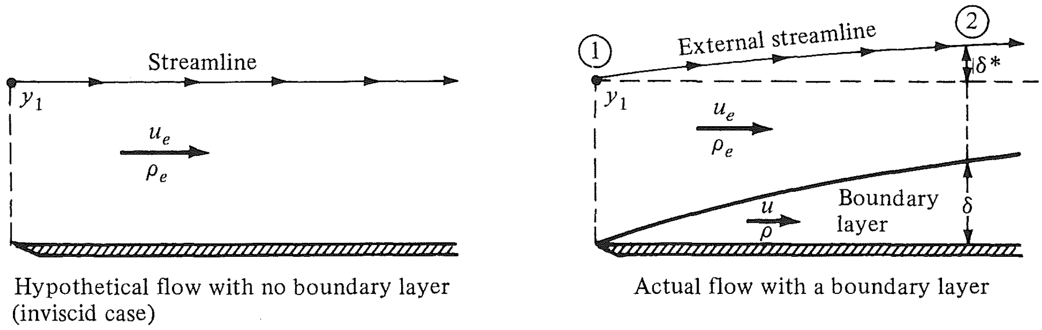

Figure 3.2: Interpretation inviscid and viscid case.

Displacement thickness

This quantity is a measure for the missing mass flow due to the presence of the boundary layer. Its expression can be derived by comparing the inviscid and viscous situation as represented in figure 3.2. For the inviscid case, the mass flow can be written as:

$$\int_0^\infty (\rho_e u_e)\,\mathrm{dy} \tag{3.1}$$

For the viscid case:

$$\int_0^\infty (\rho u)\,\mathrm{dy} \tag{3.2}$$

Expressing the missing mass flow as the product of $\rho_e u_e$ and height δ^*, one finds:

$$\begin{aligned} \rho_e u_e \delta^* &= \int_0^\infty (\rho_e u_e - \rho u)\,\mathrm{dy} \\ \delta^* &= \int_0^\infty \left(1 - \frac{\rho u}{\rho_e u_e}\right)\mathrm{dy} \end{aligned} \tag{3.3}$$

Momentum thickness

Analogue to the interpretation of the displacement thickness, the momentum thickness represents the missing momentum flow due to presence of the boundary layer. Momentum is defined by multiplying the mass flow with the velocity. The mass flow is defined as the mass flow in the viscous case. Therefore, the momentum flow in the inviscid case can be written as:

$$u_e \int_0^\infty (\rho u)\,\mathrm{dy} \tag{3.4}$$

And for the viscid case:

$$\int_0^\infty \left(\rho u^2\right) \mathrm{dy} \tag{3.5}$$

Expressing the missing momentum flow as the product of $\rho_e u_e^2$ and height θ, one finds:

$$\begin{aligned} \rho_e u_e^2 \theta &= \int_0^\infty \rho u \left(u_e - u\right) \mathrm{dy} \\ \theta &= \int_0^\infty \frac{\rho u}{\rho_e u_e} \left(1 - \frac{u}{u_e}\right) \mathrm{dy} \end{aligned} \tag{3.6}$$

The momentum thickness is often used to determine the profile drag of a certain geometry. For a calculated velocity profile, the displacement thickness is always the greater of the two. This can be seen in figure 3.3.

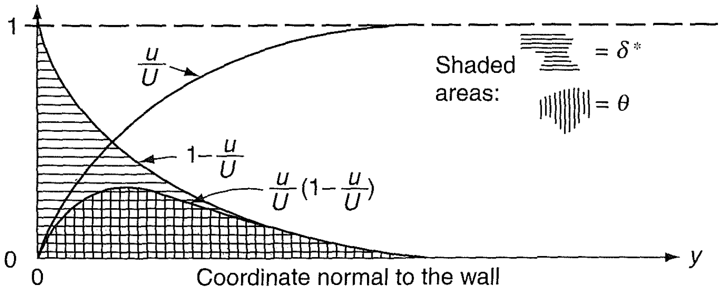

Figure 3.3: Displacement and momentum thickness (from White [2006]).

Shape factor

A frequently used parameter in boundary layer analysis is the shape factor. It is defined as the quotient of the displacement and momentum thickness:

$$H = \frac{\delta^*}{\theta} \tag{3.7}$$

It gives an indication of the state of the boundary layer as can be seen in figure 3.4. Some typical values for a laminar boundary layer can be seen in table 3.1. Note that the shape factor can never reach a value below one.

Table 3.1: Laminar boundary layer.

State	Shape factor
Near stagnation point	2.2
Near minimum pressure	2.6
Close to separation	4
Separated	$O(10)$

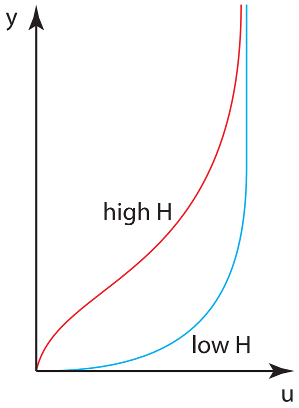

Figure 3.4: Boundary layer condition.

Skin friction coefficient

The slope of the velocity profile of the boundary layer near the wall is of particular importance since it gives a measure of the wall shear stress. The wall shear stress is given by:

$$\tau_w = \mu \left(\frac{\partial u}{\partial y} \right)_{y=0} \tag{3.8}$$

where μ is the absolute viscosity coefficient of the gas. It is different for different gases at different temperatures but for air at standard sea-level temperature:

$$\mu = 1.7894 \text{ x } 10^{-5} \ \ [\text{kg/ms}] \tag{3.9}$$

From observation of the velocity profiles of laminar and turbulent boundary layers, it can be stated that (Anderson [2007]):

$$\left(\frac{\partial u}{\partial y} \right)_{y=0} \text{ laminar flow } < \left(\frac{\partial u}{\partial y} \right)_{y=0} \text{ turbulent flow} \tag{3.10}$$

and thus is the laminar shear stress less than the turbulent shear stress:

$$(\tau_w)_{\text{laminar}} < (\tau_w)_{\text{turbulent}} \tag{3.11}$$

Now, the skin friction coefficient (dimensionless) is defined as:

$$C_f = \frac{\tau_w}{\frac{1}{2}\rho_e u_e^2} \tag{3.12}$$

3.3 Boundary layer equations

In order to study the behaviour of boundary layers, one must return to the most general form of the equations of motion of a Newtonian fluid (linear stress-strain relationship). These equations of motion can be derived by specifying the conservation of mass, momentum and energy within a small volume element. This element will be considered as a continuum in which the smallest volume element considered is still continuous. This is the case when the dimensions are still significantly larger than the distance between the molecules in the fluid. The complete derivation of the equations of motion will be left out, but can be found in Anderson [2007]. The resulting expressions for a two-dimensional steady incompressible Newtonian fluid with negligible body forces are given by:

$$\begin{aligned}
&\text{continuity equation}\\
&\nabla \cdot \mathbf{V} = \frac{\partial u}{\partial x} + \frac{\partial v}{\partial y} = 0\\
&\text{x-momentum equation}\\
&u\frac{\partial u}{\partial x} + v\frac{\partial u}{\partial y} = -\frac{1}{\rho}\frac{\partial p}{\partial x} + \nu\left(\frac{\partial^2 u}{\partial x^2} + \frac{\partial^2 u}{\partial y^2}\right)\\
&\text{y-momentum equation}\\
&u\frac{\partial v}{\partial x} + v\frac{\partial v}{\partial y} = -\frac{1}{\rho}\frac{\partial p}{\partial y} + \nu\left(\frac{\partial^2 v}{\partial x^2} + \frac{\partial^2 v}{\partial y^2}\right)
\end{aligned} \tag{3.13}$$

In order to get the conservation equations for turbulent flows, the instantaneous quantities in equation 3.13 are replaced by the sum of their mean and fluctuating parts. This is the principle of Reynolds averaging and can be described for this case by the expressions and properties stated in 3.14 together with the properties of the averaging operator (often called Reynolds conditions). Note that the mean parts have a bar and the fluctuating parts an apostrophe. The derivation is left out for convenience but has been verified and can be found in Pope [2000]. The resulting set of equations after Reynolds averaging is given by equation 3.15.

$$\begin{aligned}
u &= \overline{u} + u'\\
v &= \overline{v} + v'\\
p &= \overline{p} + p'
\end{aligned} \tag{3.14}$$

Where for the mean quantities the ensemble average is used (satisfying all Reynolds conditions):

$$\overline{u} = \lim_{N\to\infty} \frac{1}{N}\sum_{i=1}^{N} u_i$$

$$\begin{aligned}
&\frac{\partial \overline{u}}{\partial x} + \frac{\partial \overline{v}}{\partial y} = 0\\
&\overline{u}\frac{\partial \overline{u}}{\partial x} + \overline{v}\frac{\partial \overline{u}}{\partial y} = -\frac{1}{\rho}\frac{\partial \overline{p}}{\partial x} + \nu\left(\frac{\partial^2 \overline{u}}{\partial x^2} + \frac{\partial^2 \overline{u}}{\partial y^2}\right) - \frac{\partial}{\partial x}\left(\overline{u'^2}\right) - \frac{\partial}{\partial y}\left(\overline{u'v'}\right)\\
&\overline{u}\frac{\partial \overline{v}}{\partial x} + \overline{v}\frac{\partial \overline{v}}{\partial y} = -\frac{1}{\rho}\frac{\partial \overline{p}}{\partial y} + \nu\left(\frac{\partial^2 \overline{v}}{\partial x^2} + \frac{\partial^2 \overline{v}}{\partial y^2}\right) - \frac{\partial}{\partial x}\left(\overline{u'v'}\right) - \frac{\partial}{\partial y}\left(\overline{v'^2}\right)
\end{aligned} \tag{3.15}$$

So far, two-dimensional steady and incompressible flow was emphasized and no simplifications were made to restrict the flow to boundary layers. These simplifications can be made by assuming that the ratio between boundary layer thickness δ and some reference length L is sufficiently small and perform an order of magnitude analysis.
Noting that the orders can be described by:

$$\overline{u} \sim u_e \qquad \overline{p} \sim \rho u_e^2 \qquad \overline{x} \sim L \qquad \overline{y} \sim \delta$$

From the continuity equation in 3.15, it can easily be seen that the order of $\overline{v}$ must be:

$$\overline{v} \sim \frac{u_e \delta}{L}$$

Furthermore, assume large Reynolds numbers:

$$\frac{\delta}{L} \sim \frac{1}{\sqrt{Re_L}} \qquad Re_L = \frac{u_e L}{\nu}$$

For the fluctuation terms $\overline{u'^2}$, $\overline{v'^2}$ and $\overline{u'v'}$ in the x-momentum and y-momentum equations from 3.15 it is assumed that they are all of the same order of magnitude:

$$\overline{u'^2} \sim \overline{v'^2} \sim \overline{u'v'}$$

For a complete order of magnitude analysis, see Cebeci and Cousteix [2005]. The result can be summarized as (omitting the bars for mean quantities):

$$\begin{aligned} \frac{\partial u}{\partial x} + \frac{\partial v}{\partial y} &= 0 \\ u\frac{\partial u}{\partial x} + v\frac{\partial u}{\partial y} &= -\frac{1}{\rho}\frac{\partial p}{\partial x} + \nu\frac{\partial^2 u}{\partial y^2} - \frac{\partial}{\partial y}\left(\overline{u'v'}\right) \\ \frac{\partial p}{\partial y} &= 0 \end{aligned} \tag{3.16}$$

Comparing the x- and y-momentum parts of 3.13 and 3.16 with each other, we see that the boundary layer approximations reduced some viscous terms and neglected the pressure variation in y-direction. At the cost of these reductions, an extra fluctuation term has popped up that is called the turbulent shear stress. Detailed knowledge of the physical processes of turbulent fluctuations is required in order to develop as good and generally valid model equations as possible.
As a result of zero pressure variation in y-direction, the pressure is not longer an unknown and can be equated to the free-stream value where Bernoulli's law applies:

$$\frac{\partial p}{\partial x} = -\rho u_e \frac{\partial u_e}{\partial x}$$

The solutions to the boundary layer equations can either be obtained from the partial differential equations in 3.16 directly with assumptions on the Reynolds stress $-\rho\overline{u'v'}$ (via finite difference techniques) or via integral techniques that reduce the partial differential equations to ordinary differential equations together with several empirical closure models.
This distinction is the nerve of the difference between the design tools RFOILSUCV2 and ACTITRANS2D. In general, finite difference methods offer more flexibility and for the purpose of mass transfer this becomes very important.

3.4 Solution strategies

As proposed in section 3.3, finite difference and integral methods are the two main methods to solve for the boundary layer equations. Of the two, the first one offers the most flexibility and is used in ACTITRANS2D. The latter one, used in XFOIL and RFOILSUCV2, requires more empirical relations but needs less computation time.
How do these methods work and how can they be extended for boundary layer mass transfer? Read on, stay tuned and find out in subsections 3.4.1 and 3.4.2.

3.4.1 Finite difference method

Finite difference methods are based on the solution of the boundary layer equations in their partial differential form. The system can be found in equation 3.16. By using the no slip condition and the possibility of mass transfer at the wall, the boundary conditions can be written as expression 3.17.

$$\begin{array}{lll} y = 0 & u = 0 & v = v_w(x) \\ y = \delta & u = u_e & \end{array} \tag{3.17}$$

As the boundary layer thickness increases with increasing downstream position, it is necessary to take small steps to maintain computational accuracy. By using transformed coordinates, this growth can be reduced and larger steps can be taken in streamwise direction. Here, the Falkner-Skan transformation will be used in which the dimensionless similarity variable η and a dimensionless stream function $f(x,\eta)$ are defined by:

$$\begin{aligned} \eta &= \sqrt{\frac{u_e}{\nu x}}\, y \\ \psi(x,\eta) &= \sqrt{u_e \nu x}\, f(x,\eta) \end{aligned} \tag{3.18}$$

By using these transformations, the system can be written as (for a derivation see Cebeci and Bradshaw [1977] and note that an apostrophe now means a derivative with respect to η):

$$(bf'')' + \frac{m+1}{2} f f'' + m\left[1 - (f')^2\right] = x\left(f' \frac{\partial f'}{\partial x} - f'' \frac{\partial f}{\partial x}\right) \tag{3.19}$$

with boundary conditions:

$$\begin{array}{lll} \eta = 0 & f' = 0 & f = f_w \\ \eta = \eta_e & f' = 1 & \end{array} \tag{3.20}$$

In equation 3.20, f_w represents the dimensionless stream function at the wall that takes into account the possibility for mass transfer at the surface. Its expression can be derived starting from the definition of the streamfunction:

$$\begin{aligned} v &= -\frac{\partial \psi}{\partial x} \\ \psi(x,0) &= -\int_0^x v_w(x)\,\mathrm{d}x \end{aligned} \tag{3.21}$$

Using these relations and the transformations from equation 3.18, one can write it as:

$$f_w = f(x,0) = \frac{\psi(x,0)}{\sqrt{u_e \nu x}} = -\frac{1}{\sqrt{u_e \nu x}} \int_0^x v_w(x)\,\mathrm{d}x \tag{3.22}$$

In equation 3.19, b is a parameter that is used to describe the turbulent shear stress and m is the pressure gradient parameter:

$$b = 1 + \frac{\nu_t}{\nu} \qquad\qquad m = \frac{x}{u_e}\frac{\mathrm{d}u_e}{\mathrm{d}x}$$

The turbulent shear stress can be modeled in many different ways. An overview can be found in van den Berg [2011]. Here, a mixing length model is used by letting:

$$-\overline{u'v'} = \nu_t \frac{\partial u}{\partial y} = l^2 \left(\frac{\partial u}{\partial y}\right)^2$$

where l is the mixing length. The reader is referred to section 3.6 for a more elaborate discussion on this topic.

For the inverse calculations, transformation 3.23 will be used (since u_e is also treated as unknown, see subsection 3.4.3). This will lead to slightly different relations as can be found in Cebeci and Cousteix [2005].

$$\begin{aligned} \eta &= \sqrt{\frac{u_\infty}{\nu x}}\,y \\ \psi(x,\eta) &= \sqrt{u_\infty \nu x}\, f(x,\eta) \end{aligned} \tag{3.23}$$

Several numerical methods to solve equation 3.19 can be used. In the book series of Cebeci, the use of Keller's box method is encouraged. It involves only slightly more arithmetic than the Crank–Nicolson method and it is second order accurate with possibly non uniform spacings. Here, only the key features of this method will be presented. For a detailed discussion, see Cebeci [1999].

The steps that should be taken can be summarized as follows:

- **Reduce order:** Write equation 3.19 as a system of three first order equations. Use $f' = u$ and $u' = v$.
- **Finite differencing:** Approximate the equations on an arbitrary rectangular mesh. The ordinary differential equation is discretized by using centered differences and the partial differential equation is approximated at the mid point of the rectangle. The result is an implicit and non linear system.
- **Linearization:** Use Newton's method.
- **Matrix system:** Write as a non singular matrix system of form $\mathbf{A}\mathbf{x} = \mathbf{b}$ where $\mathbf{x}$ contains the unknowns.
- **Solve:** Use built in MATLAB functions[6]. Iterate until converged solutions exist.

For the purpose of this thesis, it is more useful to describe the modifications that are made to simulate boundary layer mass transfer than to describe all the details of the solution strategy that can mostly be found elsewhere. These modifications will now be covered.

---

[6] Including LU decomposition as mentioned in Ferziger and Perić [2002].

Wall boundary condition

First of all, and probably most important, the boundary condition at the wall is corrected to simulate mass transfer through the wall. This term already popped up in previous equations and can be seen in expression 3.22. In ACTITRANS2D, normalized parameters are used as well as a Reynolds number based on a reference length c :

$$\mathrm{Re}_c = \frac{u_\infty c}{\nu} \qquad \xi = \frac{x}{c} \qquad w = \frac{u_e}{u_\infty} \qquad \mathrm{d}x = \frac{\mathrm{d}x}{\mathrm{d}\xi} = c \cdot \mathrm{d}\xi$$

Using these relations, the expression for f_w can be rewritten as:

$$\begin{aligned} f_w &= -\frac{1}{\sqrt{\left(\frac{u_e}{u_\infty}\right) u_\infty \nu \xi \cdot c}} \int_0^\xi c \cdot v_w\left(\xi\right) \mathrm{d}\xi \\ &= -\frac{\sqrt{\frac{u_\infty c}{\nu}}}{\sqrt{w\xi}} \int_0^\xi c \cdot \left(\frac{v_w\left(\xi\right)}{u_\infty}\right) \mathrm{d}\xi \\ f_w &= -\frac{\sqrt{\mathrm{Re}_c}}{\sqrt{w\xi}} \int_0^\xi c \cdot \left(\frac{v_w\left(\xi\right)}{u_\infty}\right) \mathrm{d}\xi \end{aligned} \tag{3.24}$$

For the inverse calculations, $u_e = u_\infty$ and thus $w = 1$. Then the dimensionless stream function at the wall becomes:

$$f_w = -\frac{\sqrt{\mathrm{Re}_c}}{\sqrt{\xi}} \int_{\xi_0}^\xi c \cdot \left(\frac{v_w\left(\xi\right)}{u_\infty}\right) \mathrm{d}\xi \tag{3.25}$$

Initial profiles

To solve the system in linearized form, initial estimates of f_j, u_j and v_j must be used. It is useful to provide a good estimate for this. By assuming a third order polynomial:

$$u = a + b\eta + c\eta^3$$

and using the boundary conditions from equation 3.20 (and the fact that at the boundary layer edge: $\frac{\partial u}{\partial \eta} = f'' = 0$), the initial profiles (with mass transfer at the wall) can be derived to be:

$$\begin{aligned} f_j &= f_w + \frac{1}{4}\eta_e \left(\frac{\eta_j}{\eta_e}\right)^2 \left[3 - \frac{1}{2}\left(\frac{\eta_j}{\eta_e}\right)^2\right] \\ u_j &= \frac{3}{2}\left(\frac{\eta_j}{\eta_e}\right) - \frac{1}{2}\left(\frac{\eta_j}{\eta_e}\right)^3 \\ v_j &= \frac{3}{2}\frac{1}{\eta_e}\left[1 - \left(\frac{\eta_j}{\eta_e}\right)^2\right] \end{aligned} \tag{3.26}$$

Displacement thickness

Starting from the incompressible version of 3.3, one can write the displacement thickness in the coordinates that are used in ACTITRANS2D corrected for mass transfer. Write the displacement thickness as 3.27.

$$\delta^* = \int_0^\infty \left(1 - \frac{u}{u_e}\right) \mathsf{dy} \approx \int_0^\delta \left(1 - \frac{u}{u_e}\right) \mathsf{dy} \tag{3.27}$$

Transform this relation to the new coordinates by using:

$$\mathsf{dy} = \left(\frac{\mathsf{dy}}{\mathsf{d}\eta}\right) \mathsf{d}\eta = \sqrt{\frac{\nu x}{u_e}} \mathsf{d}\eta = \frac{x}{\sqrt{\mathsf{Re}_x}} \mathsf{d}\eta$$

Then, equation 3.27 becomes:

$$\begin{aligned} \delta^* &= \frac{x}{\sqrt{\mathsf{Re}_x}} \int_0^{\eta_e} (1 - f') \, \mathsf{d}\eta = \frac{x}{\sqrt{\mathsf{Re}_x}} [\eta - f]_0^{\eta_e} \\ &= \frac{x}{\sqrt{\mathsf{Re}_x}} [\eta_e - f_e + f_w] \end{aligned} \tag{3.28}$$

For the inverse calculations, transformation 3.23 is used. Then:

$$\mathsf{dy} = \sqrt{\frac{\nu x}{u_\infty}} \mathsf{d}\eta = \frac{\sqrt{x}}{\sqrt{\mathsf{Re}_c}} \mathsf{d}\eta$$

As a consequence of the new transformation, $f' = u/u_\infty$ and thus:

$$\frac{u}{u_e} = \frac{u}{u_\infty} \frac{u_\infty}{u_e} = \frac{f'}{w}$$

For the inverse calculation, equation 3.27 becomes:

$$\begin{aligned} \delta^* &= \frac{\sqrt{x}}{\sqrt{\mathsf{Re}_c}} \int_0^{\eta_e} \left(1 - \left(\frac{f'}{w}\right)\right) \mathsf{d}\eta = \frac{\sqrt{x}}{\sqrt{\mathsf{Re}_c}} \left[\eta - \left(\frac{f}{w}\right)\right]_0^{\eta_e} \\ &= \frac{\sqrt{x}}{\sqrt{\mathsf{Re}_c}} \left[\eta_e - \frac{(f_e - f_w)}{w}\right] \end{aligned} \tag{3.29}$$

Eddy viscosity model

For the corrections to this model, the reader is referred to section 3.6. In short, a two layer method is used that considers different eddy viscosities for the inner and outer layer. The functions are empirical and based on a limited range of experimental data. The formulation for the inner layer is corrected for mass transfer by Cebeci [1999], Kays and Moffat [1975] and Kays et al. [1969]. The outer layer viscosity includes a term for the displacement thickness which is modified according to 3.28 or 3.29.

Transition model

Since there is no fundamental theory to describe the transition from laminar to turbulent flow, engineering prediction methods are used. In the past, many of these methods were used and an overview can be seen in White [2006]. It is usually a function of the following parameters:

- Pressure gradient

- Surface roughness
- Mach number
- Free stream turbulence
- Wall suction or blowing
- Wall heating or cooling

Most prediction methods only deal with one or two of these parameters. In ACTITRANS2D, it is tried to use a prediction method that can handle wall suction and blowing. In White [2006], the one-step method of Wazzan et al. is mentioned for this purpose. For details and more options to determine transition, the reader is referred to section 3.5.

Sink drag

The output drag coefficient should be modified to include the so called sink drag. This extra drag term, that is present due to removal of the fluid, is discussed in detail in section 3.7.

Potential flow

To include the viscous effects in the potential method to compute the corrected pressure distribution, various approaches can be used. The one chosen here is to add a normal velocity component at the right hand side of the potential flow equations defined by the expression:

$$v_n = \frac{\mathrm{d}}{\mathrm{d}x}\left(u_e \delta^*\right)$$

In this way, no adjustments to the surface should be made. For more information on how to include the viscous effects in the panel method, see subsection 3.4.4.
Now, according to Bellobuono [2006], to include the effect of mass transfer along the surface, a correction should be made to the normal velocity v_n:

$$v_n = \frac{\mathrm{d}}{\mathrm{d}x}\left(u_e \delta^*\right) + v_w\left(x\right)$$

3.4.2 Integral techniques

Most integral methods are based on the momentum integral equation (first derived by Théodore von Kármán). This equation, including surface mass transfer terms, is derived in appendix E by starting from equation 3.16 where the pressure term is eliminated via Bernoulli and the total shear stress is defined as $\tau = \mu\left(\partial u/\partial y\right) - \rho\overline{u'v'}$. The result can be seen in equation E.5. In RFOILSUCV2, a slightly different version is used that takes a compressibility correction into account (from Drela [1985]):

$$\frac{\mathrm{d}\theta}{\mathrm{d}x} + \left(H + 2 - M_e^2\right)\frac{\theta}{u_e}\frac{\mathrm{d}u_e}{\mathrm{d}x} = \frac{C_f}{2} + \frac{v_w}{u_e} \tag{3.30}$$

Furthermore, the energy shape parameter integral equation is written as (Ferreira [2002]):

$$\theta\frac{\mathrm{d}H^*}{\mathrm{d}x} + \left(2H^{**} + H^*\left(1 - H\right)\right)\frac{\theta}{u_e}\frac{\mathrm{d}u_e}{\mathrm{d}x} = 2C_D - H^*\frac{C_f}{2} + \left(1 - H^*\right)\frac{v_w}{u_e} \tag{3.31}$$

These relations are valid for both laminar and turbulent boundary layers including mass transfer. These two equations contain six unknowns ($\delta^*, \theta, C_f, C_D, H^*$ and H^{**}) for which two can be solved for (usually δ^* and θ). In these equations C_D represents the dissipation coefficient defined as:

$$C_D = \frac{1}{\rho_e u_e^3} \int_0^\infty \tau \left(\frac{\partial u}{\partial y} \right) \mathrm{d}y$$

Also two new shape parameters H^* and H^{**} are defined as:

$$H^* = \frac{\theta^*}{\theta} \qquad H^{**} = \frac{\delta^{**}}{\theta}$$

$$\theta^* = \int_0^\infty \frac{\rho u}{\rho_e u_e} \left(1 - \left(\frac{u}{u_e} \right)^2 \right) \mathrm{d}y \qquad \delta^{**} = \int_0^\infty \frac{u}{u_e} \left(1 - \frac{\rho}{\rho_e} \right) \mathrm{d}y$$

Thus, to solve equations 3.30 and 3.31, four additional 'closure' relations should be used. For these closure relations, numerous variations exist in literature and for full detail of the original closure relations (without mass transfer effects), one is referred to Drela [1985] and Ferreira [2002].

Important to point out is that it took until the thesis of Merchant [1996] (and de Oliveira [2011]) until someone investigated the effect of adapting the closure relations for mass transfer. In Ferreira [2002], only the modifications as shown in equations 3.30 and 3.31 were taken into account leading to the program XFOILSUC. With the changes of de Oliveira [2011], RFOILSUCV2 was born.

In this subsection, a concise description is given of the possible corrections that could be made to the original closure relations to account for the effect of surface mass transfer.

Skin friction coefficient

It can be imagined that the skin friction coefficient closure relation should be adapted for mass transfer since it will affect the velocity gradient near the wall. In this paragraph, two attempts will be noted. One described in Kays et al. [2005] and one in Merchant [1996].

To follow the reasoning in Kays et al. [2005] (page 212-215), the skin friction closure relation may be modified according to equation 3.32, where C_{f_0} is the original closure relation without mass transfer.

$$C_{f_s} = C_{f_0} \cdot \frac{\ln\left(1 + B_f\right)}{B_f} \qquad \text{where} \qquad B_f = \frac{\left(\frac{v_w}{u_e}\right)}{\left(\frac{C_{f_s}}{2}\right)} \tag{3.32}$$

This (implicit) relation is only valid for small pressure gradients and small mass transfer values. In the second approach, first the effect of mass transfer on the shear stress τ is shown by writing equation E.1 close to the wall:

$$\begin{aligned} \rho v_w \frac{\partial u}{\partial y} &= \rho u_e \frac{\mathrm{d}u_e}{\mathrm{d}x} + \frac{\partial \tau}{\partial y} \\ \tau &\approx \tau_w - \rho u_e \frac{\mathrm{d}u_e}{\mathrm{d}x} y + \rho v_w u \end{aligned} \tag{3.33}$$

Merchant [1996] then used the concept of slip velocity[7] and stated that the wall shear stress with transpiration can be written as:

$$\tau_{w_s} \approx \tau_{w_0} - \rho v_w u_s \tag{3.34}$$

and thus the skin friction coefficient becomes:

$$C_{f_s} \approx C_{f_0} - 2\rho \frac{v_w}{u_e} \frac{u_s}{u_e} \tag{3.35}$$

Dissipation coefficient

Again observing Merchant [1996], the dissipation coefficient with transpiration can be splitted into two parts – a part where the inner layer is affected by transpiration and an outer layer that remains unchanged:

$$C_D = \frac{\tau_{w_s} u_s}{\rho_e u_e^3} + \frac{1}{\rho_e u_e^3} \int_0^\infty \tau \frac{\partial u}{\partial y} \mathrm{d}y \tag{3.36}$$

Substitution of relation 3.34 in equation 3.36 gives a new result for the dissipation coefficient:

$$C_{D_s} = \frac{C_{f_s}}{2} \frac{u_s}{u_e} - \frac{1}{2} \left(\frac{v_w}{u_e} \right) \left(\frac{u_s}{u_e} \right)^2 + C_\tau \left(1 - \frac{u_s}{u_e} \right) \tag{3.37}$$

where C_τ is the maximum shear stress coefficient (Drela [1985]). Note that without mass transfer, it falls back to the original closure relation for the dissipation coefficient.

Entrainment relation

Another closure relation extendable for transpiration can be based on entrainment. According to Head [1960] the boundary layer thickness δ grows because the boundary layer entrains irrotational fluid from the outer flow. This entrainment relation can be found in Schlichting and Gersten [2000] and is given by equation 3.38.

$$E = \frac{1}{u_e} \frac{\mathrm{d}}{\mathrm{d}x} \left[u_e \left(\delta - \delta^* \right) \right] \tag{3.38}$$

To use this relation, E should be related to the integral parameters (and hence the shape factor). Defining a new shape factor $H_1 = \left(\delta - \delta^* \right) / \theta$, one can write 3.38 as:

$$\frac{1}{u_e} \frac{\mathrm{d}}{\mathrm{d}x} \left(u_e \theta H_1 \right) = F \left(H_1 \right) \tag{3.39}$$

In which $F\left(H_1\right)$ is an empirical function relating the boundary layer mass to the shape factor. For both this function and the empirical relation between H_1 and H, several options can be used which can be found in White [2006].

According to Head [1960] once again, the influence of transpiration can be added by (only) changing 3.39 to the form:

$$\frac{1}{u_e} \frac{\mathrm{d}}{\mathrm{d}x} \left(u_e \theta H_1 \right) = F \left(H_1 \right) + \frac{v_w}{u_e} \tag{3.40}$$

---

[7] Velocity of the inner profile approaches u_s when $\eta \to \infty$ and velocity of the outer wake profile approaches u_s when $\eta \to 0$.

3.4.3 Standard and inverse methods

To be able to simulate airfoil flows for a wide application range, it should be possible to reasonably predict the angle of attack where massive flow separation (or stall) occurs. Stall behaviour is particularly important to predict the maximum lift coefficient $c_{l_{max}}$. Generally, stall can be categorized in leading and trailing edge stall. The former will usually occur for thin airfoils due to the strong adverse pressure gradient near the leading edge at high incidence, the latter is typical for thick airfoils where separation starts at the trailing edge and travels forward at increased incidence. At stall, small changes in angle of attack cause very large changes in δ^*, and it follows that convergence cannot be achieved. Another observation is that at this point, the thin boundary layer approximation will be violated. This aspect is one of the main limitations of ACTITRANS2D although the angle of attack where stall occurs can be reasonably approximated. Another aspect dealing with separating flow are separation bubbles. At low chord Reynolds number $\left(10^3 - 10^5\right)$, large separation bubbles can occur downstream of the leading edge. This bubble usually exist when laminar separation is followed by transition to turbulent flow that can resist larger adverse pressure gradients after which the flow reattaches to the airfoil surface. The length of the bubble increases with decreasing Reynolds number and can have significant influence on airfoil characteristics.

At higher Reynolds number $\left(10^6 - 10^7\right)$, transition often occurs before separation and transition is confined to a relatively small region. In these cases, empirical transition methods will work fine. In cases with larger bubbles, it is acceptable to set the onset of transition to the point where laminar separation occurs.

An interesting issue that comes along with backflow regions can be explained by means of a numerical experiment. Figure 3.5 represents a bubble with next to it the result for a computation of the boundary layer with prescribed δ^*. Station i, close to separation, is varied.

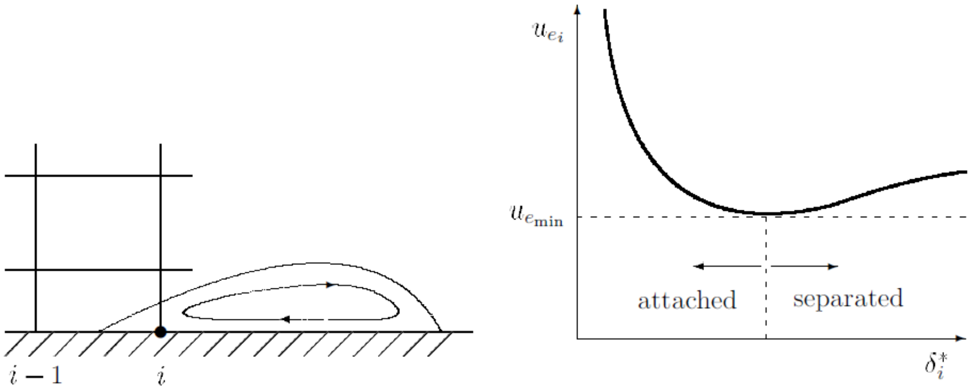

Figure 3.5: Bubble (left) and computation (right) from Veldman [2010].

As can be seen in figure 3.5, prescribing the boundary layer edge velocity (from inviscid calculations, called the 'standard' method) will not always yield a solution for δ^* (and sometimes two). This explains the numerical problems at separation points – often referred to as the 'Goldstein singularity'. Several ways to overcome this problem may be used.

To present this, denote the relations between the exteral flow and boundary layer in a symbolic way:

$$\begin{aligned} \text{External flow:} \qquad & u_e = E\left[\delta^*\right] \\ \text{Boundary layer:} \qquad & u_e = B\left[\delta^*\right] \end{aligned}$$

The 'standard' or 'direct' method mentioned earlier can be represented as the following iteration:

$$\begin{aligned} u_e^{(n)} &= E\left[\delta^{*(n-1)}\right] \\ \delta^{*(n)} &= B^{-1}\left[u_e^{(n)}\right] \end{aligned}$$

But as announced, the B^{-1} does not always exist, especially near separation. To overcome this problem, the iteration process can be reversed and the 'inverse' method is used:

$$\begin{aligned} \delta^{*(n)} &= E^{-1}\left[u_e^{(n-1)}\right] \\ u_e^{(n)} &= B\left[\delta^{*(n)}\right] \end{aligned}$$

The relation E^{-1} will usually exist but the scheme converges slowly. Mixtures of the methods is also possible and 'semi-inverse' methods will pop up. A problem that is associated when using some inverse method is the lack of a priori knowledge of the required δ^*. This value must be obtained as part of the overall problem from the interaction between the boundary layer and the external flow.
Writing the external boundary condition for each boundary layer sweep as:

$$u_e(x) = u_e^i(x) + \delta u_e(x)$$

In this relation, $u_e^i(x)$ is the inviscid velocity resulting from a panel method and $\delta u_e(x)$ the perturbation in edge velocity due to the presence of the δ^*. This perturbation term can be derived from thin airfoil theory where a vertical velocity $v(x,0)$ is imposed on the $x-$axis between x_a and x_b. A potential flow solution for the horizontal velocity along the $x-$axis (based on complex function theory) can be determined as:

$$u(x,0) = \frac{1}{\pi}\int_{x_a}^{x_b} \frac{v(\sigma,0)}{x-\sigma}\mathrm{d}\sigma \tag{3.41}$$

From the conservation of mass it can be seen that $v \sim -y\frac{\mathrm{d}u_e}{\mathrm{d}x}$. Expanding v for large y as:

$$v(x,y) \sim -\frac{\mathrm{d}u_e}{\mathrm{d}x}y + v_1(x) + \ldots, \qquad y \to \infty$$

we observe that:

$$\begin{aligned} v_1(x) &= \lim_{y\to\infty}\left[v(x,y) + \frac{\mathrm{d}u_e}{\mathrm{d}x}y\right] \\ &= \lim_{y\to\infty}\left[\int_0^y \frac{\partial v}{\partial y}(x,y)\,\mathrm{d}y + \frac{\mathrm{d}u_e}{\mathrm{d}x}y\right] \\ &= \lim_{y\to\infty}\left[\int_0^y -\frac{\partial u}{\partial x}(x,y)\,\mathrm{d}y + \frac{\mathrm{d}u_e}{\mathrm{d}x}y\right] \\ &= \lim_{y\to\infty}\left[\int_0^y \left(\frac{\mathrm{d}u_e}{\mathrm{d}x} - \frac{\partial u}{\partial x}(x,y)\right)\mathrm{d}y\right] \\ &= \frac{\mathrm{d}}{\mathrm{d}x}\int_0^\infty (u_e - u)\,\mathrm{d}y = \frac{\mathrm{d}}{\mathrm{d}x}(u_e\delta^*) \end{aligned}$$

Thus, if equation 3.41 is rewritten to describe the perturbation effect of the boundary layer on the external flow, the following equation holds (often referred to as the 'Hilbert' integral):

$$\delta u_e(x) = \frac{1}{\pi}\int_{x_a}^{x_b} \frac{\mathrm{d}}{\mathrm{d}\sigma}(u_e\delta^*)\frac{\mathrm{d}\sigma}{x-\sigma}$$

3.4.4 Viscous effects in potential method

Mostly two approaches are used to incorporate viscous effects in the inviscid method. The first one uses a displaced surface and the second one is using a transpiration model. In figure 3.6 a schematic representation of the two methods can be seen. In the left subfigure, the real situation is seen. In the middle figure, the displacement method is seen for which the body coordinates are corrected by δ^*. In the right subfigure, a normal velocity is included at the wall. Both methods are equally valid but the latter one has the advantage that the body coordinates can stay the same.
In the first paragraph, the transpiration model will shortly be covered since it is used in ACTITRANS2D. Furthermore, the way in which finite trailing edges are handled is also covered in the paragraph thereafter.

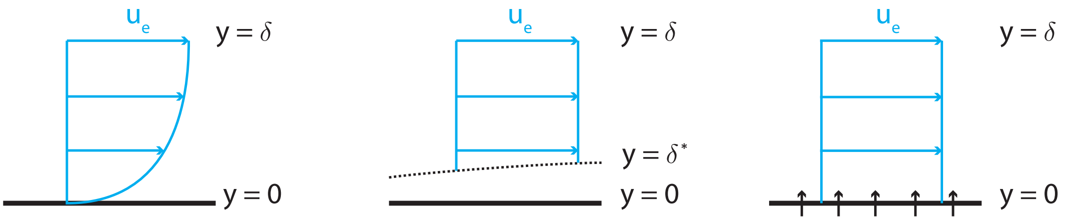

Figure 3.6: Including viscous effects.

Transpiration model

Both the transpiration and displacement surface model are based on first order boundary layer theory. This means that only thin boundary layers are considered as well as the fact that the normal pressure gradient can be neglected (see section 3.3).
To derive an expression for the normal velocity at the wall, consider the incompressible continuity equation for both the real (subscript r) and model (subscript m) case. Subtracting both leads to equation 3.42.

$$\frac{\partial}{\partial x}(u_r - u_m) + \frac{\partial}{\partial y}(v_r - v_m) = 0 \tag{3.42}$$

Integrating this relation from the wall to the edge of the boundary layer and making use of boundary conditions 3.43, equation 3.49 will result.

$$\begin{aligned} v_r &= 0 && y = 0 \\ v_r &= 0 && y = \delta \\ v_m &= v_n && y = 0 \\ v_m &= 0 && y = \delta \end{aligned} \tag{3.43}$$

$$\begin{aligned}\frac{\mathsf{d}}{\mathsf{dx}}\int_0^{\delta}(u_r-u_m)\,\mathsf{dy}+[v_r-v_m]_0^{\delta}=0\\ v_n=\frac{\mathsf{d}}{\mathsf{dx}}\int_0^{\delta}(u_m-u_r)\,\mathsf{dy}\end{aligned}\tag{3.44}$$

Now, use the fact that in the model $u_m = u_e$ (see figure 3.6), expression 3.49 can be rewritten as:

$$\begin{aligned}v_n&=\frac{\mathsf{d}}{\mathsf{dx}}u_e\int_0^{\delta}\left(1-\frac{u_r}{u_e}\right)\mathsf{dy}\\ &=\frac{\mathsf{d}}{\mathsf{dx}}\left(u_e\delta^*\right)\end{aligned}$$

Note that on the dividing streamline in the wake, a velocity jump should be imposed. This is defined as (v is measured positive in upward direction):

$$\Delta v_{\mathsf{wake}}=v_{m_{\mathsf{upper}}}-v_{m_{\mathsf{lower}}}=\frac{\mathsf{d}}{\mathsf{dx}}\left(u_{e_{\mathsf{upper}}}\delta^*_{\mathsf{upper}}\right)+\frac{\mathsf{d}}{\mathsf{dx}}\left(u_{e_{\mathsf{lower}}}\delta^*_{\mathsf{lower}}\right)$$

Now, to incorporate the viscous effects in the potential method, an iterative scheme is used. First, the potential flow is computed with a panel method. Then, by using the calculated velocities, the viscous calculation is performed. These effects are taken into account by using the described transpiration model and a new 'potential' flow is computed. This cycle is repeated until a converged solution exists.

Finite trailing edge

In practice, airfoils usually have a finite trailing edge for manufacturing reasons. To handle this in design tools, some corrections should be made to simulate this.

In XFOIL, the corrections that were made to simulate a finite trailing edge can be found in Drela [1989a]. In summary, the dimension of the trailing edge – h_{te} – is added to the displacement thickness in the wake:

$$\delta^*_{\mathsf{wake}}=\delta^*_{\mathsf{upper}}+\delta^*_{\mathsf{lower}}+h_{\mathsf{te}}$$

and an extra panel is placed over the finite trailing edge that contains a source. Also, several corrections are made to the closure relations that will not be repeated here.

In ACTITRANS2D, some similar ideas are used. First of all, the displacement thickness in the wake is corrected by closing the trailing edge (linearly) according to figure 3.7. Then the relations for the displacement thickness on the upper and lower side of the wake streamline can be written as:

$$\begin{aligned}\delta^*_{\mathsf{w_u}}&=\delta^*_{\mathsf{u}}+\mathsf{h}_1(x)\\ \delta^*_{\mathsf{w_l}}&=\delta^*_{\mathsf{l}}+\mathsf{h}_2(x)\end{aligned}$$

Furthermore, the drag coefficient is corrected for the so called base drag which can be written as (see Hoerner [1965]):

$$\Delta C_d=k\left(C_{d_0}\right)^{-\frac{1}{3}}\left(\frac{\mathsf{h_{te}}}{c}\right)^{\frac{4}{3}}$$

where C_{d_0} represents the uncorrected drag coefficient and k is a constant. This equation is an empirical relation. Note also that the geometry is changed when a finite trailing edge thickness is specified. This is explained in appendix B.

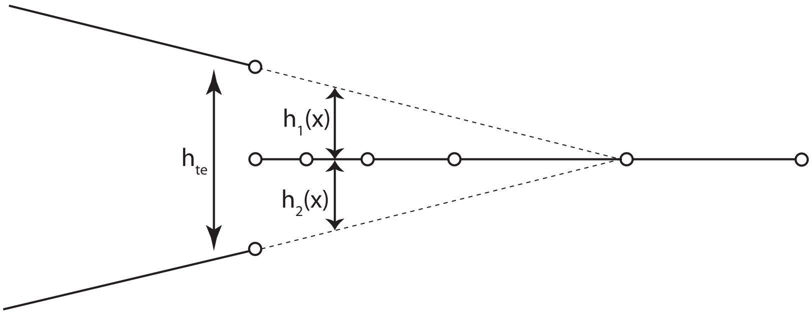

Figure 3.7: Closing the finite trailing edge.

3.5 Transition methods

The way in which a boundary layer moves from laminar to turbulent state is of crucial importance in predicting airfoil properties. Till now, there is no fundamental theory to describe transition and hence engineering prediction methods (empirical or semi-empirical) are frequently used.

If the onset of transition can be predicted by a certain method, it is known that the flow will not be turbulent instantly. There has to be a region where the turbulence grows and where the laminar boundary layer can developed to a turbulent one. How this effect is included in the numerical method is dependent on the way in which the boundary layer equations are solved.

In ACTITRANS2D, this effect has been modeled by multiplying the expressions for the eddy viscosity (see section 3.6) with a factor γ_{tr}. This factor will be zero for laminar flow (vanishing eddy viscosity) and one for fully turbulent flow. From Cebeci [2003], it is claimed that:

$$\gamma_{\text{tr}} = 1 - \mathrm{e}^{\left[-G(x-x_{\text{tr}})\int_{x_{\text{tr}}}^{x}\frac{\mathrm{d}x}{u_e}\right]} \tag{3.45}$$

where G is a spot-formation-rate parameter:

$$G = \left(\frac{3}{C^2}\right)\left(\frac{u_e^3}{\nu^2}\right)\mathrm{Re}_{x_{\text{tr}}}$$

The constant C is dependent on whether high Reynolds or low Reynolds number flow is considered.

What is left is to determine the onset of transition. In the past, many (engineering) methods were developed for this. For an overview, see White [2006]. In ACTITRANS2D, several options were explored. These options are shortly covered in the following paragraphs. As previously mentioned, transition is dependent on many variables and usually a certain method is only applicable to handle a few of them.

Michel's transition prediction

To start, a straightforward method was implemented proposed by Michel. For this method alone, several variations exist. It states that the variation of $\mathrm{Re}_{\theta_{\text{tr}}}$ – the transitional Reynolds number based on the momentum thickness – and Re_{x} is a universal curve. Originally, the empirical relation was valid for Reynolds numbers between $4 \cdot 10^5$ and $7 \cdot 10^6$ and described by:

$$\mathrm{Re}_{\theta_{\text{tr}}} = \frac{u_e(x)\,\theta(x)}{\nu} \approx 1.535 \cdot \mathrm{Re}_{\mathrm{x}}^{0.444}$$

According to Cebeci and Smith [1974], for higher values for the Reynolds number, the transition point can be determind by Smith and Gamberoni. Combining both leads to equation 3.46 and is valid for Reynolds numbers between $1 \cdot 10^5$ and $40 \cdot 10^6$.

$$\mathrm{Re}_{\theta_{\text{tr}}} \approx 1.174\left[1 + \left(\frac{22400}{\mathrm{Re}_{\mathrm{x}}}\right)\right]\mathrm{Re}_{\mathrm{x}}^{0.46} \tag{3.46}$$

Wazzan's transition prediction

In the search for a transition method that could be used in cases of suction, the present author applied the method of Wazzan et al. [1988] that is claimed to work for the effect of pressure gradient, surface heat transfer and suction. It is also called the $H - \mathrm{Re_x}$ method since it is based on the shape factor and the Reynolds number.
This method is not well verified with experiment but correlated with e^9 type calculations that are based on linear stability theory. It is described by the relation 3.47 and graphically illustrated in figure 3.8.

$$\log\left(\mathrm{Re}_{\mathrm{x_{tr}}}\right) \approx -40.4557 + 64.8066 \cdot H - 26.7538 \cdot H^2 + 3.3819 \cdot H^3 \tag{3.47}$$

Formula 3.47 is valid for shape factors between 2.1 and 2.8. This shape factor is first determined from the boundary layer calculation after which the locus is found with the formula from below. At this locus, the transitional Reynolds number can be found and compared with the local Reynolds number to determined wheter transition will occur or not.

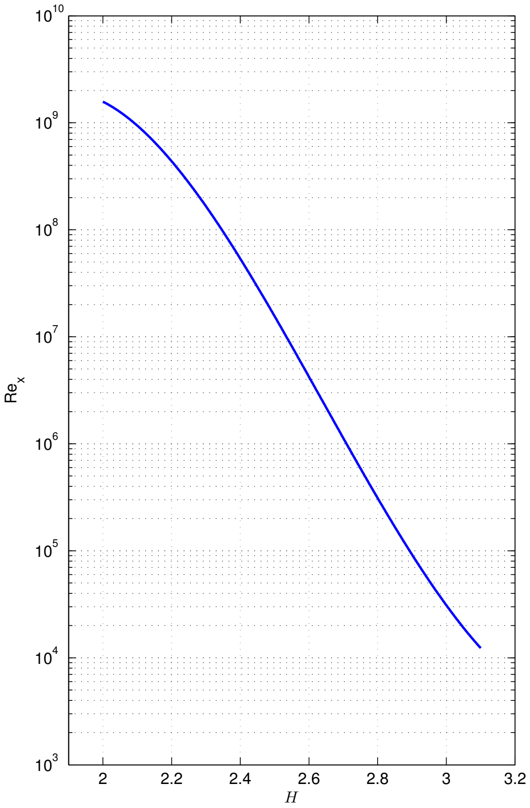

Figure 3.8: Wazzan's transition prediction.

Alternative methods

As another way of handling transition is setting transition to a fixed point. In practice, natural transition only occurs when the free stream is quiet and the surface is smooth. In reality, surfaces are often rough and contaminated and as a result, transition will occur in early stages. Using this way of specifying transition gives a very simplistic view on the real world but it provides a way to simulate contaminated surfaces and wind tunnel results where, for example, trip wires are used.

3.6 Modeling the eddy viscosity

In order to compute the velocity profile of a turbulent boundary layer, assumptions should be made to compute the Reynolds stresses. These stresses directly follow from the Reynolds averaging as performed in section 3.3. They result from the transport of mean momentum by the turbulent fluctuations.

Boussinesq was the first person to find a model for the Reynolds stresses by introducing the concept of eddy viscosity (Pope [2000]). He implied that the Reynolds (or turbulent) stresses are proportional to the velocity gradient by using the same analogy as for viscous stresses:

$$-\rho\overline{u'v'} = \rho\nu_t\left(\frac{\partial u}{\partial y}\right) \tag{3.48}$$

The constant ν_t is reffered to as the eddy viscosity with dimensions length times velocity (same as the kinematic viscosity). The difficulty now is that the eddy viscosity – as opposed to the kinematic viscosity – is not a property of the fluid but varies strongly across the flowfield.

Another related concept is the Prandtl mixing length. This length is a typical distance l that a turbulent eddy travels before dispersing (some analogy exists with the theory of mean free path λ for molecules). Note that l represents the largest eddies that dominate the turbulent momentum transport.

The relation between ν_t and l can be derived by considering two eddies moving through a shear layer as in figure 3.9. Both eddies are moving with constant total velocity **u**. It is illustrated that a positive v' results in a negative u' and vice versa. Thus, $\overline{u'v'} < 0$ for both eddies.

Furtermore, u' is assumed to be proportional to both the mixing length and velocity gradient and the turbulence is assumed to be isotropic:

$$u' \sim l \cdot \frac{\partial u}{\partial y} \qquad\qquad |u'| \approx |v'|$$

From this, relation 3.49 will follow.

$$-\overline{u'v'} \sim l^2\left(\frac{\partial u}{\partial y}\right)^2 \tag{3.49}$$

Now, comparing this with the assumption of Boussinesq in equation 3.48, the eddy viscosity can be written as expression 3.50.

$$\nu_t \sim l^2\left(\frac{\partial u}{\partial y}\right) \tag{3.50}$$

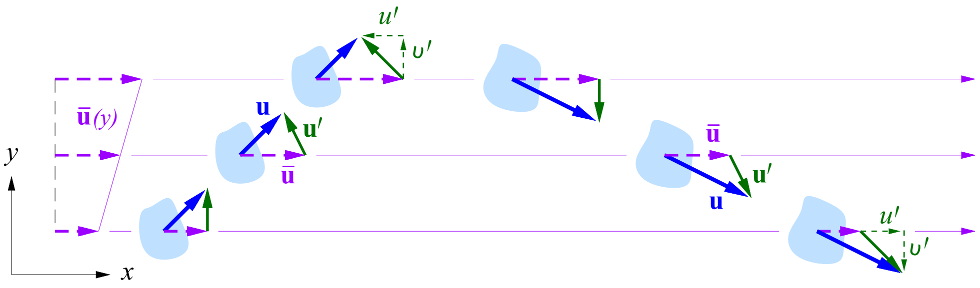

Figure 3.9: Two turbulent eddies travelling through a flow field. Based on Pope [2000].

In order to provide models for the mixing length in 3.50, the turbulent boundary layer is divided in several regions. These regions can be seen in figure 3.10.

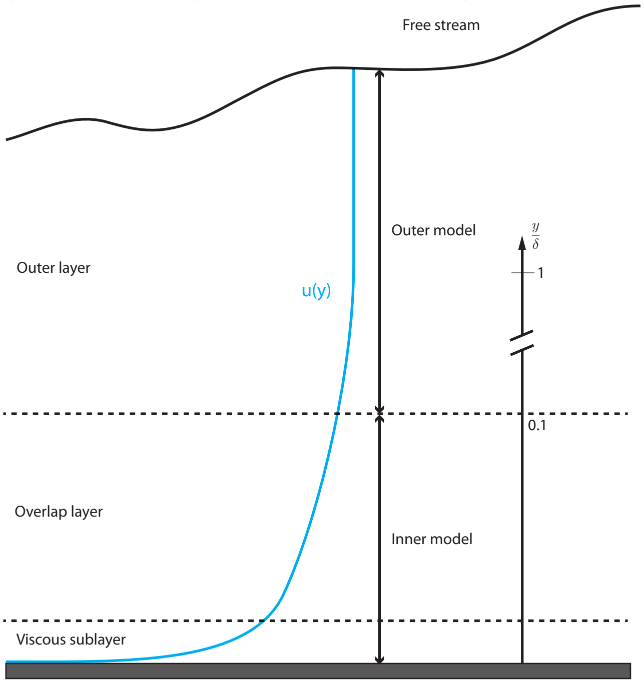

Figure 3.10: Schematic division turbulent boundary layer.

A widely used model is the one of Cebeci and Smith [1974]. Here, two relations are developed for the inner and outer layer of the turbulent boundary layer. These two relations can be seen in equation 3.51.

$$\begin{aligned}(\nu_t)_i &= l^2 \left|\frac{\partial u}{\partial y}\right| \gamma_{\mathsf{tr}} \\ (\nu_t)_o &= \alpha u_e \delta^* \gamma_{\mathsf{tr}} \gamma\end{aligned} \tag{3.51}$$

In these equations, γ represents the intermittency with the free stream flow, α is a constant between 0.016 and 0.02 and γ_{tr} is the parameter specifying whether the flow is laminar ($\gamma_{\mathsf{tr}} = 0$), turbulent ($\gamma_{\mathsf{tr}} = 1$) or somewhere inbetween (see section 3.5).
Moving towards the free stream, the turbulence becomes intermittent. This means that only a fraction γ of the time the flow is considered to be turbulent (see for example the clouds where a irregular but sharp boundary exist with the sky). This factor is determined by experiments and is found to be:

$$\gamma = \frac{1}{2}\left(1 - \mathrm{erf}\left(\zeta\right)\right) \qquad \text{where} \qquad \zeta = 5\left[\left(\frac{y}{\delta}\right) - 0.78\right]$$

Note that $(\nu_t)_o$ is now fully defined and that a mixing length relation for the inner layer should be found to close the relation for $(\nu_t)_i$. For this purpose, the mixing length model of van Driest will be used. This model is valid for the complete inner layer (Pope [2000]):

$$l = \kappa y \left[1 - \mathrm{e}^{\left(-\frac{y}{A}\right)}\right]$$

where κ is the von Kármán constant and A is a damping length. It is this damping length where the corrections for mass transfer at the wall and pressure gradient could be taken into account. Without corrections (negligible pressure gradient and no mass transfer), A narrows down to:

$$A = 26\left(\frac{\nu}{u_\tau}\right)$$

With this equation, the expressions for the eddy viscosity are fully defined. To correct for the pressure gradient and mass transfer, the possible empirical relations that are modeled in ACTITRANS2D will be outlined in the following paragraphs. For the outer layer model, the corrections with respect to mass transfer are included in δ^* and γ_{tr}.

For convenience, the pressure gradient, mass transfer parameter and wall shear velocity are written as:

$$p^+ = \left(\frac{\nu u_e}{u_\tau^3}\right)\left(\frac{\mathrm{d}u_e}{\mathrm{d}x}\right) \qquad v_w^+ = \frac{v_w}{u_\tau} \qquad u_\tau = \sqrt{\frac{\tau_w}{\rho}}$$

Kays et al. [1969]

In this attempt, the damping length is written as:

$$A = A^+\left(\frac{\nu}{u_\tau}\right)$$

and hence for the case without corrections, $A^+ = 26$. Kays et al. [1969] expressed the damping constant as a function of the pressure gradient and mass transfer as:

$$A^+ = \frac{26}{\left(1 + 5.9 v_w^+\right)} + f_1\left(p^+\right) + f_2\left(p^+, v_w^+\right) \tag{3.52}$$

where the empirical functions $f_1\left(p^+\right)$ and $f_2\left(p^+, v_w^+\right)$ are based on experimental data.

$$\begin{aligned} f_1\left(p^+\right) &= 1133p^+ && p^+ \leq 0.012 \\ &= 2133p^+ - 12 && p^+ > 0.012 \\ f_2\left(p^+, v_w^+\right) &= 1990\left[p^+\left(v_w^+\right)^{\frac{1}{4}}\right]^{1.10} && v_w^+ \geq 0 \\ &= 6.78\left(p^+\right)^{0.7}\left(-v_w^+\right)^{1.40} && v_w^+ < 0 \end{aligned}$$

Cebeci and Smith [1974]

In this approach, the damping length is written as:

$$A = \left(\frac{A^+}{N}\right)\left(\frac{\nu}{u_\tau}\right) \qquad \text{where} \qquad A^+ = 26$$

To correct for mass transfer, pressure gradient and possibly compressible flow, N is determined as:

$$N^2 = \left(\frac{\rho_e}{\rho_w}\right)^2 \frac{p^+}{v_w^+}\left[1 - \mathrm{e}^{\left(11.8 v_w^+\right)}\right] + \mathrm{e}^{\left(11.8 v_w^+\right)}$$

Kays and Moffat [1975]

In this endeavour, the effects of pressure gradient and mass transfer are modeled as:

$$A^+ = \frac{25.0}{a\left[v_w^+ + b\left(\frac{p^+}{1+cv_w^+}\right)\right] + 1.0}$$

where

$$\begin{array}{llllll} a = 7.1 & \text{if} & v_w^+ \geq 0.0 & \text{else} & a = 9.0 \\ b = 4.25 & \text{if} & p^+ \leq 0.0 & \text{else} & b = 2.0 \\ c = 10.0 & \text{if} & p^+ \leq 0.0 & \text{else} & c = 0.0 \end{array}$$

Besides the correction to the mixing length model for pressure gradient and mass transfer, the effect of roughness should also be taken into account. First of all, roughness only affects the inner region of the boundary layer. A surface can be considered as hydraulically smooth if the viscous sublayer thickness of the turbulent boundary layer (see figure 3.10) is much larger than the height of the roughness elements. By defining a roughness Reynolds number as:

$$k^+ = k\left(\frac{u_\tau}{\nu}\right)$$

where k is the characteristic roughness height, one can distinguish between three layers (for uniform sand-grain roughness):

Hydraulically smooth:	$k^+ < 5$
Transitionally smooth:	$5 \leq k^+ < 70$
Fully rough:	$k^+ \geq 70$

In Cebeci and Smith [1974], it is stated that the velocity profile for rough flow can be obtained from the smooth flow condition by shifting the independent variable in the van Driest formulation. This can be represented by the following set of equations.

$$u^+ = \int_0^{y^+} \frac{2}{1 + \left[1 + 4a\left(y^+\right)\right]^{\frac{1}{2}}} \mathrm{d}y^+$$

$$a\left(y^+\right) = \left(\kappa y^+\right)^2 \left[1 - \mathrm{e}^{-\left(\frac{y^+}{A^+}\right)}\right]^2 \qquad \text{smooth wall}$$

$$= \left(\kappa\left(y^+ + \Delta y^+\right)\right)^2 \left[1 - \mathrm{e}^{-\left(\frac{\left(y^+ + \Delta y^+\right)}{A^+}\right)}\right]^2 \qquad \text{rough wall}$$

In these equations, Δy^+ is heavily dependent on empirical data. For sand-grain roughness this shift is determined by:

$$\Delta y^+ = 0.9\left[\sqrt{k^+} - k^+ \mathrm{e}^{\left(-\frac{k^+}{6}\right)}\right]$$

3.7 Sink drag

An interesting phenomenon that comes along with mass transfer along the surface is the drag that is caused by removal of the fluid. According to Schlichting and Gersten [2000], this type of drag – the sink drag – is experienced by every body, even in inviscid flow.
Since there is still debate on how to include this drag, this section will clarify how to treat the sink drag. Subsection 3.7.1 will show whether the sink drag is already included in the drag formulation or should be accounted for separately. This has been done by applying the conservation of mass and momentum on several control volumes. In this analysis, a flat plate surface is considered as well as steady and incompressible flow without body forces.

3.7.1 A separate drag?

To answer this question, sufficiently large control volumes are considered along a flat plate with and without mass transfer along the surface. Using the plate will ensure that the pressure on each boundary of the control volume is constant and hence this term will vanish in the momentum equation (integral of surface vector on closed surface is zero). Using the aforementioned assumptions, the drag per unit meter span follows from the momentum equation as:

$$\mathsf{D}' = -\oiint (\rho \mathbf{V} \cdot \mathbf{dS})\, \mathsf{u} \tag{3.53}$$

Furthermore, the continuity equation can be written as:

$$\oiint \rho \mathbf{V} \cdot \mathbf{dS} = 0 \tag{3.54}$$

Note that since the control volumes have unit depth, the surface integral becomes a line integral.

Situation I

In this case, the plate without mass transfer is considered as illustrated in figure 3.11. Applying equation 3.54 leads to:

$$\begin{gathered} -\int_A^B (\rho u)\, \mathsf{dy} + \int_C^D (\rho u)\, \mathsf{dy} = 0 \\ -\rho u_e \left(h_1 - \delta_1^*\right) + \rho u_e \left(h_2 - \delta_2^*\right) = 0 \\ h_2 - h_1 = \delta_2^* - \delta_1^* \end{gathered} \tag{3.55}$$

Equation 3.53 can now be written as:

$$\begin{aligned} \oiint (\rho \mathbf{V} \cdot \mathbf{dS})\, \mathsf{u} &= -\int_A^B (\rho u^2)\, \mathsf{dy} + \int_C^D (\rho u^2)\, \mathsf{dy} \\ &= -\rho u_e^2 \int_A^B \left(\frac{u}{u_e}\right)^2 \mathsf{dy} + \rho u_e^2 \int_C^D \left(\frac{u}{u_e}\right)^2 \mathsf{dy} \\ &= -\rho u_e^2 \left(h_1 - \theta_1 - \delta_1^*\right) + \rho u_e^2 \left(h_2 - \theta_2 - \delta_2^*\right) \\ \mathsf{D}_\mathsf{I}' &= \rho u_e^2 \left(h_1 - h_2 - \theta_1 + \theta_2 - \delta_1^* + \delta_2^*\right) \\ &= \rho u_e^2 \left(\theta_2 - \theta_1\right) \end{aligned} \tag{3.56}$$

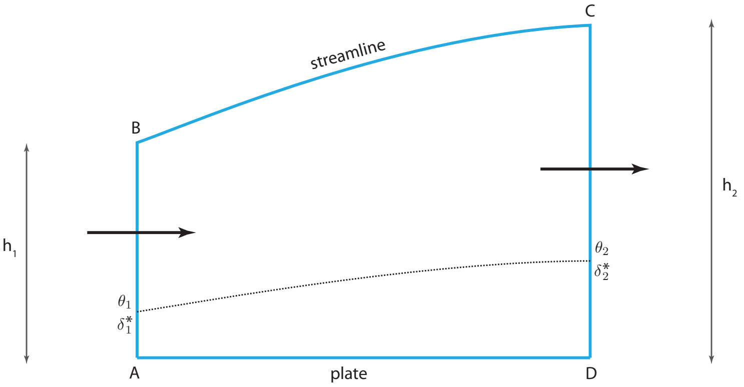

Figure 3.11: Control volume situation I.

Situation II

For the second case, the flat plate with mass transfer is considered. This is shown in figure 3.12.

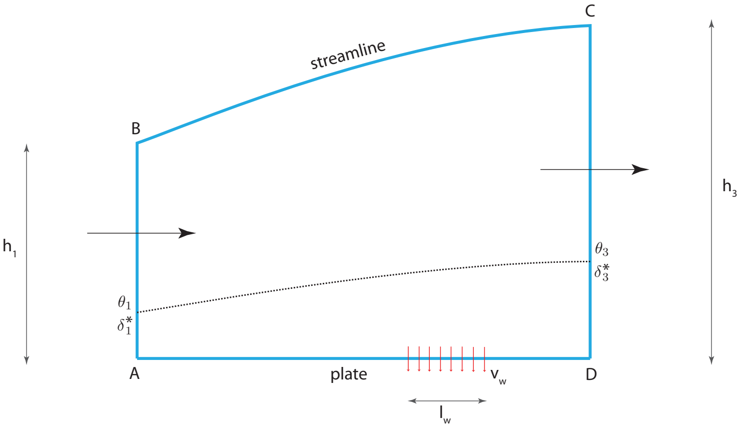

Figure 3.12: Control volume situation II.

Applying equation 3.54 now leads to:

$$\begin{aligned} -\int_A^B (\rho u)\,\mathrm{dy} + \int_C^D (\rho u)\,\mathrm{dy} + \int_D^A (\rho v_w)\,\mathrm{dx} = 0 \\ -\rho u_e\left(h_1 - \delta_1^*\right) + \rho u_e\left(h_3 - \delta_3^*\right) + \rho v_w l_w = 0 \\ h_3 - h_1 = \delta_3^* - \delta_1^* - \frac{v_w l_w}{u_e} \end{aligned} \tag{3.57}$$

Formula 3.53 becomes:

$$\begin{aligned} \oiint \left(\rho \mathbf{V}\cdot\mathbf{dS}\right)\mathrm{u} &= -\int_A^B \left(\rho u^2\right)\mathrm{dy} + \int_C^D \left(\rho u^2\right)\mathrm{dy} + \int_D^A \left(\rho v_w \cdot (0)\right)\mathrm{dx} \\ &= -\rho u_e^2\left(h_1 - \theta_1 - \delta_1^*\right) + \rho u_e^2\left(h_3 - \theta_3 - \delta_3^*\right) \\ \mathrm{D}'_{\mathrm{II}} &= \rho u_e^2\left(h_1 - h_3 - \theta_1 + \theta_3 - \delta_1^* + \delta_3^*\right) \\ &= \rho u_e^2\left(\frac{v_w l_w}{u_e} + \theta_3 - \theta_1\right) \end{aligned} \tag{3.58}$$

Comparing the two situations result in:

$$\begin{aligned}\Delta \mathsf{D}' = \mathsf{D}'_{\mathsf{II}} - \mathsf{D}'_{\mathsf{I}} &= \rho u_e^2 \left(\theta_3 - \theta_2 + \frac{v_w l_w}{u_e}\right) \\ &= \rho u_e^2 \left(\theta_3 - \theta_2\right) + \rho v_w l_w u_e \\ \Delta C_d = \frac{\Delta \mathsf{D}'}{\frac{1}{2}\rho u_e^2 c} &= \frac{2}{c}\left(\theta_3 - \theta_2\right) + 2\frac{v_w l_w}{u_e c}\end{aligned} \tag{3.59}$$

From 3.59 one can see that the difference in drag (coefficient) result from the different boundary layer momentum thickness as well as the extra term due to removal of the fluid. Since the formulation for the drag coefficient is based on the boundary layer properties (Squire-Young formula), this standalone term should be accounted for separately. Note that although it should be accounted for separately, it is not considered as a separate kind of drag. The drag occurs as a result of the momentum loss of the fluid. One part disappears (or appears) through mass transfer at the surface and one part disappears due to the momentum loss in the boundary layer (momentum thickness). So the answer posed at the beginning of this section is 'no' but it should be accounted for separately in the drag formulation.

3.7.2 General

In subsection 3.7.1, the flat plate with constant suction was considered to show the separate contribution of the sink drag. In reality, variable mass transfer could be applied along the (possibly curved) surface and the removed air could be injected back in the free stream flow. Assuming that the reinjection speed equals u_3, the sink drag term can be written as (Terry [2004]):

$$\begin{aligned}D_s &= \rho Q_s \left(u_\infty - u_3\right) \\ Q_s &= \int_0^1 -v_w \mathsf{ds}\end{aligned} \tag{3.60}$$

Note that, if suction is applied, v_w becomes negative. The sink drag coefficient is now defined as:

$$C_{d_s} = \frac{D_s}{\frac{1}{2}\rho u_\infty^2 c} = \frac{2Q_s}{u_\infty c}\left(1 - \frac{u_3}{u_\infty}\right) \tag{3.61}$$

Defining the suction flow coefficient as:

$$C_q = \frac{Q_s}{u_\infty c} \tag{3.62}$$

One can write the sink drag coefficient as a function of the suction flow coefficient and the reinjection velocity:

$$C_{d_s} = 2C_q\left(1 - \frac{u_3}{u_\infty}\right) \tag{3.63}$$

From equation 3.63 it can be seen that the sink drag can be removed by reinjecting the air with free stream velocity (balancing the momentum loss due to removal of the fluid). If no reinjection takes place and constant suction is applied, one retrieves the same sink drag term as seen in equation 3.59.

CHAPTER

FOUR

Code architecture ActiTrans2D

The overall code architecture can be found in the diagram presented in figure 4.1. Each block is then converted to a new block diagram to elaborate on the architecture a bit more. These blocks are found in appendix A.

ACTITRANS2D is based on the theory and practical examples (FORTRAN codes) as explained in the book series of prof. Cebeci and his associates (see Cebeci and Smith [1974], Cebeci and Bradshaw [1977], Cebeci and Cousteix [2005], Cebeci et al. [2005a], Cebeci et al. [2005b], Cebeci [2002], Cebeci [1999], Cebeci [2004a] and Cebeci [2004b]). This professor has an outstanding track record in the field of CFD and more than fourty years experience in boundary layer flows. Each block in figure 4.1 has been modified with respect to the approach of prof. Cebeci for various reasons. These modifications can be found in the lightyellow shaded blocks in the figures of appendix A.

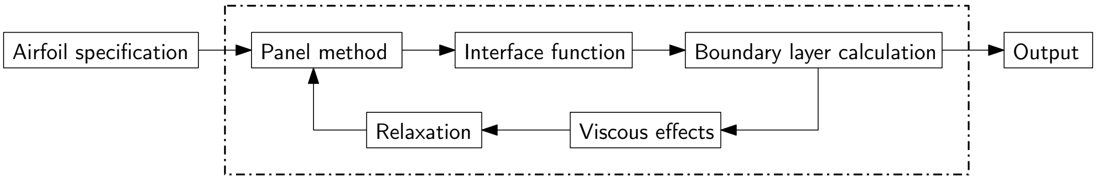

Figure 4.1: Main code architecture.

Between the extremes of fully attached flow and fully separated flow lies a wide range of practical important flows. From figure 4.1 it can be seen that the calculations are arranged in an iterative manner. Each successive inviscid solution provides the pressure distribution for the next boundary layer computation. After each boundary layer computation, the displacement effect is taking into account via the transpiration model to change the boundary conditions in the inviscid panel method. This 'cycle' must be repeated until convergence is obtained.

For now, each block will be discussed briefly and the reader will be referred to the corresponding location in the report for more information.

4.1 Airfoil specification

To start a simulation, a certain geometry should be defined or read in via a coordinate file. Next to this, the free stream conditions should be defined by implementing a certain free stream Reynolds and Mach number. A schematic overview of the options can be found in figure A.1. Note that if data is read in from a coordinate file, the coordinates should run from the lower trailing edge to the upper trailing edge around the contour.

If a NACA body is specified, several extra options exist. The number of panels, a finite or closed trailing edge thickness as well as the option to re-distribute the panels. All these options are explained in appendix B.

4.2 Panel method

As illustrated in figure A.2, the Hess–Smith panel method is used to compute the potential flow. This method is explained in chapter 2. Note that the matrix system is solved by built in MATLAB routines.

4.3 Interface function

By using the MATLAB interface function as represented in figure A.3, the connection between the potential method and the boundary layer calculation can be made. First, the stagnation point is identified by identifying where the velocity switches from negative to positive (by running from the lower trailing edge to the upper trailing edge).

After this, the contour is divided in an upper and lower surface boundary layer by starting from the stagnation point. These coordinates are then used in the boundary layer calculation.

4.4 Boundary layer calculation

This aspect of ACTITRANS2D is probably the most involved and most modified with respect to the approach of prof. Cebeci. A graphical overview of the changes that were made can be found in figure A.4. For details about the solution method as well as the corrections to model various effects, the reader is referred to chapter 3.

A finite difference method is used and solved by using built in MATLAB functions. It is here where ways are sought to properly model boundary layer mass transfer.

4.5 Viscous effects

To model the effects of the boundary layer in the potential flow method, a transpiration model is used. This means that a non zero velocity is imposed at each mid panel point (or control point) to simulate the displacement thickness. In this way, the geometry of the body can stay the same. Different relations are used for the airfoil surface and wake as can be seen in figure A.5.

Besides the effect of the boundary layer, ways to treat a finite trailing edge are also included. Details for both viscous effects are found in subsection 3.4.4.

4.6 Relaxation

At several locations in the program, iterations are used to converge to a certain solution. To speed up this convergence or to enhance numerical stability, relaxation could be used. This is illustrated in figure A.6.
Under relaxation is used by controlling the jump in the profiles for f, u and v. At certain locations (for example at transition or at separating flow) this jump can be large and numerical instabilities can grow leading to diverging solutions. By multiplying the jump with a relaxation factor, this growth can be suppressed.

4.7 Output

This part can be divided in the boundary layer output parameters and the airfoil properties. The most important boundary layer properties were derived in section 3.2. The most important airfoil properties are the pressure, lift and drag coefficient. With respect to the approach of prof. Cebeci, the drag coefficient is extended with the base drag to account for a finite trailing edge thickness and the sink drag to account for mass transfer along the surface. All of this can be seen in figure A.7.

CHAPTER
FIVE

Flat plate validation

In order to check the corrections that were made in ACTITRANS2D to model mass transfer along the surface, a proper validation procedure should be carried out. First of all, analytical results for a laminar flat plate with transpiration are present in literature. In this way, a check can be carried out on the implementation of the new boundary conditions and changes to the output relations. To validate the effects of transpiration on the turbulence model, experimental results of McQuaid [1967] and Favre et al. [1961] will be used since there are no analytical relations to the describe the turbulent boundary layer with mass transfer. If these effects are modeled satisfactorily, the corrections for the pressure gradient and roughness can be implemented. In this way, airfoils with transpiration can be analyzed which will be the topic of chapter 6.

5.1 Laminar flat plate

The model of the flat plate in ACTITRANS2D is set up to represent a mathematical flat plate. This means that it has zero thickness and zero pressure gradient leading to a constant horizontal inviscid velocity. The analytical relations for the laminar flat plate with uniform suction are derived in appendix F to be:

$$\begin{gathered} \frac{u(\eta)}{u_\infty} = 1 - e^{\left(F\eta\sqrt{Re_x}\right)} \\ \delta^* = -\frac{x}{Re_x F} \qquad \theta = \frac{1}{2}\delta^* \qquad C_f = -2F \end{gathered} \tag{5.1}$$

This result automatically means that the shape factor should asymptotically go to two. To compare results for cases without mass transfer (bottom of the plate), the following formulae are used (Blasius laminar flat plate boundary layer – see Anderson [2007] and Schlichting and Gersten [2000]):

$$\delta^* = \frac{1.72x}{\sqrt{Re_x}} \qquad \theta = \frac{0.664x}{\sqrt{Re_x}} \qquad C_f = \frac{0.664}{\sqrt{Re_x}} \tag{5.2}$$

To capture most aspects of the laminar flat plate with and without transpiration, several plots are created. First of all, uniform suction (three promille and a Reynolds number, Re_c, of three million) has been applied on the upper surface of the plate and transition is set at the trailing edge such that the flow will be laminar on the full length of the plate. These numerical results can be compared with equations 5.1. The results for the lower surface are compared with equations 5.2. The resulting plots in figure 5.1 till 5.5 are showing the results for δ^*, θ, H, C_f and the velocity profiles on the upper surface. In each of the figures, the symbols are representing the results from ACTITRANS2D and the lines are representing theory.

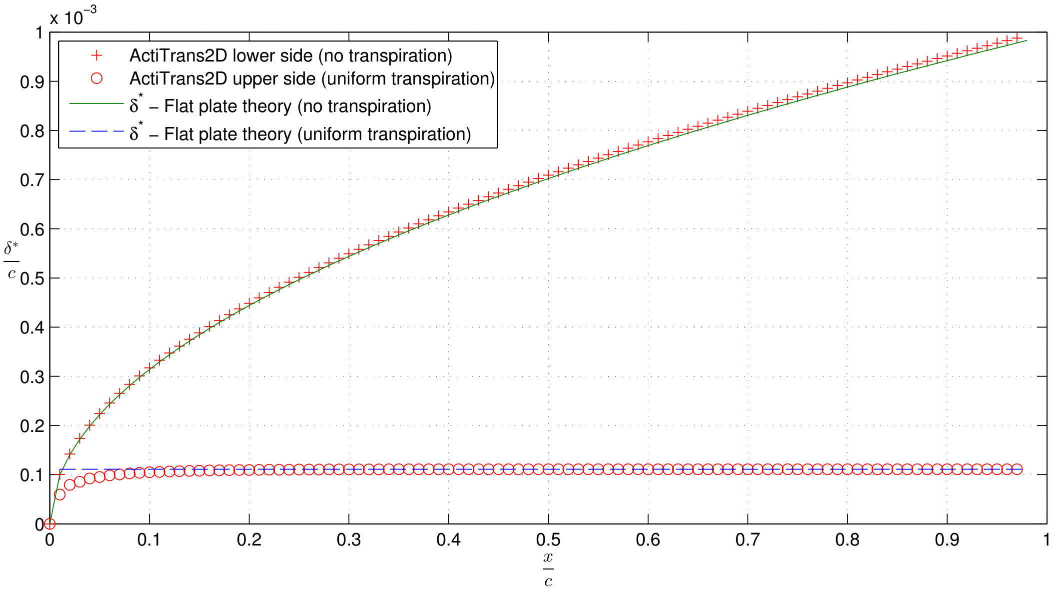

Figure 5.1: Laminar flat plate displacement thickness distribution.

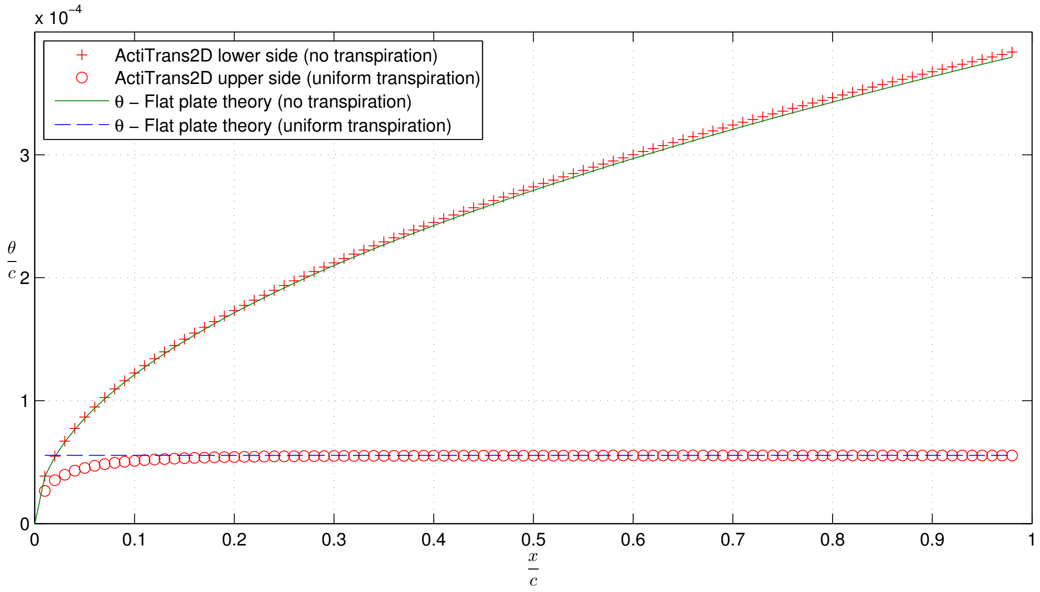

Figure 5.2: Laminar flat plate momentum thickness distribution.

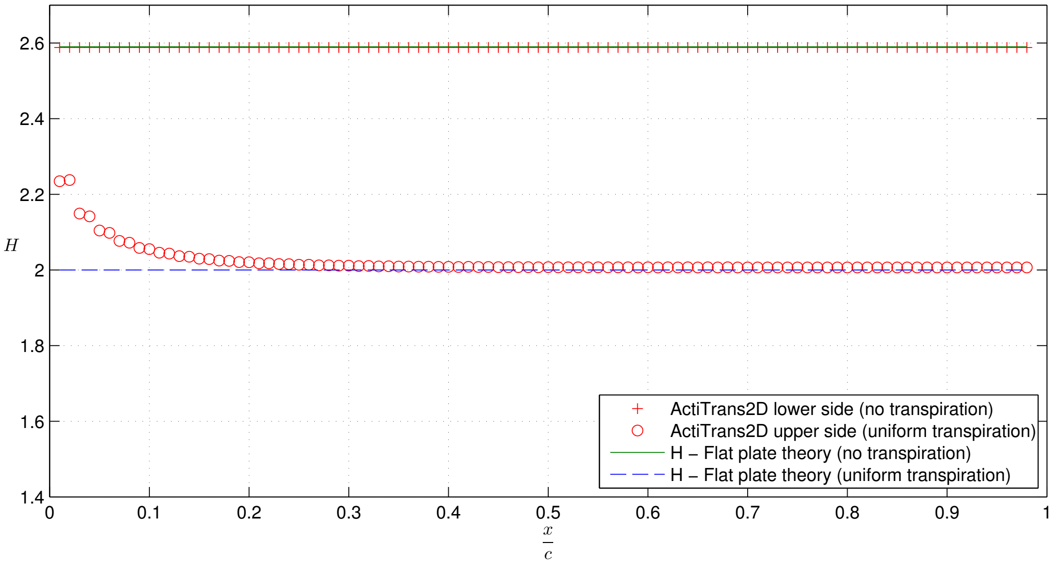

Figure 5.3: Laminar flat plate shape factor distribution.

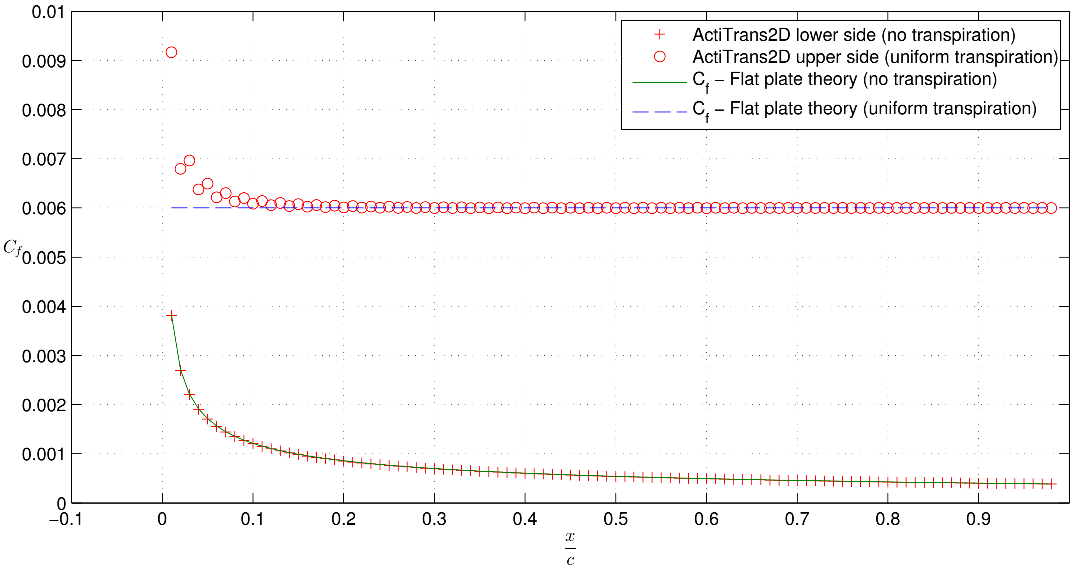

Figure 5.4: Laminar flat plate skin friction coefficient distribution.

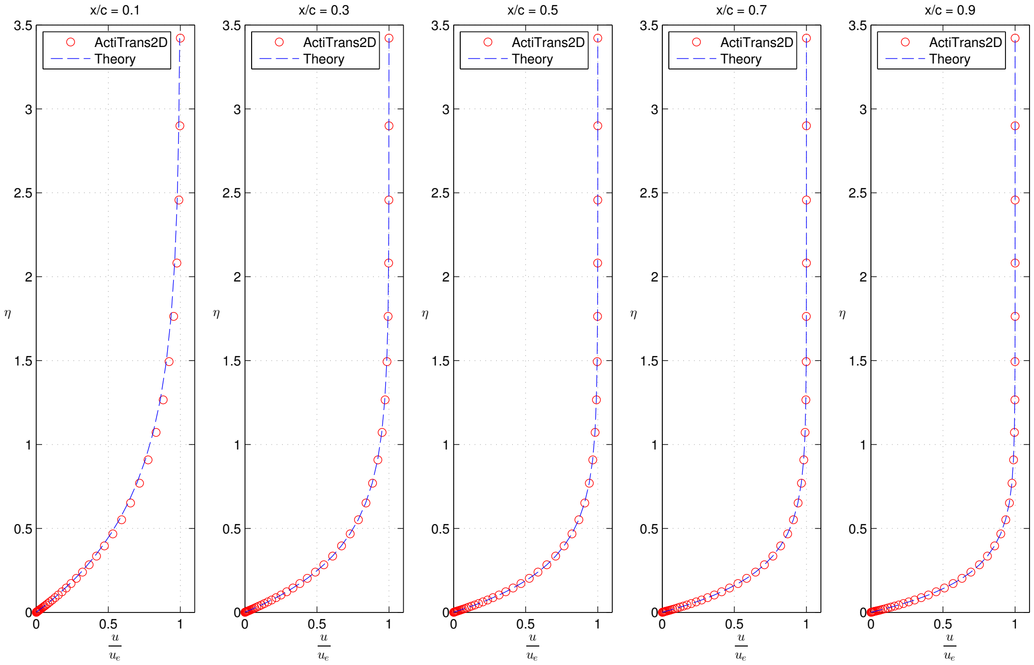

Figure 5.5: Laminar flat plate velocity profiles.

Observing the figures, interesting things may be noticed. Considering the upper surface with uniform suction, it can be seen that the idealized flow does not exist close to the leading edge of the plate, even though uniform suction starts at the leading edge. After a certain distance downstream the asymptotic suction will materialize. This distance is determined by Iglisch [1949] to be:

$$-\frac{v_w}{u_\infty}\left(\frac{u_\infty x}{\nu}\right)^{\frac{1}{2}} = -\frac{v_w}{u_\infty}\sqrt{\mathrm{Re}_c \cdot \xi} - 2 = 0$$

Thus, the asymptotic state can be reached earlier if the free stream Reynolds number Re_c and/or suction value v_w/u_∞ is increased.
From 3.24 (with $w = 1$ and $c = 1$) it follows that for the flat plate:

$$f_w(\xi) = -\frac{v_w}{u_\infty}\sqrt{\mathrm{Re}_c \cdot \xi}$$

Thus the distance at which the asymptotic suction profile exist is at the location where $f_w = 2$. It can be seen that the laminar theory is approached closely in all of the cases meaning that the corrections to the boundary conditions and output relations in ACTITRANS2D are implemented well. Note indeed that the asymptotic value for the momentum thickness is half of this value for the displacement thickness and that the skin friction coefficient and shape factor are converging to the correct theoretical values.
Note that when $x \to 0$, the Blasius profile should be approached and the shape factor should asymptotically go to the value 2.59 (divide δ^* with θ in equation 5.2). Due to the fact that a rather coarse and uniform grid is taken along the plate, this asymptotic behaviour is not well observed near $x = 0$ in figure 5.3. To show that this behaviour is actually present, a shape factor plot is created in figure 5.6 by taking more points along the plate.

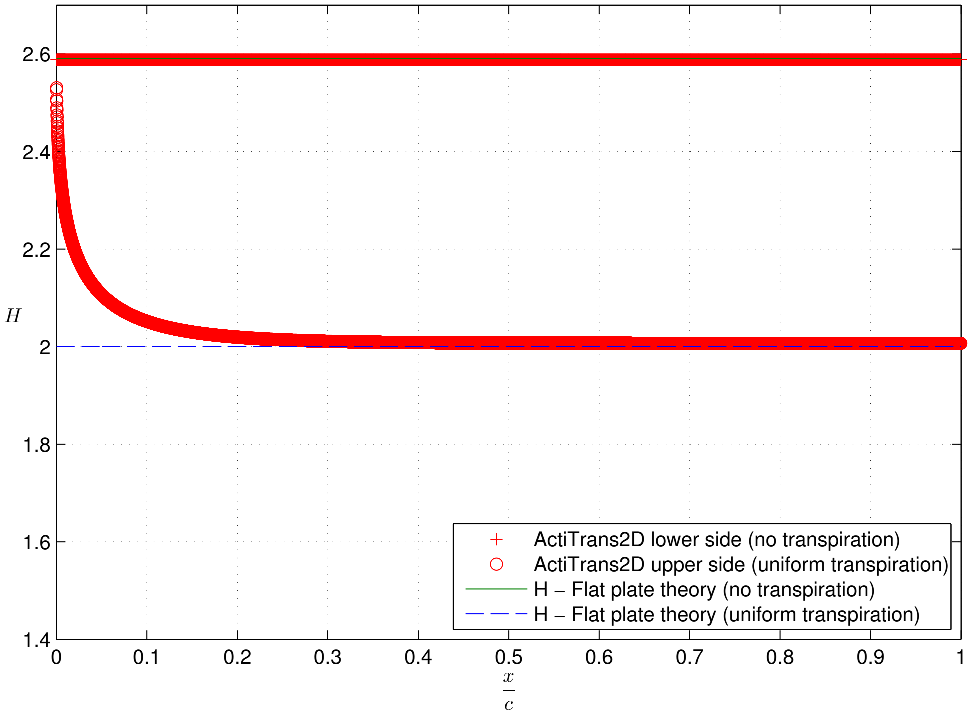

Figure 5.6: Laminar flat plate shape factor distribution. Increased number of panels.

Considering the lower surface without mass transfer it can be seen that the agreement is good with the Blasius laminar flat plate boundary layer although the difference gets slightly larger when moving towards the end of the plate.

5.2 Turbulent flat plate

Validation of the turbulence model for transpiration is a lot harder than the previous laminar flat plate with transpiration. The main reason for this is the dependency on empirical data. If there is some data present, it is still very hard to accurately simulate the same conditions at which the experiments were performed (for example the turbulence level of the wind tunnel and roughness level of the transpired surface).

The numerical results for the turbulent flat plate with transpiration from ACTITRANS2D have been compared to experimental data from McQuaid [1967] and Favre et al. [1961]. For these simulations, transition is set to the first station to ensure turbulent flow is present over the full length of the plate. In McQuaid [1967], the velocities across the boundary layer were measured by means of pitot tubes and he tabulated data is not corrected for the pitot probe placement. In Favre et al. [1961], suction was not applied from the start of the plate but from halfway on. This makes it difficult to set the same initial conditions at the start of suction. Furthermore it was not clear at what turbulence level and roughness these measurements were taken.

To compare with the blowing experiments of McQuaid [1967], coordinates of a flat plate were read in by ACTITRANS2D instead of creating a mathematical flat plate. In reality, the pressure gradient will not be exactly zero and a peak will be present at the location near the leading edge of the plate. The case where the freestream velocity was 150 [ft/s] (about 46 [m/s]) and $F = 0.0032$ has been chosen.

To get a feeling of the influence of wall roughness on the turbulent boundary layer, three values for k^+ were chosen. The results can be seen in figures 5.7 till 5.9. The correction to the turbulence model for transpiration was taken from Kays and Moffat [1975]. The symbols now represent the measurement data and the dashed lines the numerical results from ACTITRANS2D.

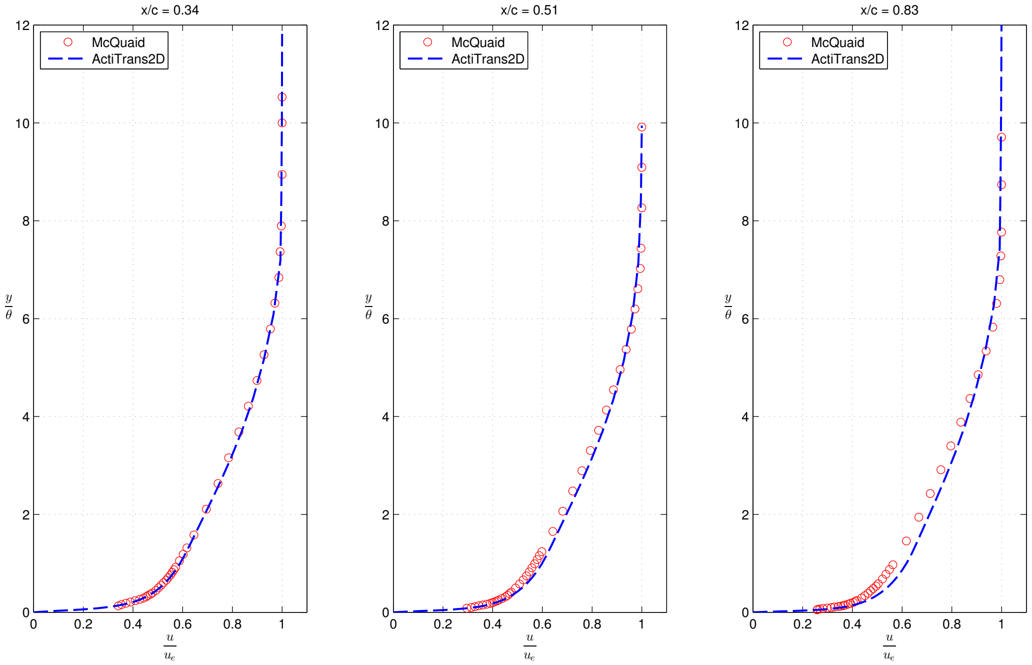

Figure 5.7: Velocity profile comparison between ACTITRANS2D and McQuaid [1967] – Smooth flat plate, $k^+ = 0$.

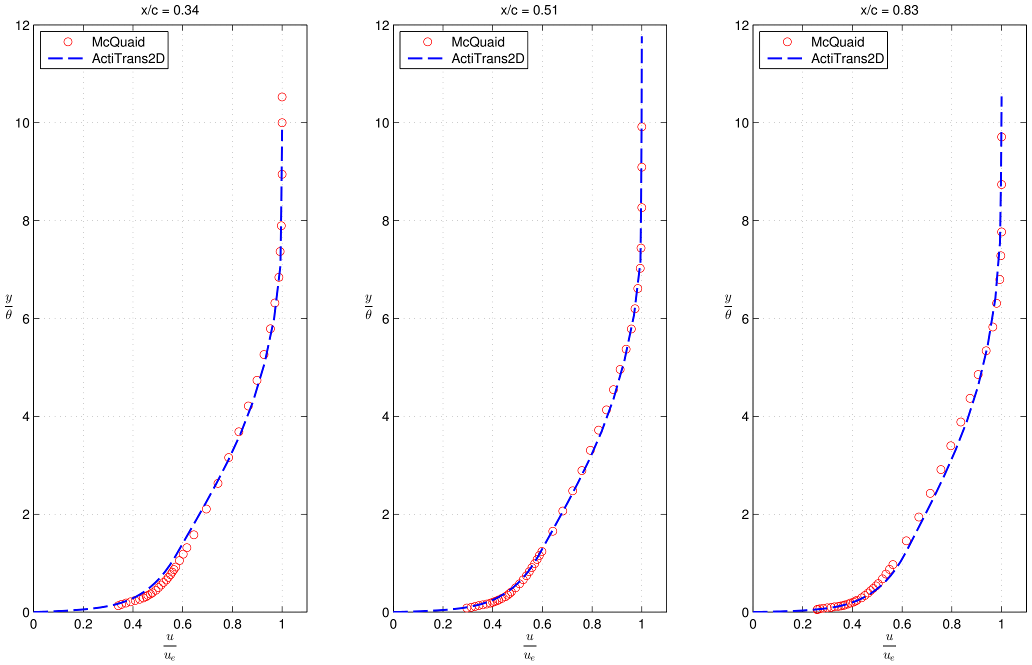

Figure 5.8: Velocity profile comparison between ACTITRANS2D and McQuaid [1967] – Transitionally rough flat plate, $k^+ = 30$.

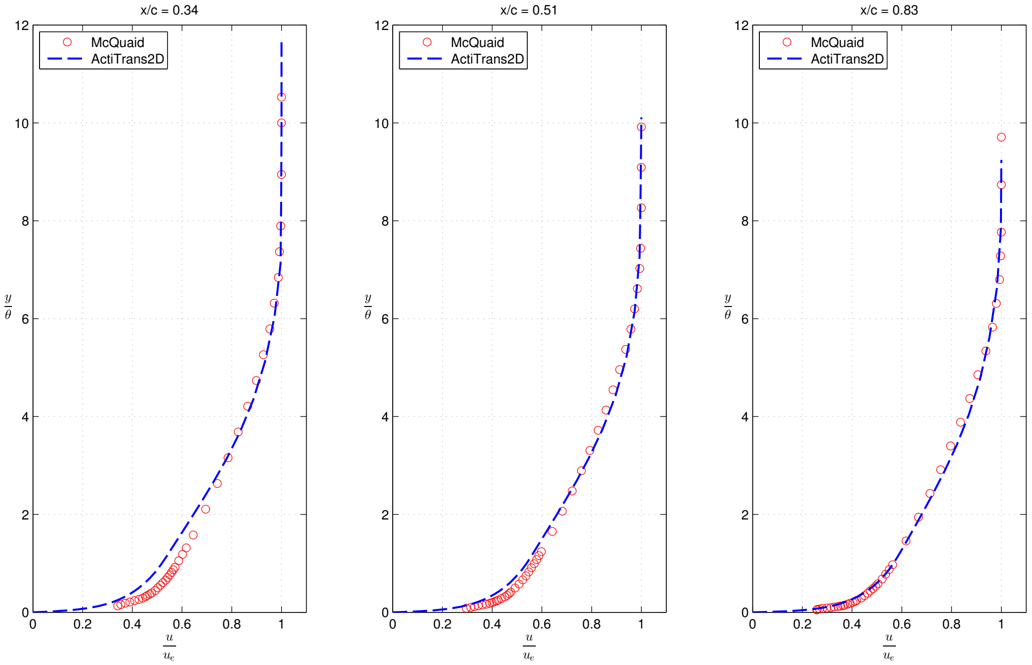

Figure 5.9: Velocity profile comparison between ACTITRANS2D and McQuaid [1967] – Fully rough flat plate, $k^+ = 90$.

Note that this time, the vertical axis represents the physical $y-$coordinate normalized with the momentum thickness at that location. Note that with increased roughness, the velocity profile is 'pushed away' from the surface. Observe that figure 5.7 has the best correspondence with the first location, figure 5.8 with the second location and figure 5.9 with the third location. This trend can be explained. Since the boundary layer thickness grows along the plate, the roughness elements must be larger to have the same effect on a thinner boundary layer (or, in other words, a plate can start as aerodynamically rough and end aerodynamically smooth). Hence, to obtain the same influence along the boundary layer, the value for k^+ should increase.

Overall, the agreement between the simulated and measured velocity profile is quite good. If compared to the case without mass transfer (for clarity not shown in the figures, one observes that – with this transpiration distribution – the velocity gradient near the wall is reduced (leading to a lower value for the wall shear stress) and a 'less full' velocity profile will develop. To further judge the modifications for mass transfer in the turbulent boundary layer, it would be nice to have extensive data sets availabe. Since this is not the case, relatively old measurement data from Favre et al. [1961] will be used. Although these data sets are not so extensive and the measurement conditions are not exactly known, it can still be used to compare with ACTITRANS2D and see the effect of suction on a turbulent boundary layer. The same flat plate coordinates and turbulence model as in the comparison with McQuaid [1967] will be used. The lower side of the plate (without suction) will also be used to compare with the skin friction coefficient formula (Schlichting and Gersten [2000] and White [2006]):

$$C_f = \frac{0.027}{Re_x^{\frac{1}{7}}} \tag{5.3}$$

This formula is derived from the momentum-integral relation where zero pressure gradient is imposed and assumed velocity profiles were used (since it is equilibrium flow, a wall-wake velocity profile (Coles [1956]) gives an accurate description).

The comparison of the simulated velocity profiles can be seen in figure 5.10. As can be seen, the simulated profiles and experimental data are quite off although the effect of suction (larger velocity gradient near the wall and a 'fuller' profile) can be clearly observed. The measurement data was taken from the case where the freestream velocity was 11 [m/s] and $F = -0.0052$. A smooth wall was simulated ($k^+ = 0$) and the location where the measurement data and simulated profiles were generated was at 0.4 [m] after the start of the suction region. Since the reference length is about two meter (the length of the total plate), the Reynolds number is taken to be 1.4 million. Reasons for the discrepancy between measurement and simulations are various. Most likely, the external conditions should be tuned to the measurement settings which are not known in detail to the author.

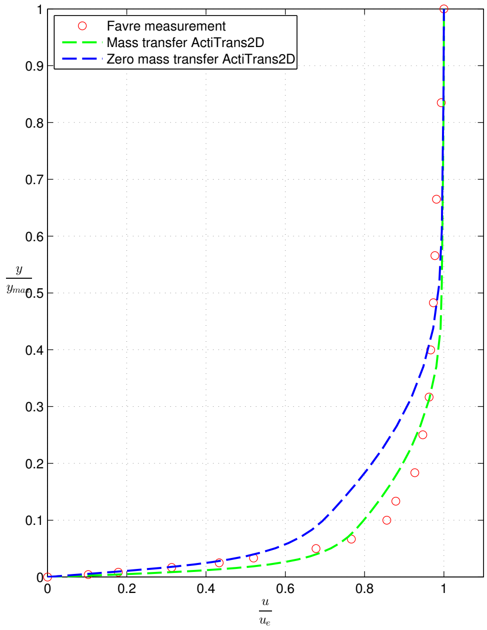

Figure 5.10: Velocity profile comparison between ACTITRANS2D and Favre et al. [1961].

The skin friction coefficient comparison on both surfaces can be found in figure 5.11.

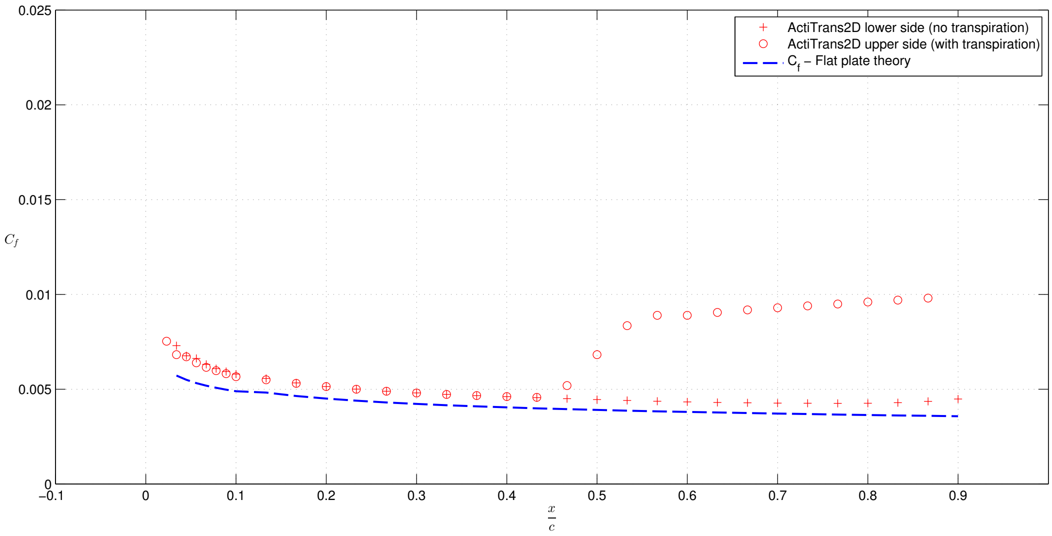

Figure 5.11: Skin friction comparison between ACTITRANS2D and theory.

Note that since formula 5.3 was based on zero pressure gradient, only the region where approximately zero pressure gradient flow can be assumed is plotted (small regions near the leading and trailing edge regions left out). Observe that the skin friction coefficient for the turbulent boundary layer along a flat plate without mass transfer is predicted a bit larger in ACTITRANS2D than in theory. Exact reasons for this are not known yet, but most likely it has to do with the uncertainty in setting the external conditions. In figure 5.11, also the skin friction coefficient on the upper side of the plate is plotted. It can be seen that when the applied suction region is reached, the skin friction coefficient will – as expected – increase significantly.

The purpose of simulation is insight, not numbers.

Oscar Buneman, 1986

CHAPTER
SIX

Airfoils with transpiration

6.1 Effect transpiration distributions: NACA 0012

Before setting up test cases to see the overall effect of transpiration on airfoils with different computational methods, it is useful to explore the effects of different transpiration distributions along the surface determined by ACTITRANS2D.

In this section, different transpiration distributions will be applied on a NACA 0012 airfoil under an angle of attack of six degrees. A full case description can be found in subsection 6.1.1. Transpiration will be applied in the laminar region (from the leading edge forward) to postpone transition as well as in the turbulent region to stay further away from massive separation. In total, sixteen transpiration distributions will be considered at the upper surface. The results that were found are presented in subsection 6.1.2 and discussed in subsection 6.1.3.

6.1.1 Case description

The settings for ACTITRANS2D for which the results were generated can be found in table 6.1. Note that the transpiration distributions are divided in four blocks. The first block, v_0 to v_3, contains the comparison of a transpiration distribution between $0.5 \leq \frac{x}{c} \leq 0.7$ with varying – but constant over the interval – transpiration strength. The second block, v_4 to v_7, is a constant transpiration strength between various locations. The third block, v_8 to v_{11}, represents a constant (laminar) transpiration strength from the leading edge forward to see if the flow can be kept laminar. The fourth and last block, v_{12} to v_{15}, indicates the effect of slot suction (suction region about 1% of the chord). Both position and suction amount are varied in this block.

Table 6.1: Case description

Airfoil Parameters	
Type	NACA 0012
Angle of Attack	6^o
Freestream Reynolds Number	$3 \cdot 10^6$
Freestream Mach Number	0.1
Number of Panels (each side/wake)	120/40

Remeshed	Yes
Finite Trailing Edge	Yes

Boundary Layer Parameters

Transition Prediction	Wazzan et al.
Eddy−Viscosity Correction	Kays−Moffat
Roughness Effects	No
Δh(0) for η−grid (upper/lower)	0.0005/0.005
Multiplier for η−grid (upper/lower)	1.16/1.14

Transpiration Distribution

Mass Transfer (upper/lower)	Yes/No

v_0:	$0.0 \leq \frac{x}{c} \leq 1.0$	$\frac{v_w}{u_\infty} = 0.0000$	$C_q = 0.0$
v_1:	$0.5 \leq \frac{x}{c} \leq 0.7$	$\frac{v_w}{u_\infty} = -0.002$	$C_q = 4.169 \cdot 10^{-4}$
v_2:	$0.5 \leq \frac{x}{c} \leq 0.7$	$\frac{v_w}{u_\infty} = -0.004$	$C_q = 8.338 \cdot 10^{-4}$
v_3:	$0.5 \leq \frac{x}{c} \leq 0.7$	$\frac{v_w}{u_\infty} = -0.006$	$C_q = 1.300 \cdot 10^{-3}$
v_4:	$0.2 \leq \frac{x}{c} \leq 0.4$	$\frac{v_w}{u_\infty} = -0.004$	$C_q = 8.664 \cdot 10^{-4}$
v_5:	$0.4 \leq \frac{x}{c} \leq 0.6$	$\frac{v_w}{u_\infty} = -0.004$	$C_q = 8.499 \cdot 10^{-4}$
v_6:	$0.6 \leq \frac{x}{c} \leq 0.8$	$\frac{v_w}{u_\infty} = -0.004$	$C_q = 8.270 \cdot 10^{-4}$
v_7:	$0.8 \leq \frac{x}{c} \leq 1.0$	$\frac{v_w}{u_\infty} = -0.004$	$C_q = 8.260 \cdot 10^{-4}$
v_8:	$0.0 \leq \frac{x}{c} \leq 0.1$	$\frac{v_w}{u_\infty} = -0.001$	$C_q = 1.129 \cdot 10^{-4}$
v_9:	$0.0 \leq \frac{x}{c} \leq 0.2$	$\frac{v_w}{u_\infty} = -0.001$	$C_q = 2.128 \cdot 10^{-4}$
v_{10}:	$0.0 \leq \frac{x}{c} \leq 0.3$	$\frac{v_w}{u_\infty} = -0.001$	$C_q = 3.112 \cdot 10^{-4}$
v_{11}:	$0.0 \leq \frac{x}{c} \leq 0.4$	$\frac{v_w}{u_\infty} = -0.001$	$C_q = 4.193 \cdot 10^{-4}$
v_{12}:	$0.60 \leq \frac{x}{c} \leq 0.61$	$\frac{v_w}{u_\infty} = -0.01$	$C_q = 2.464 \cdot 10^{-4}$
v_{13}:	$0.60 \leq \frac{x}{c} \leq 0.61$	$\frac{v_w}{u_\infty} = -0.02$	$C_q = 4.928 \cdot 10^{-4}$
v_{14}:	$0.80 \leq \frac{x}{c} \leq 0.81$	$\frac{v_w}{u_\infty} = -0.01$	$C_q = 2.043 \cdot 10^{-4}$
v_{15}:	$0.80 \leq \frac{x}{c} \leq 0.81$	$\frac{v_w}{u_\infty} = -0.02$	$C_q = 4.087 \cdot 10^{-4}$

6.1.2 Results

In this subsection, the results obtained with the previously mentioned transpiration distributions will be presented. It will show the effect on the displacement thickness, momentum thickness and skin friction coefficent in graphical content. It will also present the values of the lift coefficient, drag coefficient and transition location on the upper surface in table format. Next to these properties, the pressure coefficient distribution for the case without suction can be seen in figure 6.1. For a discussion of the results, one is referred to subsection 6.1.3.
Note that to create a NACA four-digit airfoil profile, several formulae are applied for the thickness distribution, leading edge radius and the mean camber line. These formulae and section definitions are found in several references and are explained concisely in appendix B.
In the figures, the $x-$axis represent the location along the chord from the leading edge forward. The transition locations in table 6.2 are along the boundary layer coordinates from the stagnation point forward.

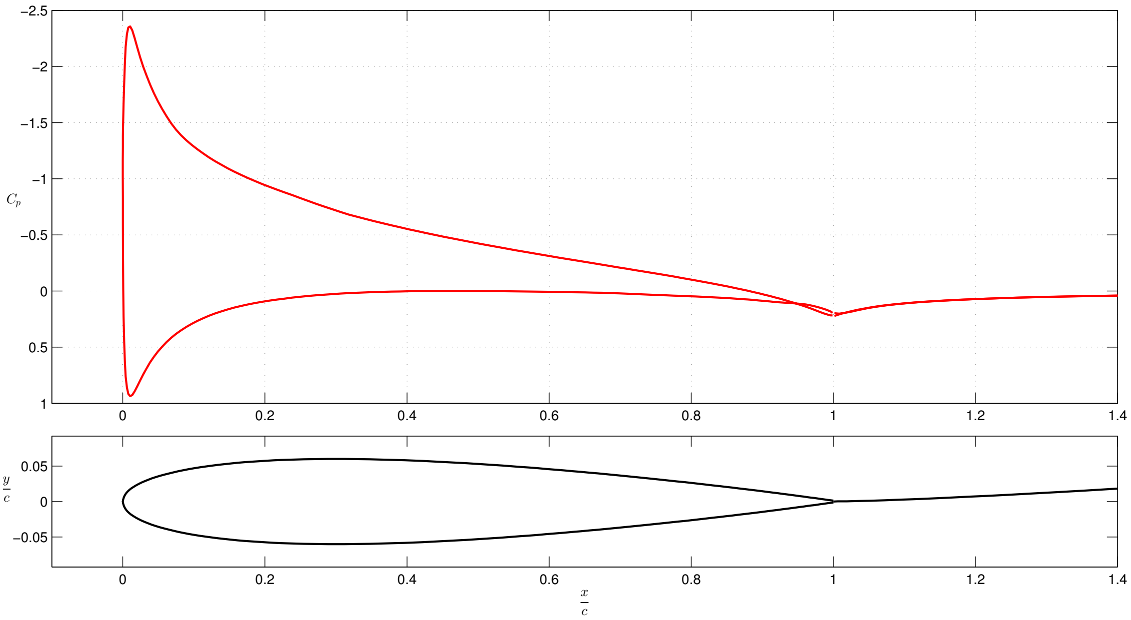

Figure 6.1: Pressure coefficient distribution and NACA 0012 geometry.

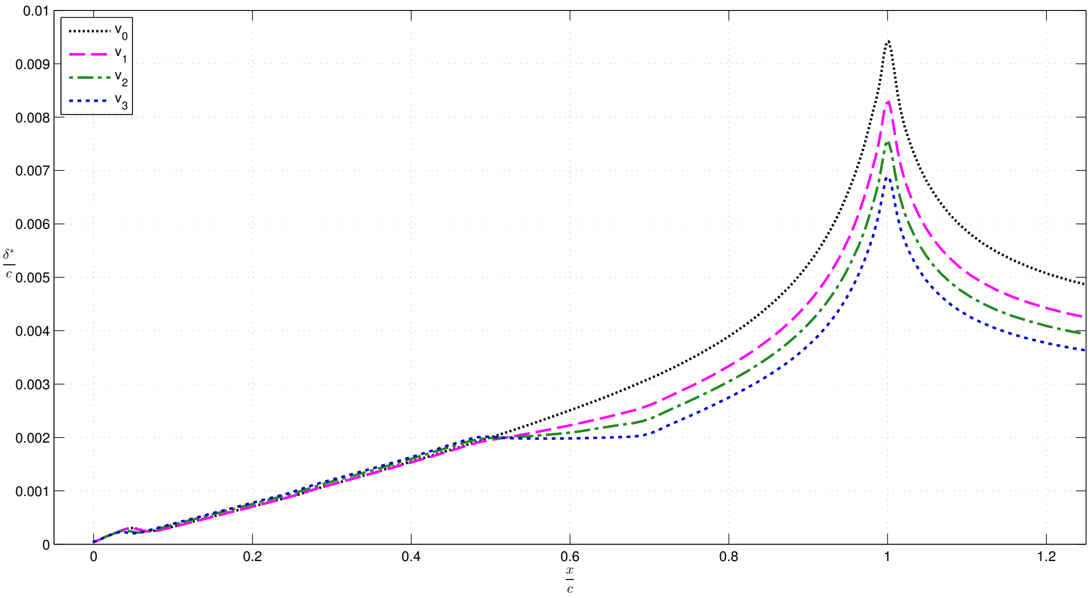

Figure 6.2: Displacement thickness. Constant region, increased turbulent suction block.

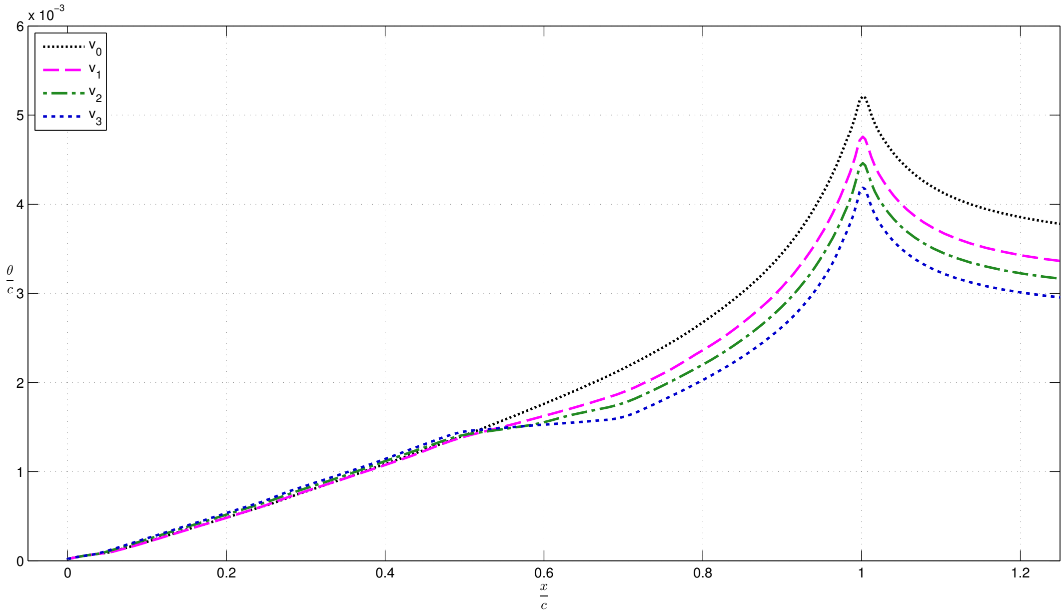

Figure 6.3: Momentum thickness. Constant region, increased turbulent suction block.

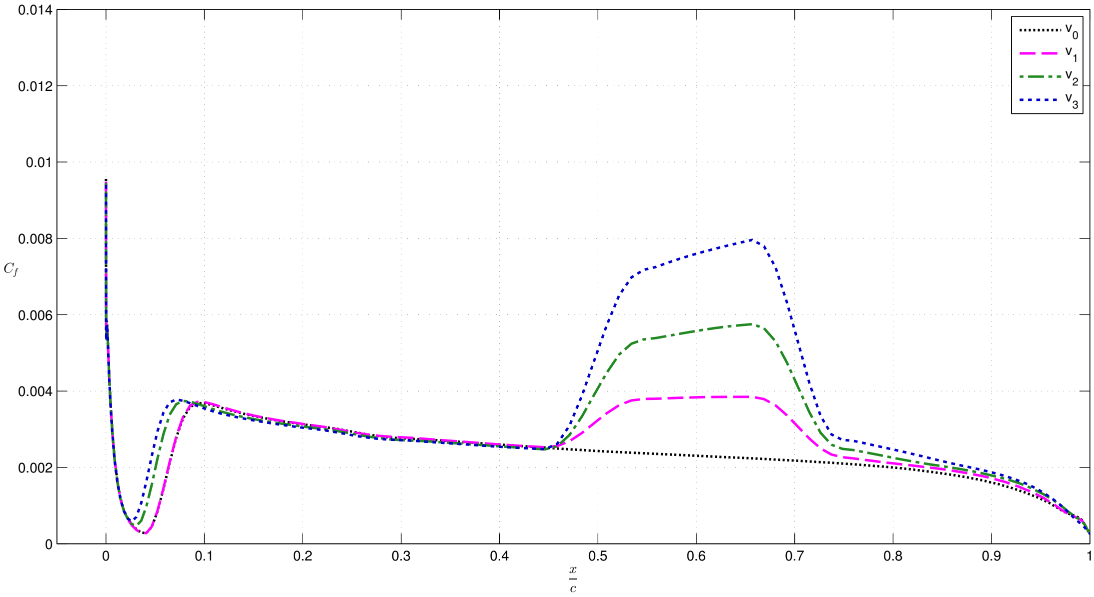

Figure 6.4: Skin friction coefficient. Constant region, increased turbulent suction block.

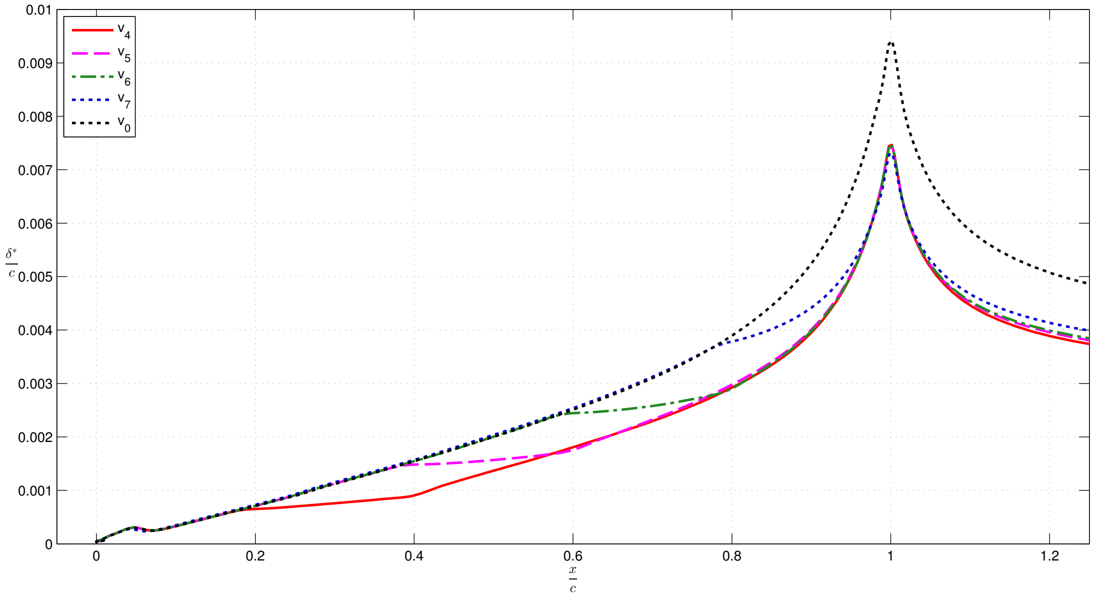

Figure 6.5: Displacement thickness. Varying region, constant turbulent suction block.

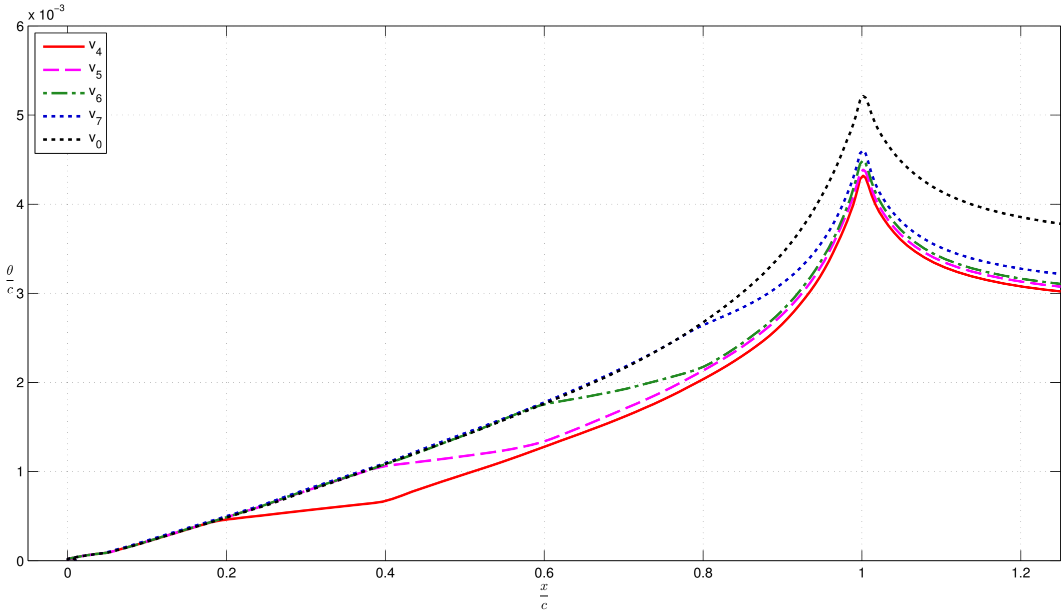

Figure 6.6: Momentum thickness. Varying region, constant turbulent suction block.

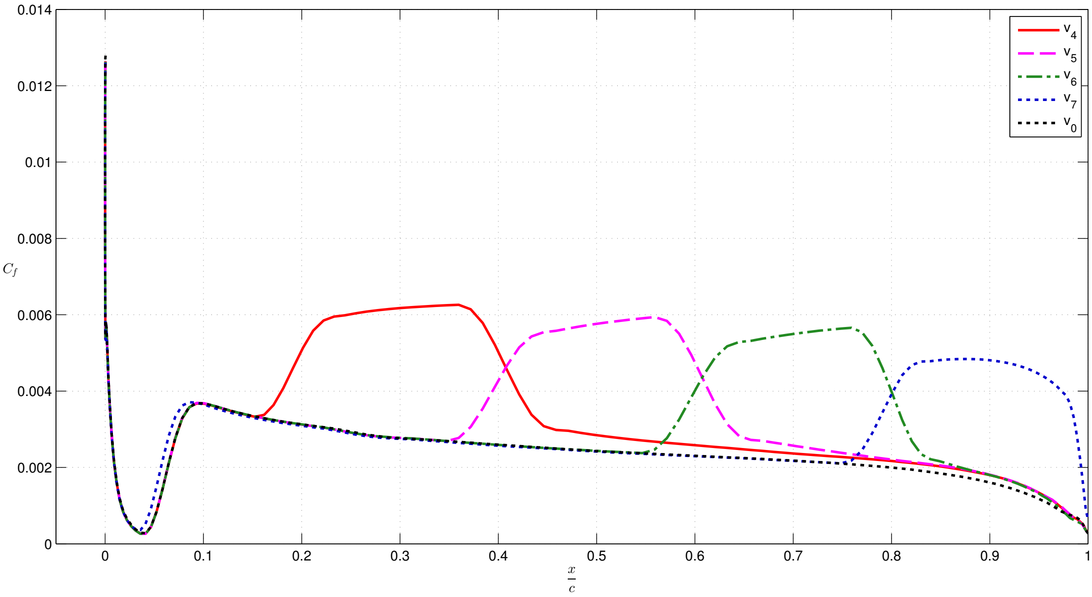

Figure 6.7: Skin friction coefficient. Varying region, constant turbulent suction block.

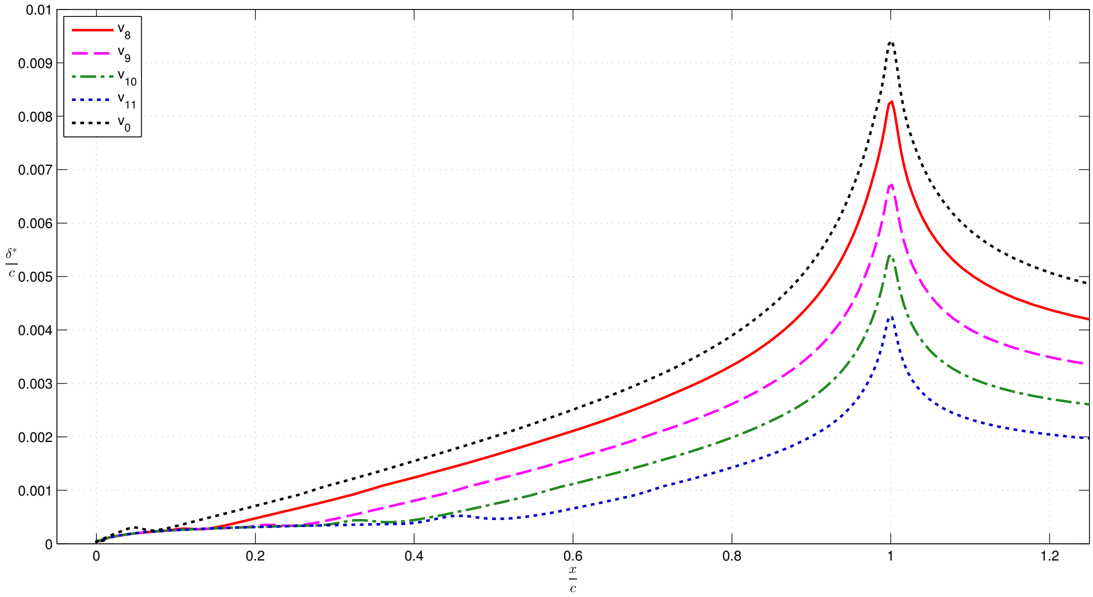

Figure 6.8: Displacement thickness. Varying region, constant laminar suction block.

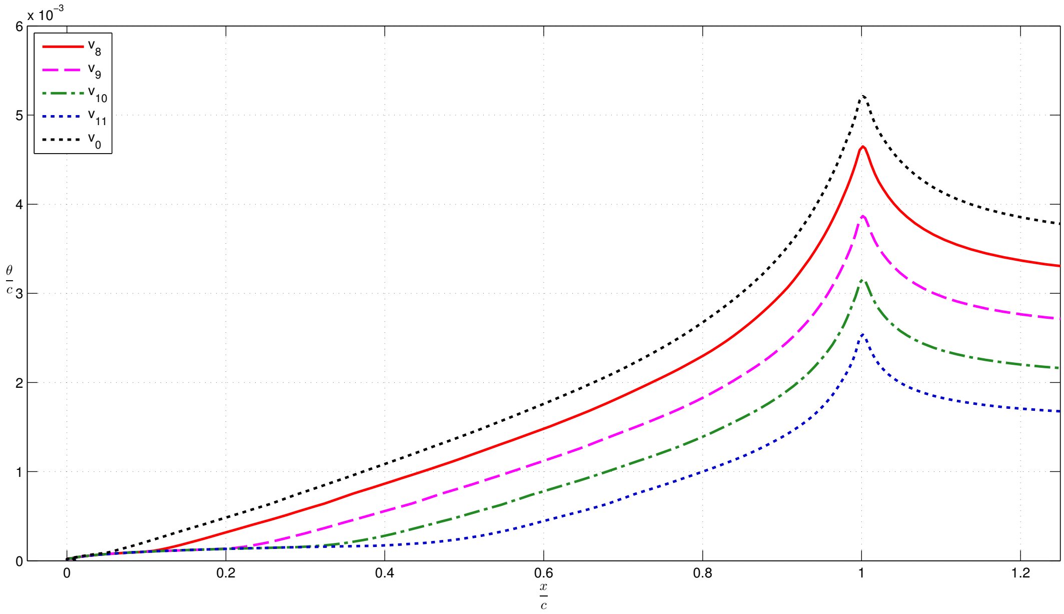

Figure 6.9: Momentum thickness. Varying region, constant laminar suction block.

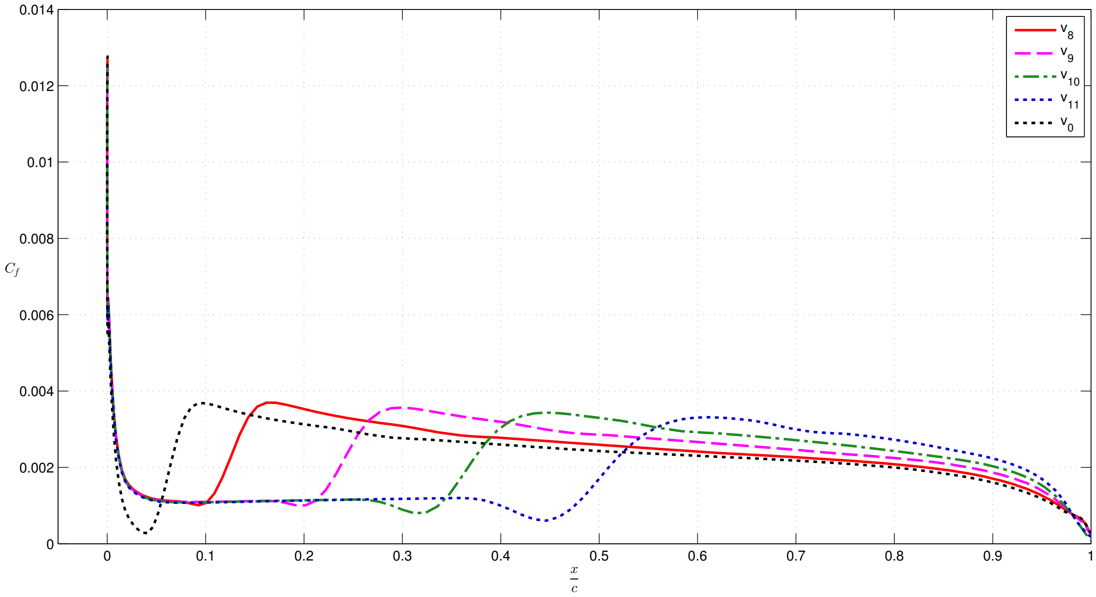

Figure 6.10: Skin friction coefficient. Varying region, constant laminar suction block.

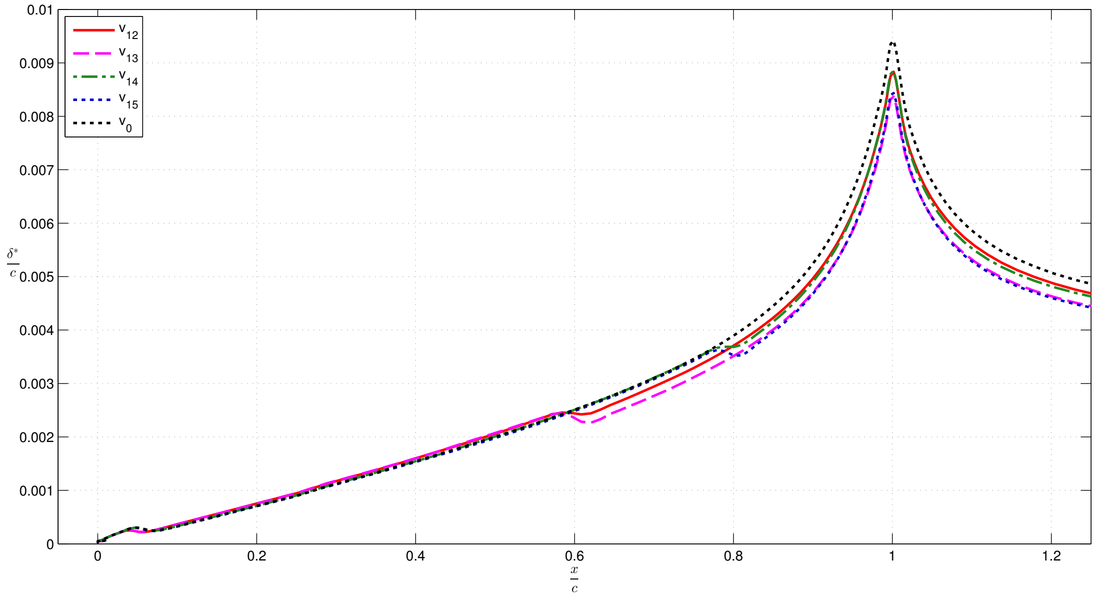

Figure 6.11: Displacement thickness. Slot suction block.

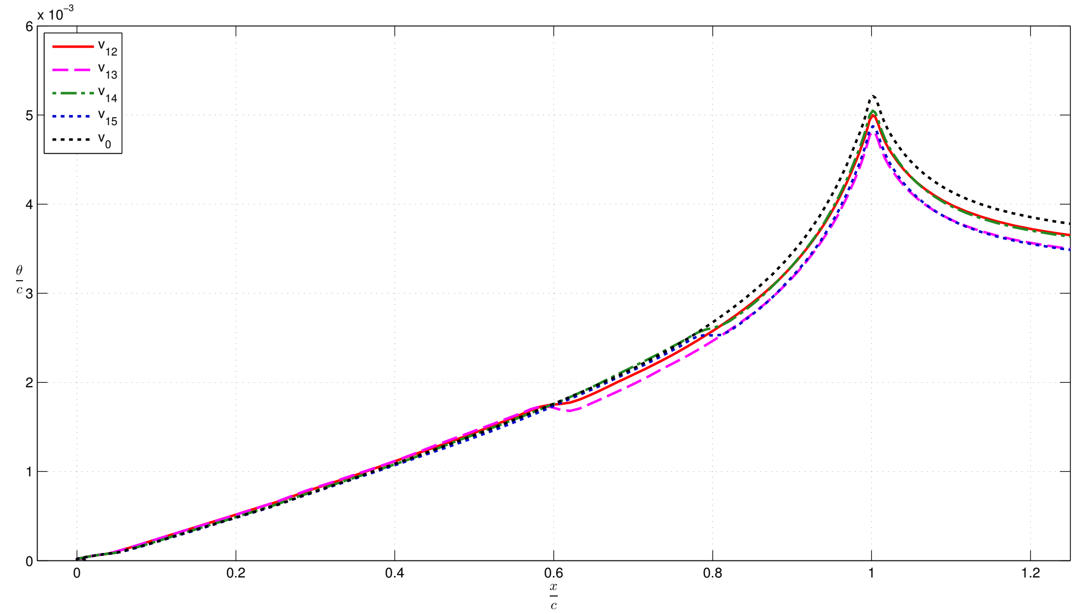

Figure 6.12: Momentum thickness. Slot suction block.

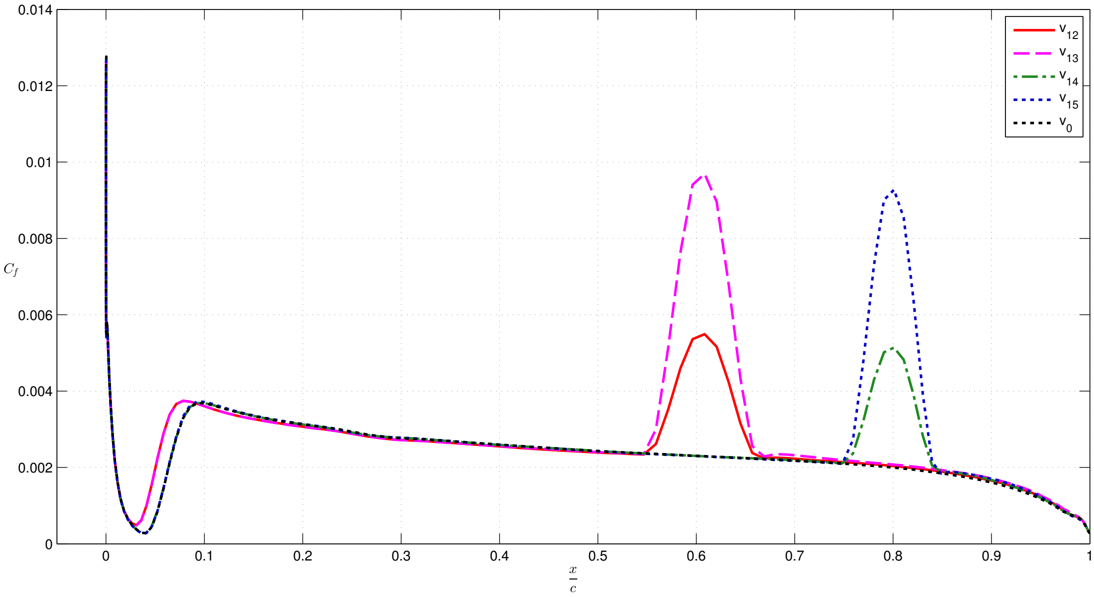

Figure 6.13: Skin friction coefficient. Slot suction block.

Table 6.2: Lift coefficient, drag coefficient and transition location for various transpiration distributions.

Transpiration Distribution	C_l	${C_d}^8$	Transition Location
v_0	0.6530	0.00845	0.0936
v_1	0.6626	0.00857	0.0938
v_2	0.6683	0.00894	0.0815
v_3	0.6748	0.00945	0.0758
v_4	0.6709	0.00880	0.0939
v_5	0.6687	0.00891	0.0939
v_6	0.6696	0.00892	0.0939
v_7	0.6726	0.00915	0.0876
v_8	0.6630	0.00783	0.1537
v_9	0.6775	0.00694	0.2595
v_{10}	0.6904	0.00616	0.3731
v_{11}	0.7029	0.00549	0.4964
v_{12}	0.6592	0.00864	0.0813
v_{13}	0.6633	0.00887	0.0814
v_{14}	0.6583	0.00862	0.0937
v_{15}	0.6629	0.00878	0.0938

6.1.3 Discussion

Since the transpiration distributions were divided in four main blocks, this subsection will discuss each block separately as well as some general comments.

Block I – constant region, increasing turbulent suction

For this block, the trend is quite clear. Increasing the suction amount will result in decreasing values for the displacement and momentum thickness after the starting point of suction. The values for the skin friction coefficient will increase significantly in the applied suction region. Note also that, after the applied suction region, the skin friction coefficient values will stay higher towards the trailing edge with increasing suction amount. These observations mainly result from the steeper velocity gradient near the wall when suction is increased. This will lead to higher skin friction coefficient values as well as 'more full' velocity profiles yielding lower displacement and momentum thicknesses.

As seen from table 6.2, the transition location will move slightly forward. The lift and drag coefficient are increasing with increased suction. For the latter one, an interesting observation can be made. Due to the decreasing value of the momentum thickness at the trailing edge, one would expect that the drag coefficient would decrease with respect to the case without suction. This is not the case since the sink drag (due to removal and stopping of the fluid) is increasing with increased suction. The net effect will cause a larger value for the drag coefficient.

---

[8] Wake drag plus sink drag.

Block II – varying region, constant turbulent suction

From this block, the effect of varying the transpiration position in the turbulent region can be seen. For the skin friction coefficient, a clear increase can be seen in regions where suction is applied.
The transition location will, as in block I and as expected, not be influenced much by changing the transpiration position in the turbulent region. Varying the position of the (same) transpiration distribution will nearly keep the lift coefficient constant but higher than for the case without transpiration. Moving the suction distribution backwards, the drag coefficient will increase. This time, the sink drag will not cause this since it is nearly the same for each transpiration distribution in this block. The reason for it is the increasing trailing edge momentum thickness when moving the suction distribution backwards (see figure 6.6). It is also interesting to see that the maximum value for the displacement thickness is nearly the same for these suction distributions (see figure 6.5).

Block III – varying region, constant laminar suction

The effect of the third block's transpiration distributions is probably the most remarkable. The first observation is that when applying (enough) suction from the leading edge forward, the flow can be kept laminar and transition can be delayed significantly. The velocity gradient near the wall of laminar boundary layers is smaller than for turbulent boundary layers and hence the values for the skin friction coefficient are lower when laminar flow is present. Notice that in regions where transpiration has ended, the value for the skin friction coefficient is larger for cases with longer suction distributions. Notice that increasing the suction length will cause the displacement and momentum thicknesses to decrease significantly. Observe also that even though the sink drag is increasing with increased suction length, the drag coefficient is decreasing rapidly. This once again follows from the decreased momentum thickness at the trailing edge and the fact that the suction quantities (and hence the sink drag term) are significantly lower than for turbulent cases. The value of the lift coefficient is increasing with increased suction length. This is due to the decrease in displacement and boundary layer thicknesses, resulting in less viscous effects and moving towards a 'more inviscid' case.

Block IV – slot suction, varying position and amount, turbulent region

The fourth block's transpiration distributions has been added to investigate the effect of slot suction on the boundary layer and airfoil properties. The reason one might use slot suction is for easier manufacturing and less disturbance of the surface flow (note that it is hard to predict the effect of the presence of the suction device on the flow structure).
An immediate observation is that the amount of suction has to be larger to have a significant effect on the properties as compared with previous blocks. On the other hand, the suction coefficient and hence the volume that has been sucked away has the same order of magnitude as the other distributions. Note that for about the same suction coefficient, it is more effective (with respect to airfoil properties) to distribute suction than to squeeze it in a small area. Between each distribution in this block, the difference between the displacement and momentum thicknesses is marginal. Note that there is a significant difference with the case without suction. The same holds for the skin friction. Typical trends can be seen in the applied suction region but the difference between each distribution after this region is marginal.

From table 6.2 it can be seen that the lift and drag coefficient are increasing for increased suction, albeit a small increment.

General

Based on previous discussion, the transpiration distribution is dependent on the goal that is pursued. For example, if one desires a high lift-over-drag coefficient, keeping the flow laminar (block III) would be the main goal (since the lift coefficient increases and the drag coefficient reduces). If one tries to avoid turbulent separation at the trailing edge without much care for the drag coefficient, one should aim for a transpiration distribution that keeps the flow attached to the body (letting the skin friction coefficient stay larger than zero). Note that this requires much larger suction values than for laminar suction. On the other hand, if one would like to let the airfoil stall, blowing along the surface could be applied (getting rid of the lift). Of course, chosing a certain transpiration distribution is heavily dependent on practical limitations. As an example, transpiration distribution v_7 would be hard to apply since a suction device should be installed up till the trailing edge (which is usually very thin). For ease of manufacturing one could use slot suction although significant larger amounts of suction are necessary.

Considering the case without suction $-$ v_0 $-$ it can be observed that the lift coefficient is predicted well as compared with the experimental results of Abbott and von Doenhoff [1959]. The experimental value is 0.63 (read off from graph). The same holds for the drag coefficient, which is 0.0084 in Abbott and von Doenhoff [1959]. Note that XFOIL predicts the lift coefficient a bit higher, 0.6603, and the drag coefficient significant lower, 0.00753. Important to point out is that the worst case scenario for the sink drag has been taken into account. This means that no reinjection of the transpired flow takes place. It is possible to reduce this sink drag by reinjection but an accurate determination is hard and still up for debate.

6.1.4 Convergence and wake velocity profiles

To see the effect of the distribution of the panels along the surface, it is useful to see how the lift coefficient changes each interaction cycle. In figure 6.14, the lift coefficient history can be seen. One for uniformly distributed panels and one with half cosine distributed panels. The latter one will increase the panel number in the regions where the most severe changes occur (see appendix B). It can be seen that increasing the number of panels in these regions will lead to an increase in lift coefficient and less fluctuation after several cycles. As can be seen, enough interaction cycles should be specified to ensure convergence.

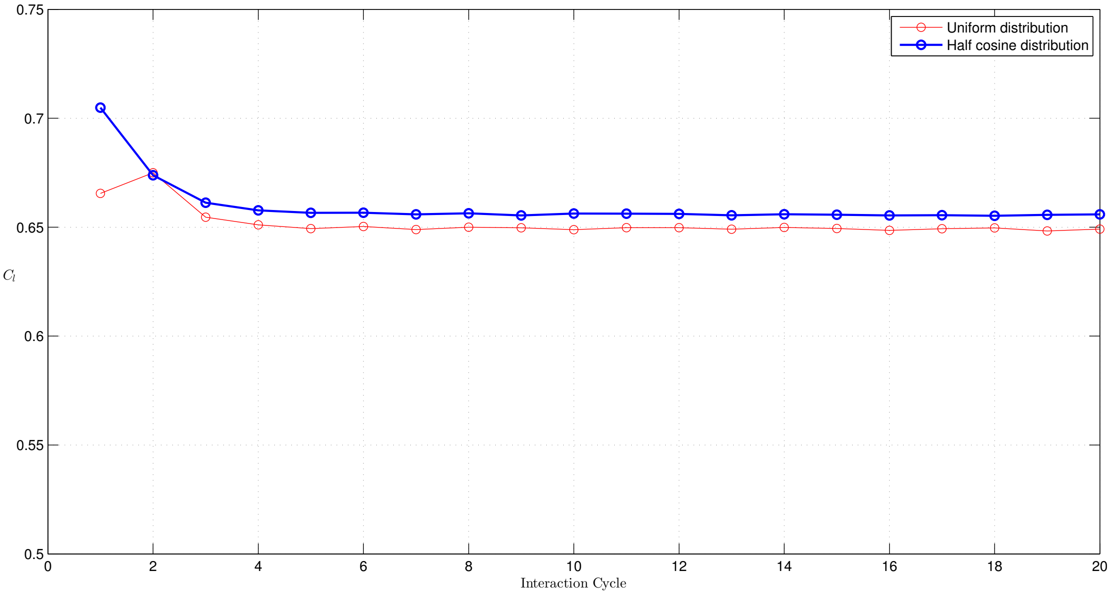

Figure 6.14: Convergence history. $R_e = 3 \cdot 10^6$, $\alpha = 6^o$, 240 panels (total).

To see the distribution of the velocity profiles in the wake, figure 6.15 is attached. As can be seen in the caption, this is a NACA 0012 profile under an angle of attack of zero degrees. As expected, fine symmetry is observed of the boundary layers on the upper and lower side of the wake streamline. About three chords downstream, the maximum deviation with the freestream (at the streamline location) is about 6%.

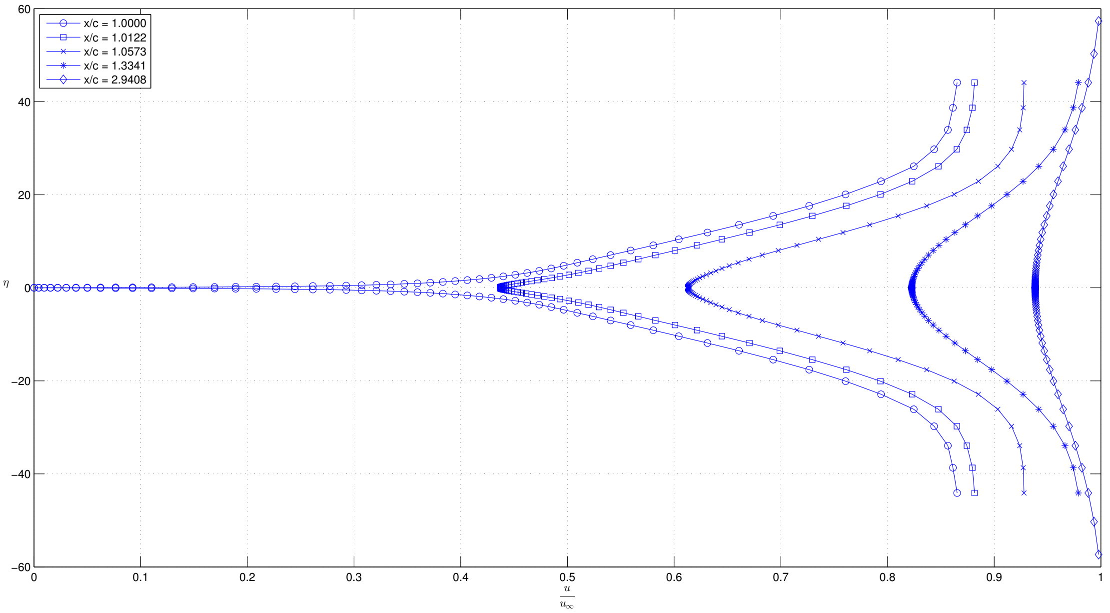

Figure 6.15: Wake velocity profiles. $R_e = 3 \cdot 10^6$, $\alpha = 0^o$, 200 panels (total).

6.2 Test case: NACA 4418

For the first test case, a NACA 4418 profile has been chosen. This is a relatively thick and cambered profile that could be used in wind turbine blades where surface mass transfer can have beneficial effects.

This profile will be used to compare the boundary layer calculation with surface mass transfer between ACTITRANS2D, RFOILSUC and RFOILSUCV2. It will present the boundary layer parameters as well as an indication of what happens to the pressure coefficient distribution when suction is applied. By using the formulae for the geometry of a NACA four-digit series, the body is created in ACTITRANS2D (see appendix B). Important to point out is that this is not exactly the same geometry as created by XFOIL (and hence RFOILSUC and RFOILSUCV2). By specifying a NACA 4418 profile and closing the trailing edge gap via the geometry design routine will yield a slightly different profile. This observation should not matter in our analysis since the same coordinate files are used between the programs (generated with ACTITRANS2D).

6.2.1 Case description

The settings for ACTITRANS2D for this specific case can be found in table 6.3. For the boundary layer properties and the pressure coefficient distribution, the angle of attack is set at 8^o.

Table 6.3: Case description

Airfoil Parameters		
Type	NACA 4418	
Angle of Attack	8^o	
Freestream Reynolds Number	$6 \cdot 10^6$	
Freestream Mach Number	0.1	
Number of Panels (each side/wake)	120/40	
Remeshed	Yes	
Finite Trailing Edge	No	
Boundary Layer Parameters		
Transition Prediction	Michel	
Eddy−Viscosity Correction	Cebeci	
Roughness Effects	No	
Δh(0) for η−grid (upper/lower)	0.0005/0.005	
Multiplier for η−grid (upper/lower)	1.16/1.14	
Transpiration Distribution		
Mass Transfer (upper/lower)	Yes/No	
$0.5 \leq \frac{x}{c} \leq 0.7$	$\frac{v_w}{u_\infty} = -0.002$	$C_q = 4.370 \cdot 10^{-4}$

6.2.2 Boundary layer characteristics

This section will present the results for the most common boundary layer characteristics. Note that in ACTITRANS2D – as opposed to RFOILSUC and RFOILSUCV2 – the wake properties are included. The reason for this is that the versions of RFOIL are based on an older version of XFOIL where this functionality was not yet included.

Displacement thickness, momentum thickness and shape factor

From the resulting velocity profiles, the values for the displacement and momentum thickness (and hence the shape factor) can be computed. These velocity profiles – as computed by ACTITRANS2D – can be seen in figure 6.16. The three boundary layer parameters are illustrated in figures 6.17, 6.18 and 6.19.

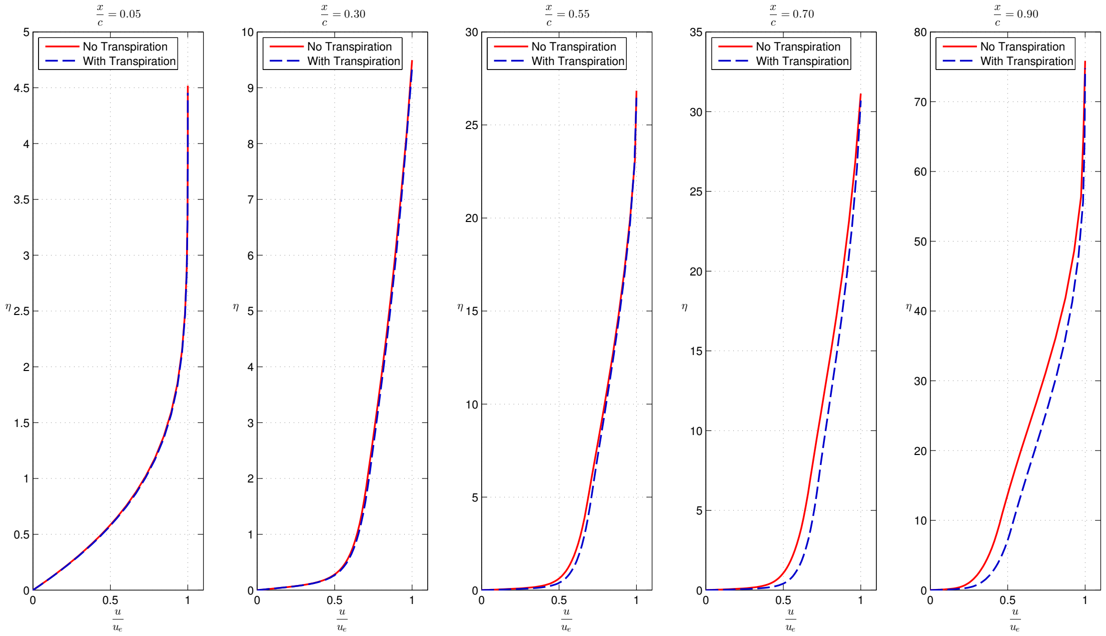

Figure 6.16: Boundary layer velocity profiles at several locations on the upper surface.

The locations to plot the boundary layer velocity profiles in figure 6.16 are chosen in such a way that the most important aspects are captured. This includes laminar boundary layer flow, turbulent boundary layer flow before suction, boundary layer flow in the suction region and the profile near the trailing edge. As can be seen, the profiles are nearly the same at the stations before the applied suction region. Inside this region, the velocity gradient at the wall will be larger and more 'full' profiles will result. At the last station, the boundary layer becomes unstable and is about to separate. This is counteracted by the applied suction.

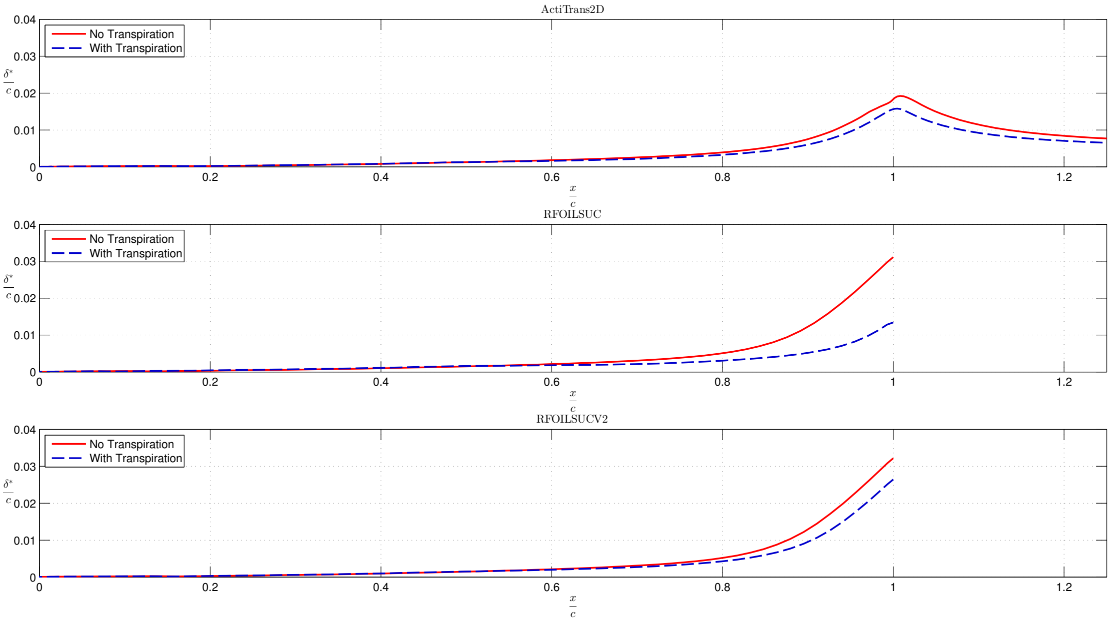

Figure 6.17: Displacement thickness comparison upper surface.

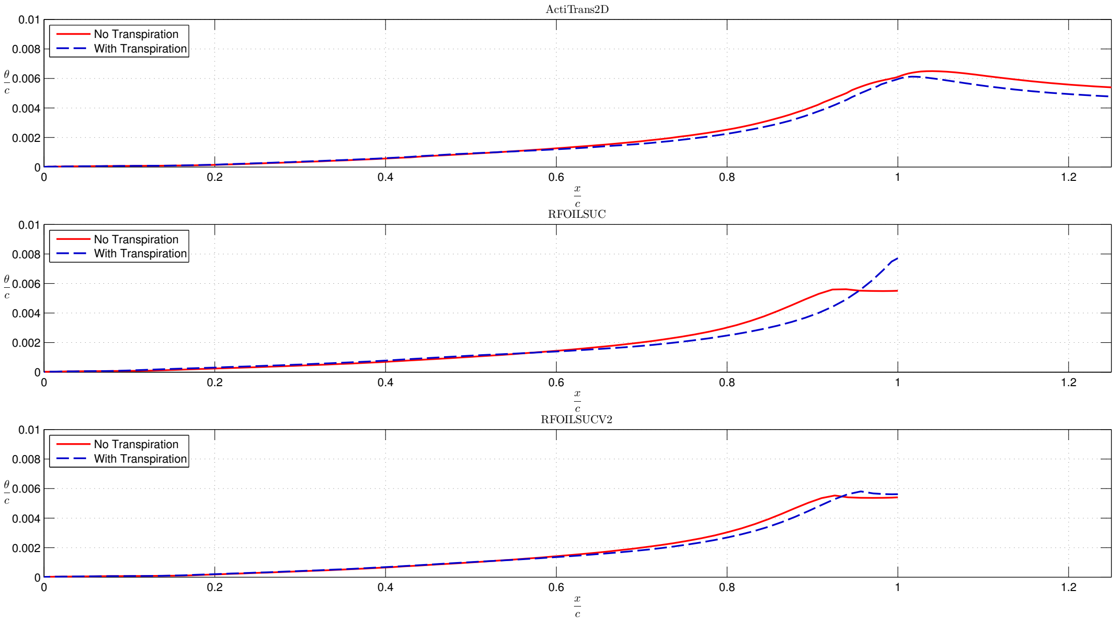

Figure 6.18: Momentum thickness comparison upper surface.

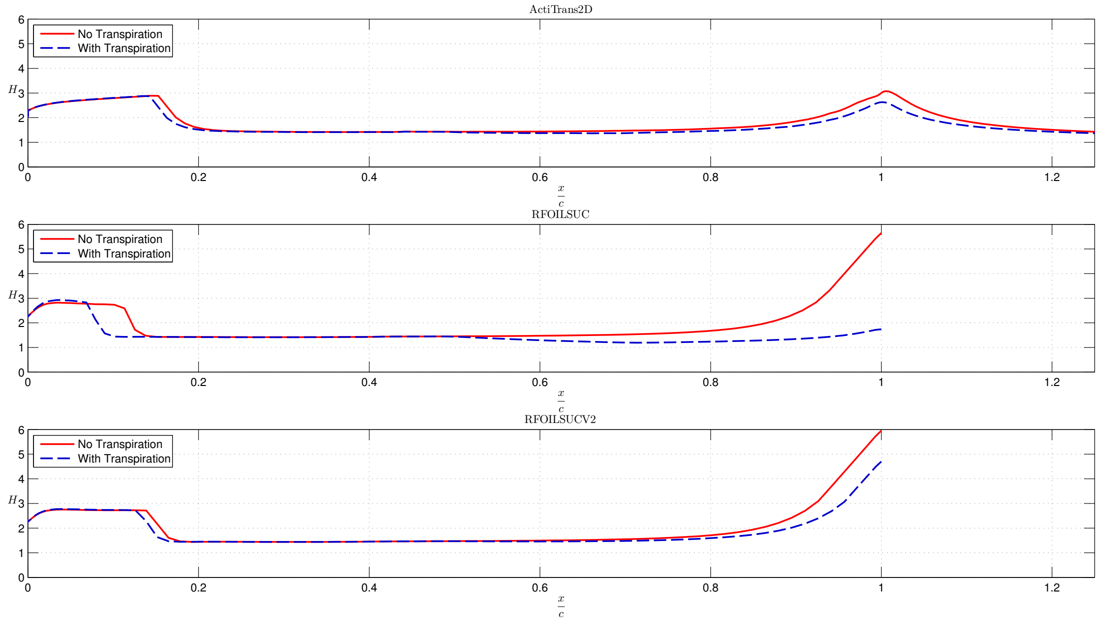

Figure 6.19: Shape factor comparison upper surface.

From figures 6.17 till 6.19, it can be seen that – as expected from the formulae – the displacement and momentum thickness are decreasing when suction is applied. Note that the effect of suction is predicted (too) large in RFOILSUC. This can be best seen in figure 6.19, where the shape factor drops heavily for this small amount of suction. From this plot, transition can also be observed. Note that RFOILSUC predicts transition a bit earlier than ACTITRANS2D and RFOILSUCV2. In general, the effect of suction is overpredicted in RFOILSUC and comparable between ACTITRANS2D and RFOILSUCV2.

Skin friction coefficient

In ACTITRANS2D, the skin friction coefficient has been determined based on the velocity gradient at the wall. In RFOILSUC and RFOILSUCV2, empirical relations were used based on the shape factor and momentum thickness Reynolds number. A comparison can be found in figure 6.20.

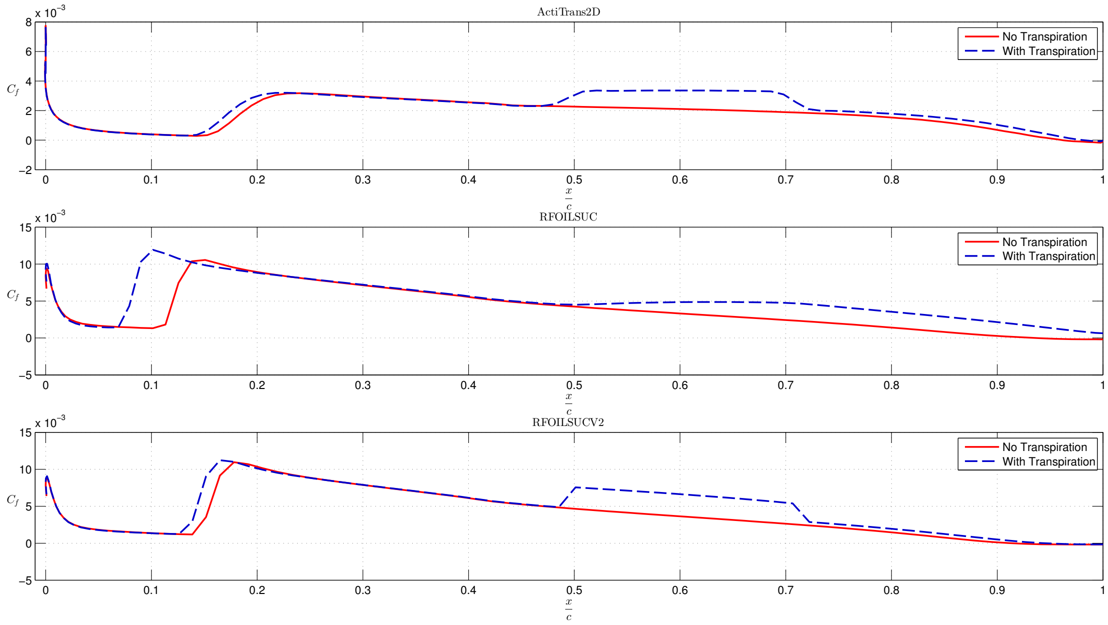

Figure 6.20: Skin friction coefficient comparison upper surface.

First of all, with the presence of boundary layer suction, separation (the location where C_f drops below zero) at the trailing edge is delayed in each case. Note that in RFOILSUC, separation is even completely removed.

It can easily be imagined that, when the suction regions ends, the velocity gradient near the wall should 'bounce' back to a lower value. This trend can be seen in ACTITRANS2D and RFOILSUCV2 but not in RFOILSUC. This is another indication that indeed the empirical closure relation for the skin friction coefficient with mass transfer is erroneous in RFOILSUC. From the plot it can once again be seen that transition is occurring as a sharp, continuous front in the RFOILSUC versions and smooth in ACTITRANS2D. Not only the way in which transition occurs is different, the 'jump' in skin friction coefficient is significantly higher. This smooth transition is modeled in ACTITRANS2D by using a smooth intermittency factor – γ_{tr} – which is zero for laminar flow and one for turbulent flow. This empirical formula can be found in section 3.5.

Also observe that – when suction is applied – the transition location will move forward. This will be explained by means of the pressure coefficient distribution in the next section.

6.2.3 Pressure coefficient distribution

In this subsection, the pressure coefficient distribution is plotted for the case with and without the specified mass transfer distribution as computed by ACTITRANS2D. The pressure coefficient distribution is one of the most important properties for an airfoil. From this distribution, other parameters may be derived.

The computed pressure coefficient distribution can be seen in figure 6.21. For convenience, the inviscid pressure coefficient distribution is also plotted. Observe that the overall effect of this transpiration distribution is that the pressure coefficient distribution moves towards a 'more inviscid' distribution leading to a larger integrated area and hence a higher lift coefficient. This is a direct effect of the reduced displacement thickness (remember the transpiration

model in the panel method to introduce viscous effects) due to the 'fuller' boundary layer velocity profiles.
Note also that the leading edge pressure peak will be higher. This will result in a transition location that moves slightly forward (if possible and not already at the leading edge).

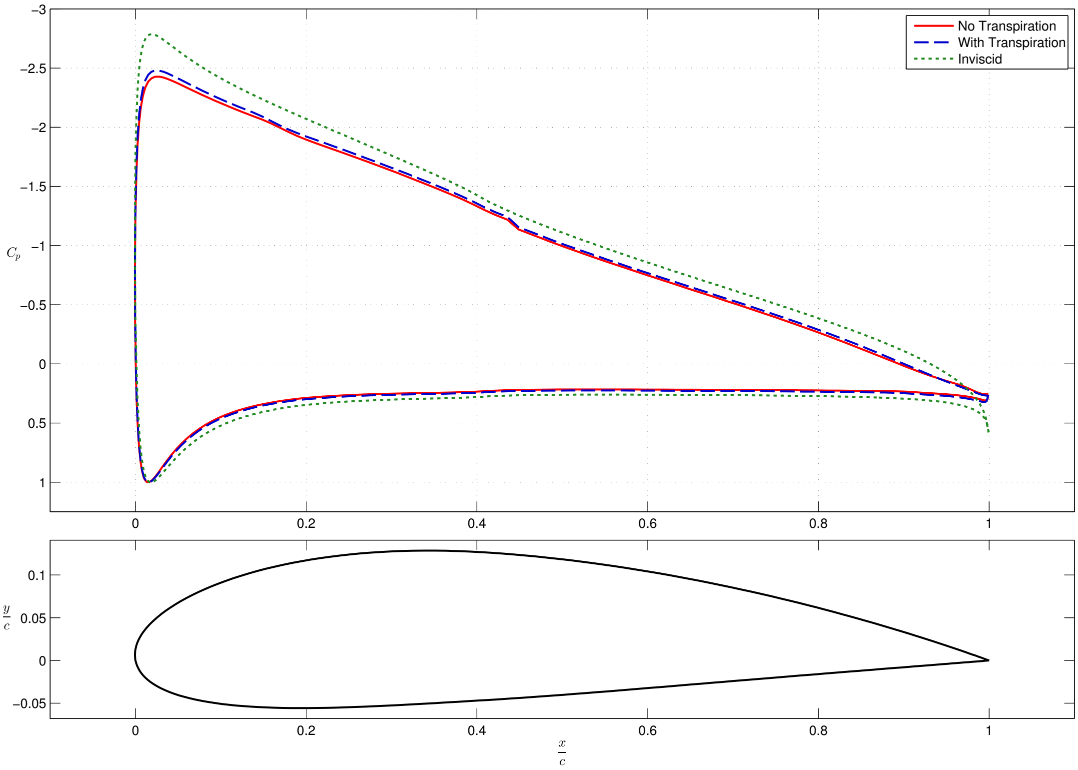

Figure 6.21: Pressure coefficient comparison.

Due to lack of measurement data of the NACA 4418 profile with and without mass transfer (with zero trailing edge thickness), no credible comparison can be made between the computational methods. By using measurement data of the AF 0901 profile developed by Actiflow B.V., the most credible methods – ACTITRANS2D and RFOILSUCV2 – will be compared in the next section.

6.2.4 Convergence

For this profile, the same way of convergence can be observed as for the NACA 0012 profile. With a more dense distribution of panels in the leading and trailing edge regions (see appendix B), the sudden changes are better captured and a higher lift coefficient will result.

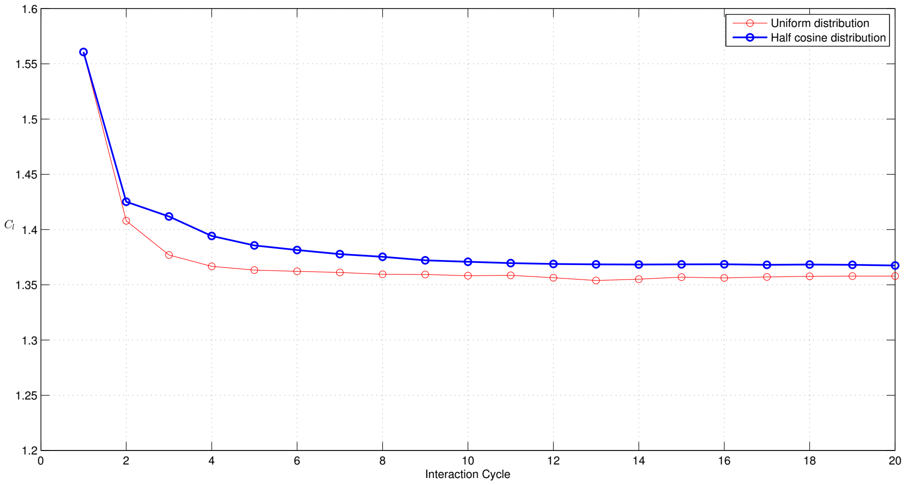

Figure 6.22: Convergence history. $R_e = 6 \cdot 10^6$, $\alpha = 8^o$, 240 panels (total).

6.3 Test case: AF 0901

In the past, Actiflow B.V. performed wind tunnel measurements[9] on an airfoil with certain mass transfer distributions. This airfoil is the AF 0901 profile described in Zwang [2009]. The measurements were mainly performed to verify the simulations done on this profile with design tools based on boundary layer calculations with integral methods (extended with mass transfer terms). The results and description of the measurements can be found in Bink [2010]. Since measurement data on airfoils with a certain suction distribution is scarce, this provides a valuable way of comparing ACTITRANS2D with the real world. Besides this, it will be compared with RFOILSUCV2 to see the differences between the design tools.
A three-dimensional view of the profile can be found in figure 6.23.

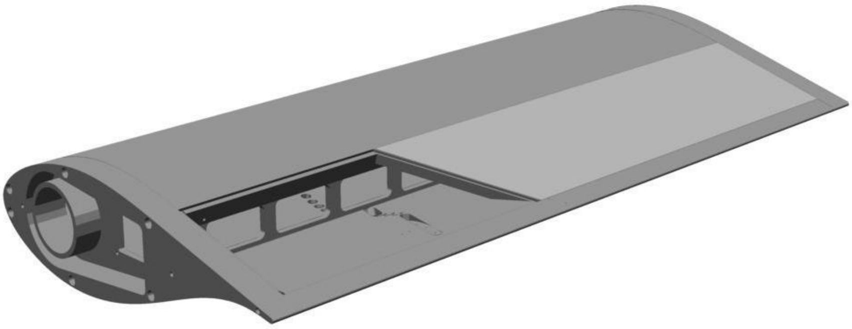

Figure 6.23: Three dimensional view AF 0901. From Bink [2010].

The case description that was used to determine the airfoil properties is found in subsection 6.3.1. The actual comparison with the measurement data and RFOILSUCV2 can be seen in subsection 6.3.2. Subsection 6.3.3 will contain a comparison of the boundary layer parameters determined by ACTITRANS2D and RFOILSUCV2 as well as the pressure coefficient distribution determined by ACTITRANS2D.

6.3.1 Case description

The settings for ACTITRANS2D for this profile can be seen in table 6.4. This time, a coordinate file is read in instead of creating a NACA profile. Notice again that a finite trailing edge is present and three suction distributions were applied at 60% to 82% of the chord.

---

[9] Low speed, low turbulence wind tunnel of the faculty of aerospace engineering of the Delft University of Technology in 2009.

Table 6.4: Case description

Airfoil Parameters		
Type	AF 0901	
Angle of Attack	-2^o to 14^o	
Freestream Reynolds Number	$3 \cdot 10^6$	
Freestream Mach Number	0.2	
Coordinate file read in	Yes	
Wake panels	40	
Remeshed	No	
Finite Trailing Edge	Yes	
Boundary Layer Parameters		
Transition Prediction	Wazzan et al.	
Eddy$-$Viscosity Correction	Kays$-$Moffat	
Roughness Effects	No	
Δh(0) for $\eta-$grid (upper/lower)	0.0005/0.005	
Multiplier for $\eta-$grid (upper/lower)	1.16/1.14	
Transpiration Distribution		
Mass Transfer (upper/lower)	Yes/No	
$0.60 \leq \frac{x}{c} \leq 0.82$	$\frac{v_w}{u_\infty} = -0.002$	$C_q = 4.695 \cdot 10^{-4}$
$0.60 \leq \frac{x}{c} \leq 0.82$	$\frac{v_w}{u_\infty} = -0.004$	$C_q = 9.390 \cdot 10^{-4}$
$0.60 \leq \frac{x}{c} \leq 0.82$	$\frac{v_w}{u_\infty} = -0.006$	$C_q = 1.401 \cdot 10^{-3}$

6.3.2 Airfoil properties

In this subsection, several airfoil properties are presented in figures 6.24 to 6.27. It covers a comparison between ACTITRANS2D, RFOILSUCV2 and experimental data. Below each of the figures, a concise discussion is devoted to the observations that are made. Notice that the clean airfoil is considered as well as the airfoil with transition fixed on the top surface at five per cent of the chord (using a zig-zag strip).

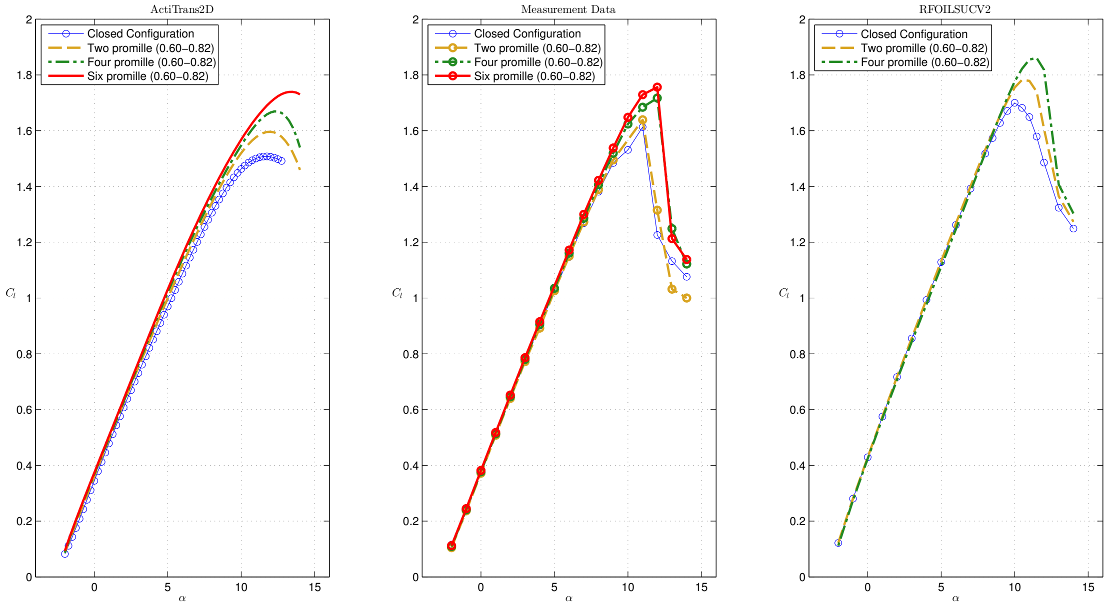

Figure 6.24: Lift coefficient curve AF 0901 — Clean configuration.

Assessing the lift coefficient curve in figure 6.24, several important aspects can be captured. First of all, observe from each subplot that the maximum lift coefficient is increased with increased suction. Also the angle of attack where the profile stalls is increased slightly. Notice that the correspondence between the measurements and ACTITRANS2D is very good up till massive separated flow (stall). In the third subplot of RFOILSUCV2 the overprediction can clearly be seen for the two and four promille suction cases. The six promille suction case could not be simulated since it gave numerical errors (this will be the case for each plot in the clean configuration).

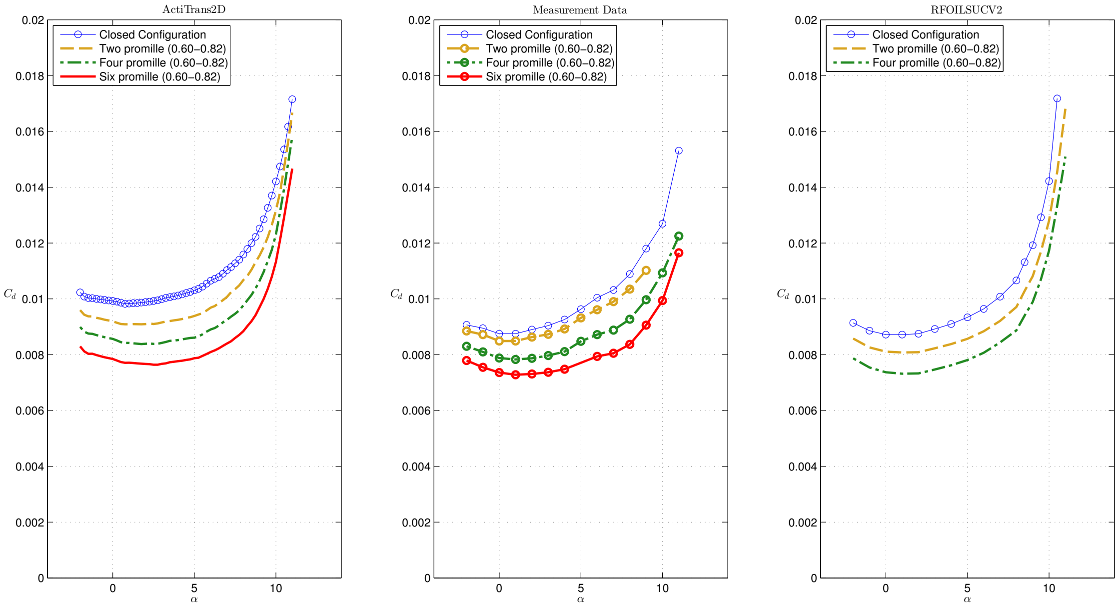

Figure 6.25: Drag coefficient curve AF 0901 — Clean configuration.

In figure 6.25, the drag coefficient curve is shown for each case. Some words are necessary here to describe the meaning of this drag coefficient. In the experiments, the wake velocity profile is determined via a wake rake. From this velocity distribution, the wake or profile drag is determined. This time, the sink drag should not be included since this is a separate drag and was not measured in the experiments (see Terry [2004]). In reality, the drag coefficient is higher and the lift over drag ratio lower.
As may be seen, ACTITRANS2D is predicting the drag coefficient slightly higher than the measurements and RFOILSUCV2 a bit lower. Each time the suction distribution is increased, a jump can be seen in the drag coefficient.

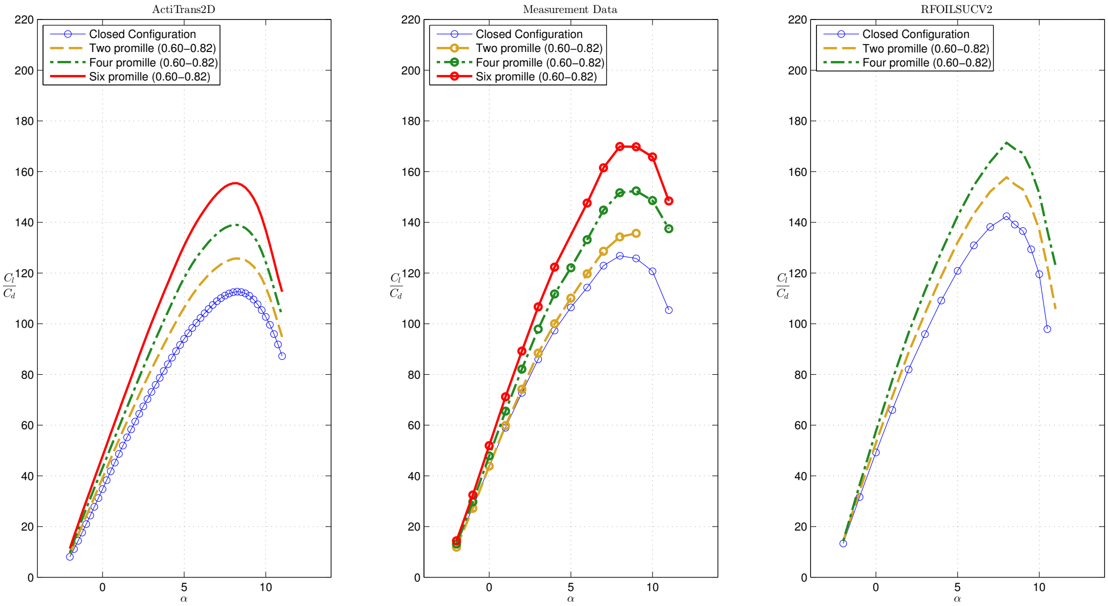

Figure 6.26: Lift-drag polar AF 0901 — Clean configuration.

From the previously mentioned parameters, the lift over drag ratio can be determined and is plotted in figure 6.26. Note that in each simulation, the angle of attack where the maximum lift over drag is obtained is predicted well (about eight degrees). Also note that ACTITRANS2D underpredicts the maximum lift over drag ratio and RFOILSUCV2 overpredicts this.
Comparing the increase in maximum lift over drag ratio for the case without suction and the case with four promille suction, it can be determined that the maximum is increased 23.4% in ACTITRANS2D, 20.1% in the experiments and 20.3% in RFOILSUCV2. This shows that although the absolute values are a bit off, the relative values are predicted well.

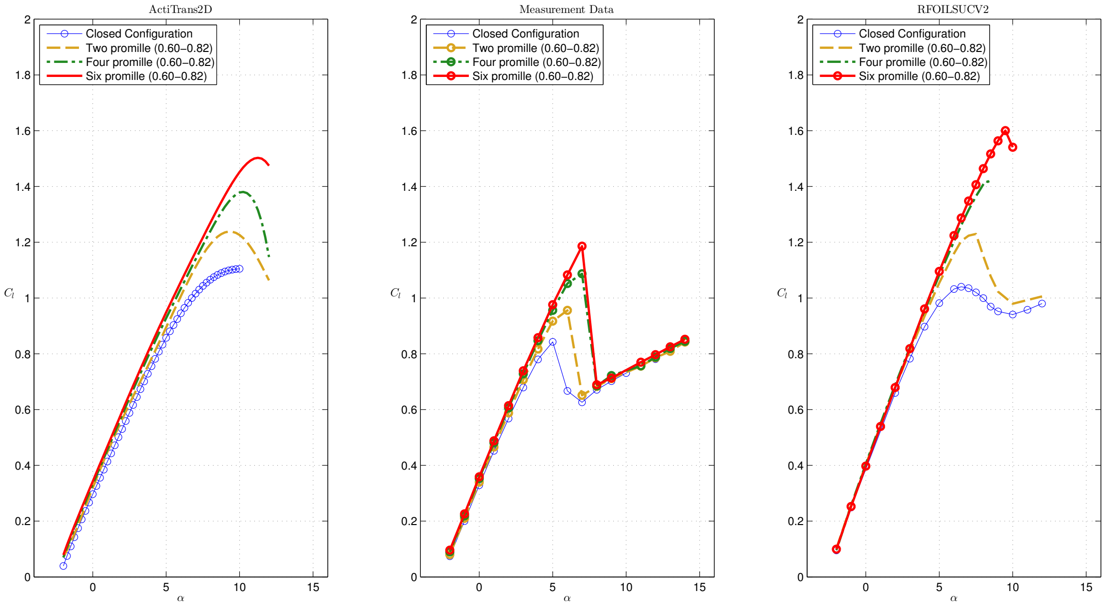

Figure 6.27: Lift coefficient curve AF 0901 — fixed transition upper side.

As a last comparison with experimental data, the case where the transition point was fixed at five per cent of the chord on the upper side is considered. To simulate this condition, zigzag tape of 0.21 millimeter was used (see Bink [2010]). It is known this does not simulate the soiling of the wind turbine blade well but it can be used to set transition at a certain location. The zigzag tape was applied at five per cent of the chord at the upper side. To simulate this in the design tools, transition has been set to this specific location on the upper surface.
At first sight, simulations and measurements do not agree well. However, taking a closer look to the situation will clarify things. In reality, stall will occur a lot earlier (at smaller angle of attack) than in simulations (the exact reason for this is not clear, could originate both from experiment or from simulation). Up to the point of stall, the agreement with ACTITRANS2D is good and with RFOILSUCV2 worse. A good way to see this is to look at the subplots at an angle of attack of five degrees.
Another aspect that can be seen from these plots is that the maximum lift coefficient is increased more for the applied suction quantities as compared to the clean configuration.

6.3.3 Boundary layer properties

To see the effect on the velocity profiles and boundary layer properties, figures 6.28 till 6.31 are included. An angle of attack of eight degrees was set as well as free transition. The same observations can be made as before when applying suction in a certain region. The velocity profiles will be more full and the gradient will be larger near the wall, the shape factor will decrease and the transition point will slightly move forward. Also the pressure coefficient distribution will change such that the lift coefficient value will increase.

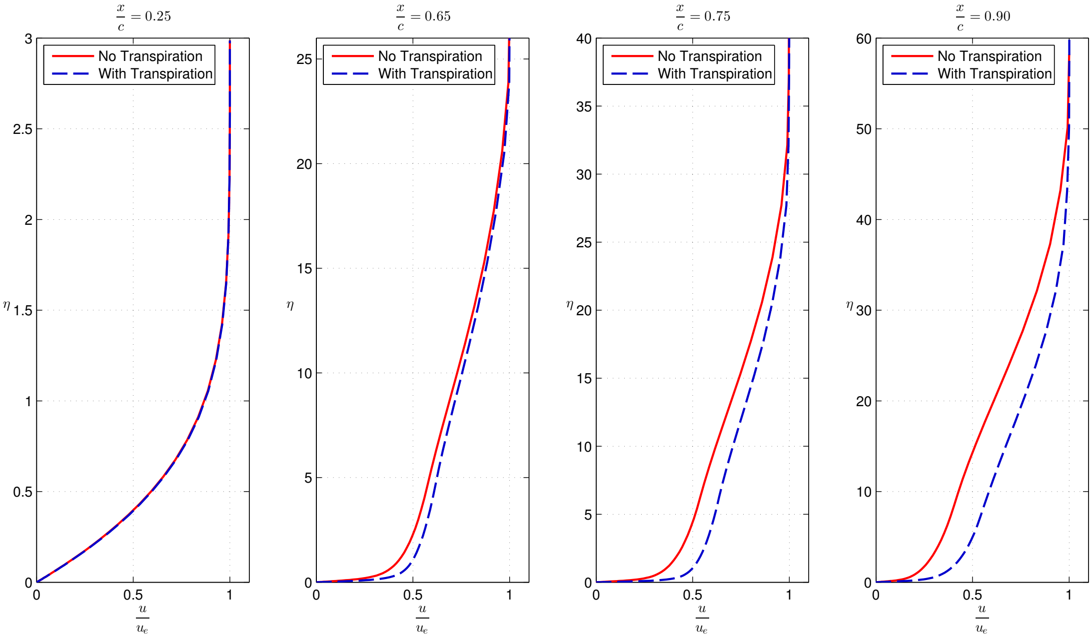

Figure 6.28: Boundary layer velocity profiles at several locations on upper surface.

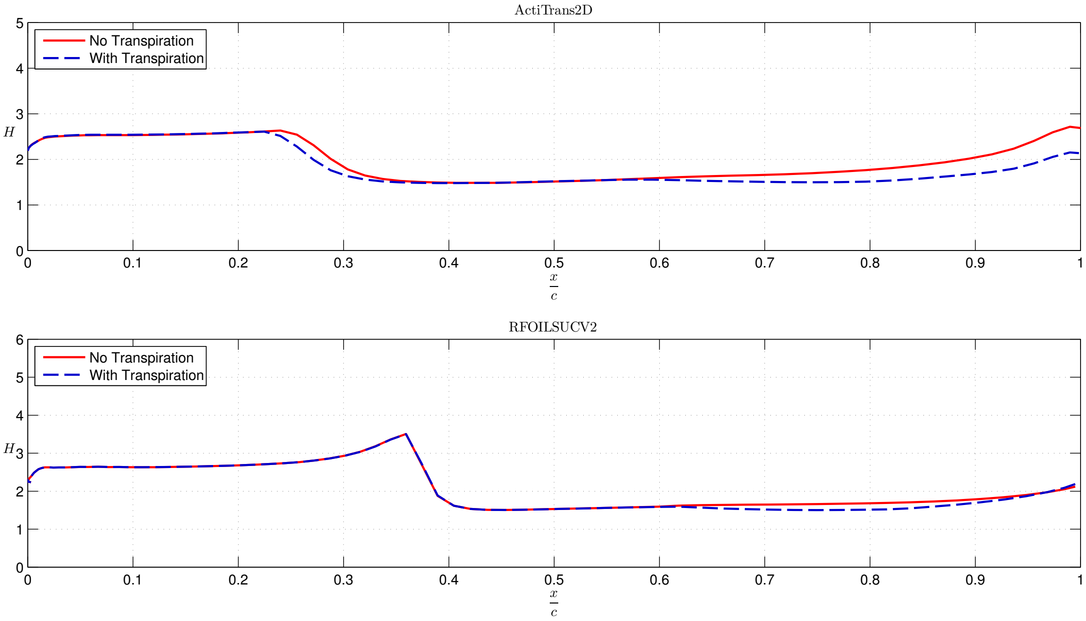

Figure 6.29: Shape factor comparison upper surface.

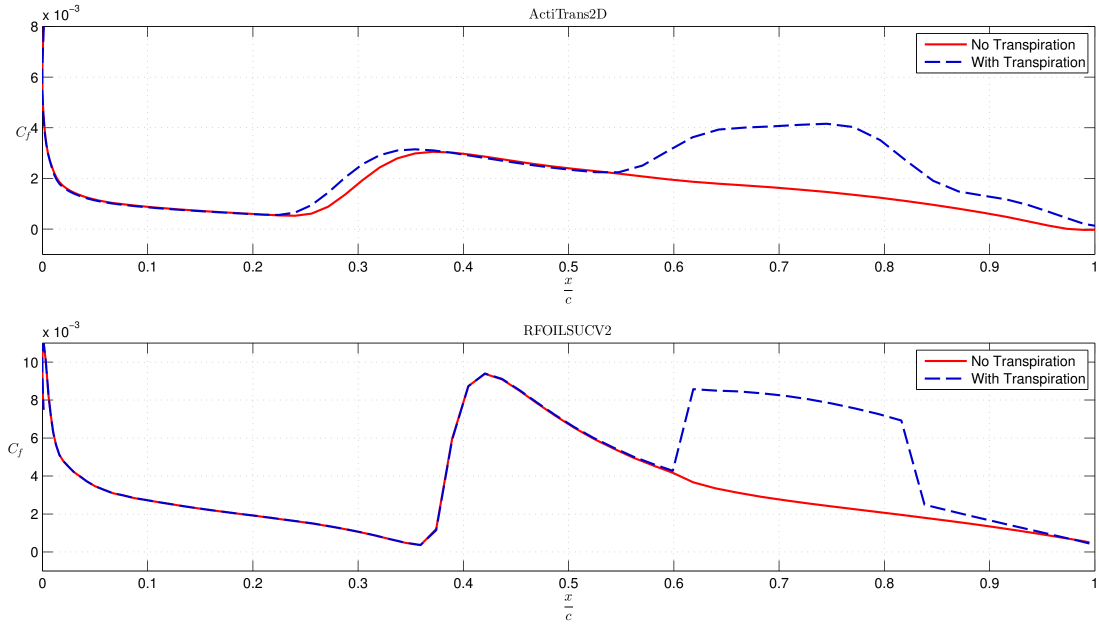

Figure 6.30: Skin friction coefficient comparison upper surface.

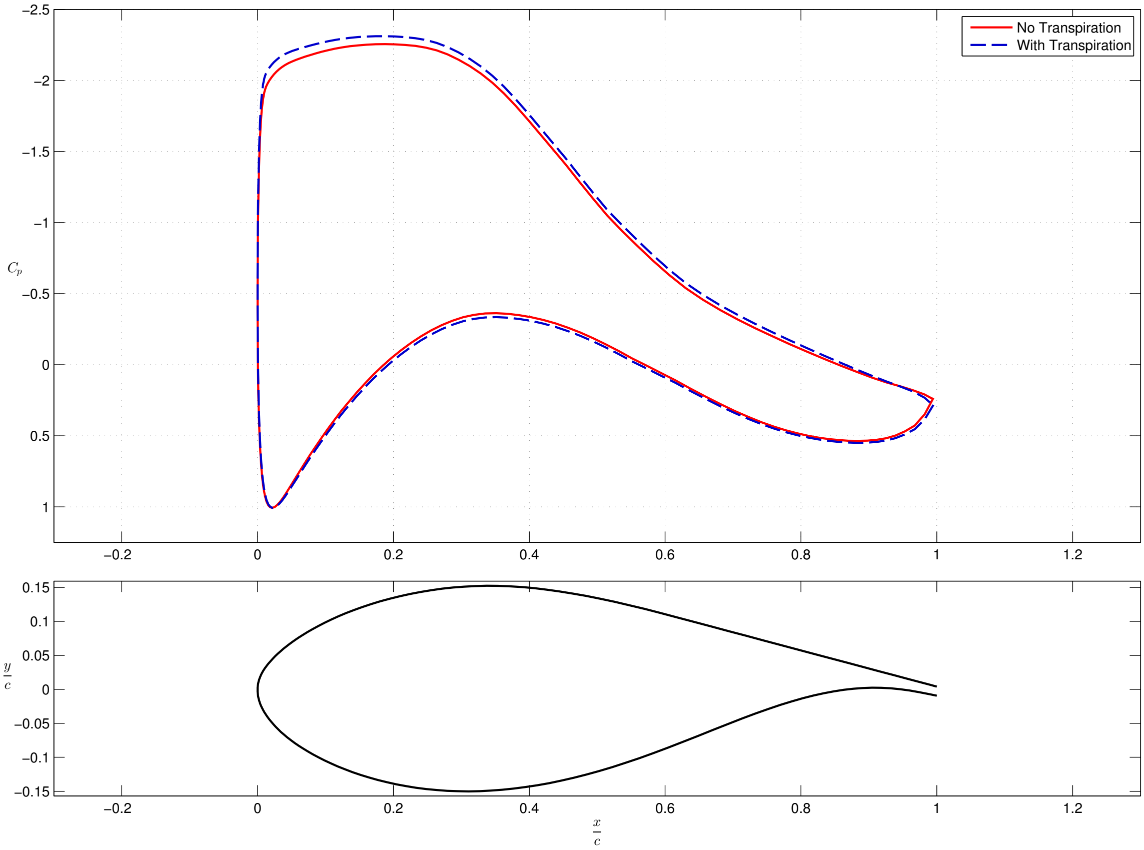

Figure 6.31: Pressure coefficient comparison.

6.4 Test case: FFA-W3-241

To investigate the effect of the location and quantity of the mass transfer distribution on the airfoil properties, the FFA-W3-241 airfoil is chosen. As explained in Bertagnolio et al. [2001], this airfoil is used on the inboard part of different Danish wind turbine blades. Measurements were carried out on this profile without mass transfer in the VELUX wind tunnel that has an open test section. Subsection 6.4.1 will cover the geometry and case description used for the simulations and subsection 6.4.2 will present and discuss the airfoil properties.

6.4.1 Case description

The geometry of the airfoil can be seen in figure 6.32. Note that it is thinner than the AF 0901 profile and has a closed trailing edge. The full case description for which the simulations in ACTITRANS2D were performed can be found in table 6.5.

Table 6.5: Case description

Airfoil Parameters			
Type		FFA-W3-241	
Angle of Attack		0^o to 18^o	
Freestream Reynolds Number		$1.6 \cdot 10^6$	
Freestream Mach Number		0.1	
Coordinate file read in		Yes	
Wake panels		40	
Remeshed		Yes	
Finite Trailing Edge		No	
Boundary Layer Parameters			
Transition Prediction		Wazzan et al.	
Eddy−Viscosity Correction		Cebeci	
Roughness Effects		No	
Δh(0) for η−grid (upper/lower)		0.0005/0.005	
Multiplier for η−grid (upper/lower)		1.16/1.14	
Transpiration Distribution			
Mass Transfer (upper/lower)		Yes/No	
v_1:	$0.3 \leq \frac{x}{c} \leq 0.5$	$\frac{v_w}{u_\infty} = -0.003$	$C_q = 1.247 \cdot 10^{-3}$
v_2:	$0.5 \leq \frac{x}{c} \leq 0.7$	$\frac{v_w}{u_\infty} = -0.003$	$C_q = 1.325 \cdot 10^{-3}$
v_3:	$0.7 \leq \frac{x}{c} \leq 0.9$	$\frac{v_w}{u_\infty} = -0.003$	$C_q = 1.334 \cdot 10^{-3}$
v_4:	$0.3 \leq \frac{x}{c} \leq 0.5$	$\frac{v_w}{u_\infty} = -0.006$	$C_q = 2.494 \cdot 10^{-3}$
v_5:	$0.5 \leq \frac{x}{c} \leq 0.7$	$\frac{v_w}{u_\infty} = -0.006$	$C_q = 2.650 \cdot 10^{-3}$
v_6:	$0.7 \leq \frac{x}{c} \leq 0.9$	$\frac{v_w}{u_\infty} = -0.006$	$C_q = 2.668 \cdot 10^{-3}$

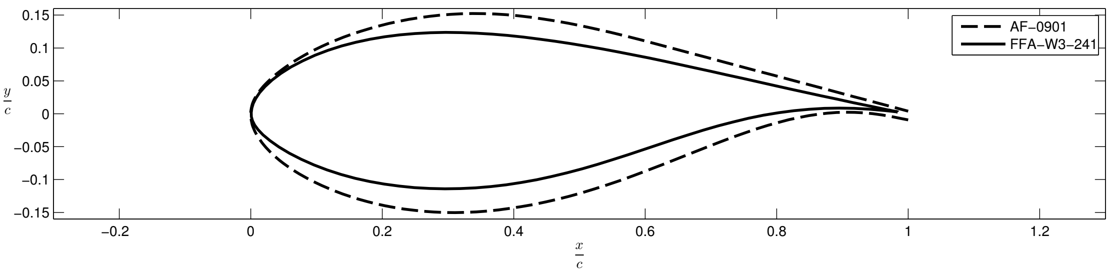

Figure 6.32: Geometry comparison AF 0901 versus FFA-W3-241.

6.4.2 Airfoil properties

The simulated airfoil properties can be found in figures 6.33 to 6.35. Below each of these figures, a short discussion is devoted to the observations that were made.

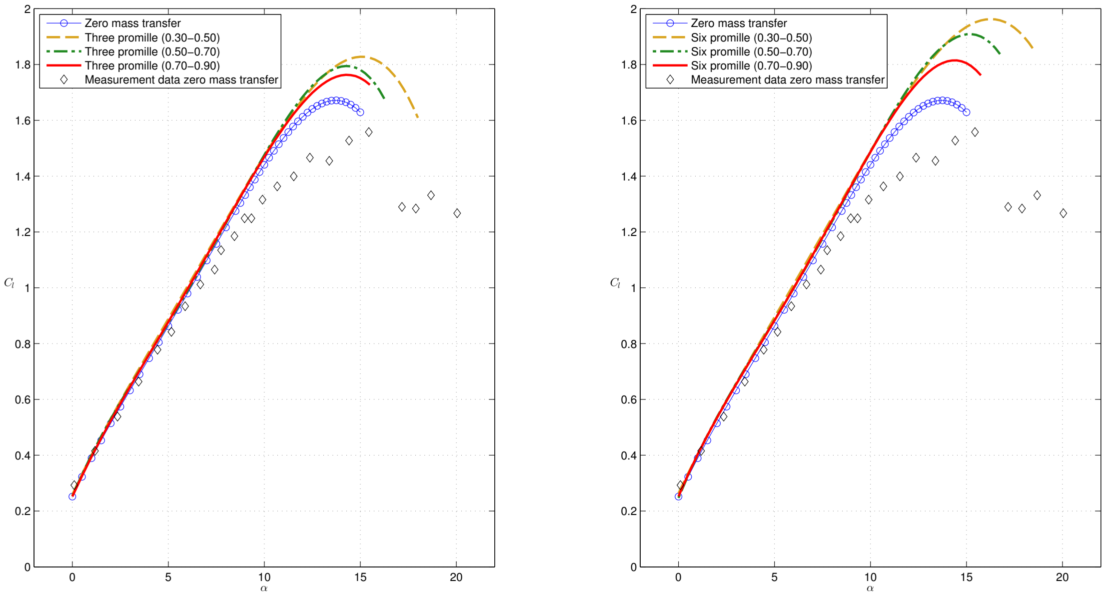

Figure 6.33: Lift coefficient curve FFA-W3-241.

In figure 6.33, the lift coefficient curve can be seen for the several transpiration distributions as well as the experimental data. First observe that computational results and experimental data are in rather good agreement up to eight degrees. After this linear region, more scatter in the measurement data is present and the agreement is worse. The maximum lift coefficient is reached at about two degrees angle of attack higher in the measurements than in the simulations (without mass transfer).

Next to this, some other interesting things might be seen in this figure. Note that in each subplot the suction quantity is the same but the location is varying. As becomes clear from both subplots, it is more efficient to place the suction distribution more forward. Moving each mass transfer distribution forward will result in a higher maximum lift coefficient as well as a higher stall angle.

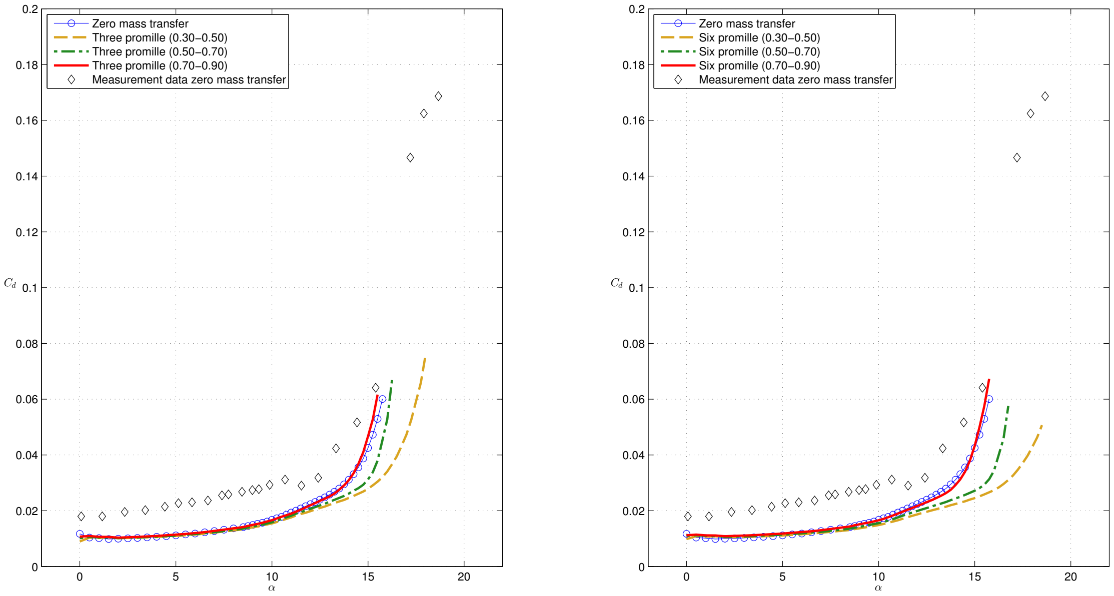

Figure 6.34: Drag coefficient curve FFA-W3-241.

Figure 6.34 is presenting the drag coefficient. This time, the drag coefficient is determined by the wake velocity profile (profile drag) plus the drag due to removal and stopping of the fluid (referred to as worst case sink drag). Leaving out the sink drag term will overestimate the gains of using suction (the drag coefficient will drop significant and hence the lift over drag ratio will increase too much). It also includes measurement data from Bertagnolio et al. [2001] (page 87, figure 115) without suction. Note that – although the values are quite a bit off – ACTITRANS2D is equally good or even better in its prediction than the design tools used in Bertagnolio et al. [2001].

Observe that when moving the suction distribution forward, the flow can be attached longer and the drag coefficient will stay lower. This observation holds for both suction quantities although this effect is even larger in the six promille suction cases. Notice that the case where suction is applied at the most rear location (seventy to ninety per cent chord), the drag coefficient is nearly the same as for the case without mass transfer. This time, the reduction in drag coefficient due to removal of momentum is balanced by the sink drag.

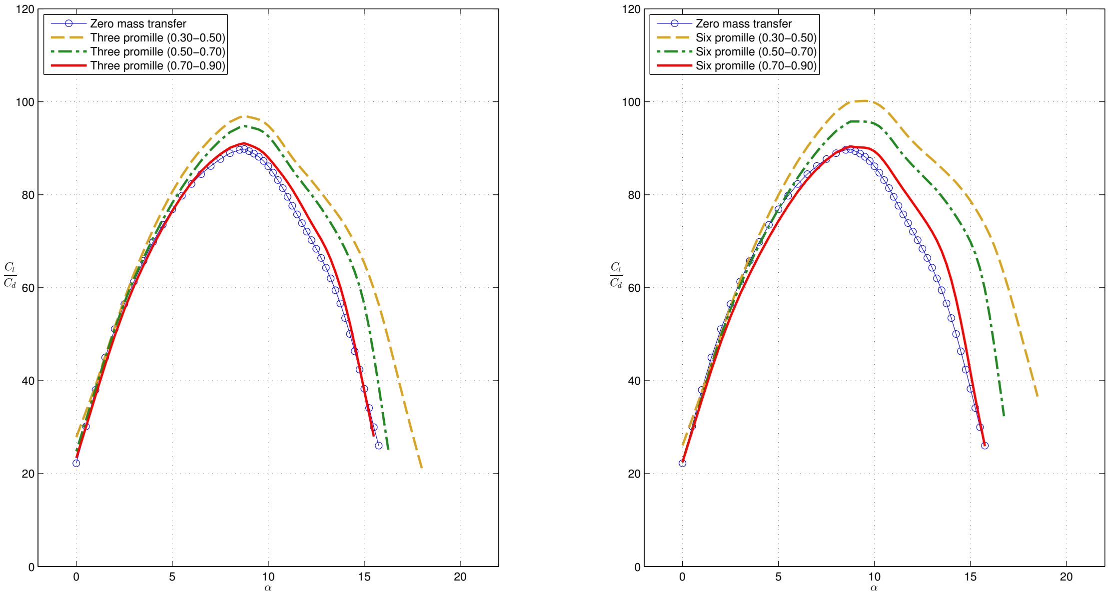

Figure 6.35: Lift-drag polar FFA-W3-241.

At last, the lift-drag polar is plotted for all suction distributions in figure 6.35. Again, moving the suction distribution forward will lead to higher lift over drag ratios. The same holds for increasing the suction amount. In the most favorable comparison (the one with six promille suction at the most forward position with the case without suction) it can be seen that the increase in lift over drag ratio is about 10%. Also note that when moving the suction distribution forward, the design angle of attack (where the lift over drag ratio reaches a maximum) is increased a bit.

CHAPTER
SEVEN

Conclusions and recommendations

In this thesis report, ways are provided to model the effect of boundary layer suction by using different computational techniques. Current methods are based on integral formulations to solve for the boundary layer equations and to include the effect of surface mass transfer. In this thesis, a finite difference formulation is used for this purpose. This led to the development of the design tool ACTITRANS2D which is validated by using analytical results and measurement data.
This chapter aims to present the reader the most important conclusions from the report as well as to give recommendations for future research on boundary layer suction.

Conclusions

Since the effect of boundary layer suction (or blowing) is especially important to predict airfoil properties in high Reynolds number flow, it is desired to couple a potential flow solver to a boundary layer solver. Usually, panel methods are used to compute this potential flow and to take viscous effects into account. In chapter 2, a low order and high order panel method are compared with exact von Kármán-Trefftz theory for two different airfoils. It is shown that for both methods, the relative error for the lift coefficient with exact theory remains within 0.5%. It is assumed that for the purpose of this thesis, the low order panel method is of sufficient accuracy and will be used in ACTITRANS2D. Of course, a state of the art panel method would increase the accuracy and convergence but as a cost it will also increase the complexity and programming effort.

As mentioned, solving for the boundary layer together with modifications for surface mass transfer, both a finite difference and integral method can be used. The former one offers more flexibility and is more general applicable but, as a disadvantage, requires more computation time. This makes it difficult to use it in optimization tools. For the latter one, numerous variations are available to correct the closure models for the effect of mass transfer. Often, each of these modifications is only valid for a specific case and are mostly not well validated.

Based on the control volume analysis in section 3.7, it is shown that the sink drag must be accounted for separately. This means it should be added to the profile drag (pressure drag plus friction drag) since this is determined via the Squire−Young formula based on the boundary layer properties.

To verify the modifications for boundary layer suction in ACTITRANS2D, a proper validation procedure should be carried out. By comparing the results of ACTITRANS2D with analytical laminar flat plate results with and without suction, it can be observed that the boundary layer properties and velocity profiles indeed converge to the correct asymptotic values and hence it can be concluded that the boundary conditions are implemented correctly. Since no analytical results are present for the turbulent flat plate, validation of the modifications on the turbulence model is heavily dependent on empirical data. Using ACTITRANS2D, the (blowing) measurements of McQuaid [1967] are simulated well and the (suction) measurements of Favre et al. [1961] are quite off. Simulating (old) measurements using the design tool is still very difficult because mostly it is not clear under what external conditions the measurements were taken. To give clear cut answers whether or not the implementations to the turbulence model are correct, far more extensive data sets should be available, especially for a turbulent flat plate with or without suction.

Chapter 6 is the most important chapter in this thesis report as it contains predictions of airfoil and boundary layer properties for several airfoils with and without suction.
For the first – NACA 0012 – airfoil, sixteen different suction distributions were compared and divided in four main blocks (constant region increased turbulent suction, varying region constant turbulent suction, varying region constant laminar suction, slot suction turbulent region with varying strength and location). Based on that discussion, the suction distribution is dependent on the goal that is pursued. By applying laminar suction from the leading edge forward, the flow can be kept laminar and smaller suction strengths would be necessary as compared with turbulent suction (less effect of the sink drag). This type will lead to higher lift-over-drag ratios. Furthermore, if one aims to prevent turbulent separation, suction in the turbulent region should be applied. Note that this will increase the maximum lift coefficient as well as the drag coefficient due to the significant sink drag component. Also note that for the same suction volume, it is more efficient (but often less practical) to distribute suction than confine it to a small region (a slot).
A NACA 4418 profile is chosen to compare between the versions of RFOIL extended for suction (i.e. RFOILSUC and RFOILSUCV2) and ACTITRANS2D. It can be concluded that the effect of boundary layer suction is overpredicted in RFOILSUC and comparable between RFOILSUCV2 and ACTITRANS2D. Note that when applying suction, the pressure distribution will go to a more inviscid case and hence the leading edge pressure peak will be higher. This can lead to earlier transition.
Since measurement data on airfoils with suction is very scarce, Actiflow B.V. performed wind tunnel tests on the AF 0901 profile. This provides a valuable way to compare the simulations of ACTITRANS2D and RFOILSUCV2 with the real world. From this study it can be seen that by increasing the amount of suction, the maximum lift coefficient will increase and will be reached at a higher angle of attack. Up to stall, correspondence between ACTITRANS2D and measurement data is good. RFOILSUCV2 overpredicts the effect of suction and suffers from numerical errors for relatively high suction strengths.
As a last simulation, predictions were made for the FFA-W3-241 airfoil with ACTITRANS2D. This to show the possible gains on a real wind turbine profile and to compare it with experimental results from a different wind tunnel (without suction). This profile is used on the

inboard part of several Danish wind turbine blades and requires a high maximum lift coefficient. Although the simulations are quite a bit off, ACTITRANS2D performs equally good or even better in its prediction than equivalent design tools used in Bertagnolio et al. [2001]. It is more efficient to place the suction distribution more to the front since then a higher maximum lift coefficient and stall angle can be reached. This behaviour can be seen for each suction strength. It is also shown that by applying six promille suction at thirty to fifty per cent chord on the upper side, the maximum lift-over-drag ratio can be increased by about 10%.

With this thesis research, an alternative design tool became available that is capable of predicting the effect of boundary layer suction on two dimensional surfaces by using a finite difference formulation for the boundary layer. It may be used in design phases in the various application fields as outlined in chapter 1. Recommendations for future research are found in the next paragraph.

Recommendations

Although it is believed that, with this thesis, a step has been made forward in modeling boundary layer suction, various recommendations can be given for future research. According to the present author, the most important ones are outlined in this paragraph.

First of all, measurement data on turbulent boundary layers with distributed suction is very scarce. To be able to validate and improve current turbulence models, it is recommended to perform extensive wind tunnel tests on a simple flat plate turbulent boundary layer with and without suction. It should become clear what happens to the velocity profiles thoughout this boundary layer. Such measurement data will be extremely valuable to everyone interested in modeling boundary layer suction.

For practical application, it is often important to determine what happens with the flow with or without surface mass transfer near and after massive separation from the surface. It is known that the boundary layer equations will not be valid in this situation and alternative computational techniques must be used. For this purpose, more sophisticated computational methods should be used. This could range from solving the RANS equations with appropriate turbulence modeling to DNS. Inbetween, the option of LES is located. With these methods, more information could be obtained about the (3D) flow structure around, for example, the suction device. To do this, commercial CFD packages might be handy. It should be stressed that this thesis aimed to study the effect of boundary layer suction by solving the boundary layer equations using a finite difference and integral method for attached and slightly separated boundary layers. Moving to a more general applicable method to model boundary layer suction and the effect of it on the flow structure opens a relatively new research domain.

Since the tool is not yet suitable for usage in optimization tools due to the larger computation time of the finite difference method as compared to the integral method, it would be beneficial to combine both methods. Since the most severe problems occur for the closure relations in the integral methods, one could use an integral method to solve for the laminar boundary layer and a finite difference method to solve the turbulent boundary layer (both with or without suction).

APPENDIX

A

Block Diagrams Code Structure

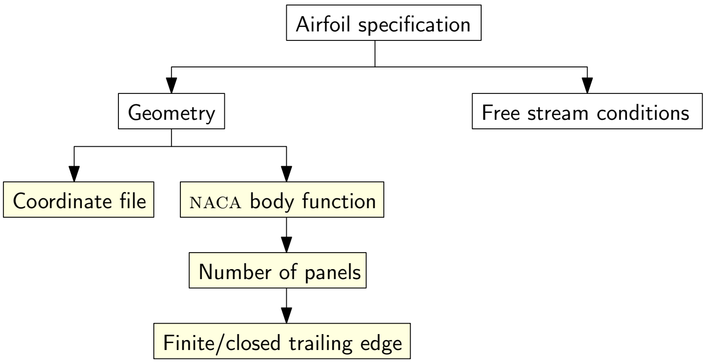

Figure A.1: Airfoil configuration block.

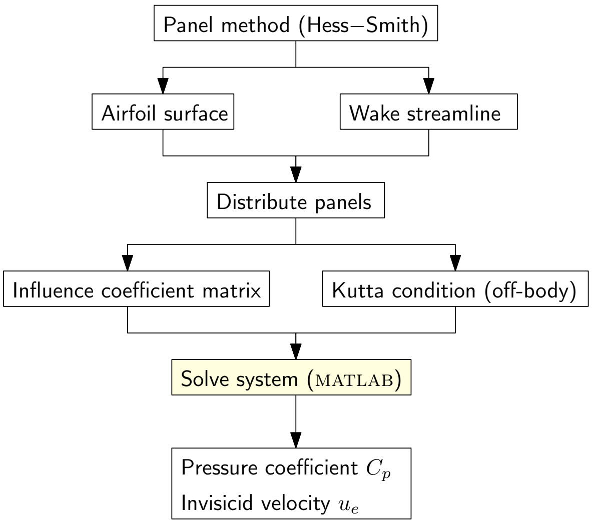

Figure A.2: Panel method architecture.

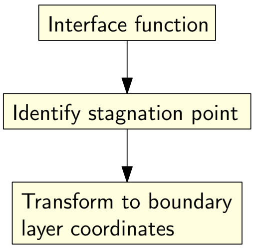

Figure A.3: Interface block.

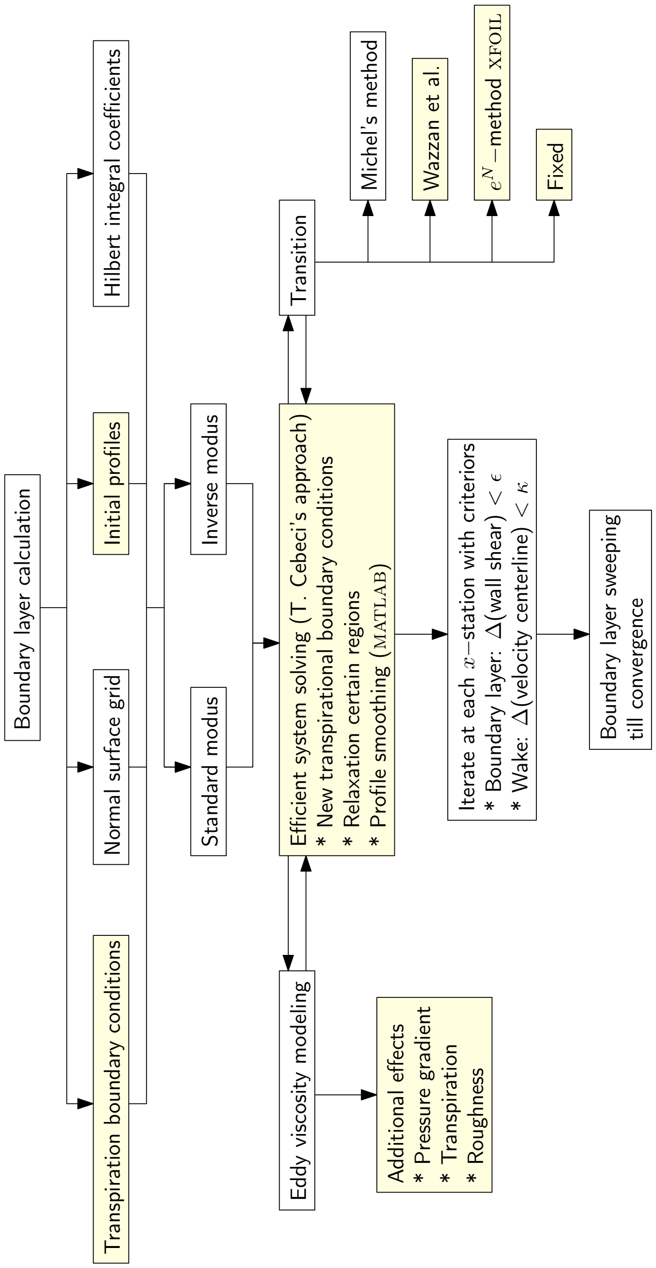

Figure A.4: Boundary layer method.

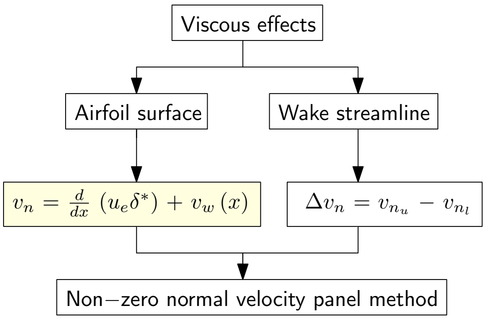

Figure A.5: Include viscous effects.

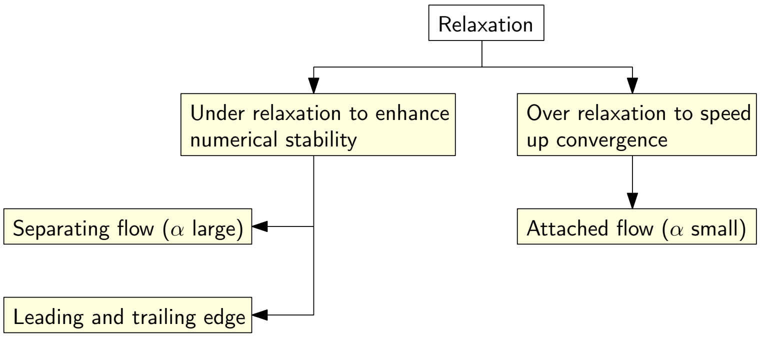

Figure A.6: Relaxation principles.

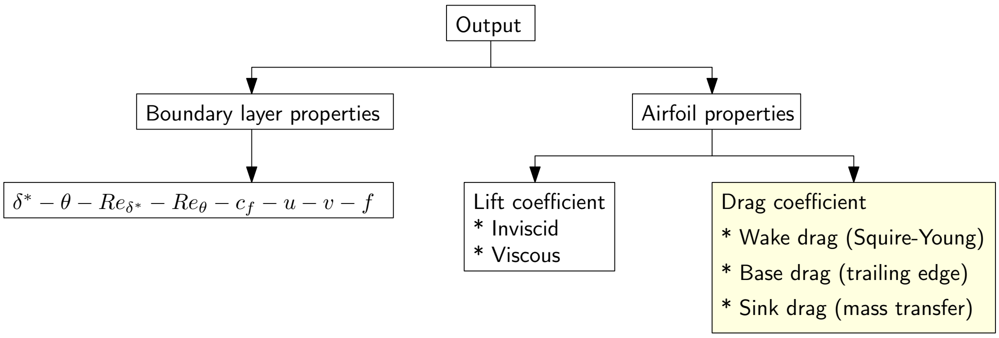

Figure A.7: Output parameters.

APPENDIX

B

NACA Body Creation and Repaneling

In order to create a NACA profile, specific steps should be followed. The theory can be found in Abbott and von Doenhoff [1959]. In essence, the geometry is created by combining mean lines and thickness distributions together according to the following formulae:

Upper side:	Lower side:
$x_U = x - y_t \cdot \sin\theta$	$x_L = x + y_t \cdot \sin\theta$
$y_U = y_c + y_t \cdot \cos\theta$	$y_L = y_c - y_t \cdot \cos\theta$

In these equations, x is the chordwise position, y_t is the thickness distribution, y_c represents the mean line and θ the slope of the mean line.

NACA four digit series

For this NACA type, the thickness distribution is given by formula B.1 in which t represents the maximum thickness in percentage chord.

$$\pm y_t = \frac{t}{0.20}\left(0.29690\sqrt{x} - 0.12600x - 0.35160x^2 + 0.28430x^3 - 0.10150x^4\right) \tag{B.1}$$

The mean line is given by equation B.2.

$$\begin{aligned} y_c &= \frac{m}{p^2}\left(2px - x^2\right) && \text{before maximum of the mean line} \\ y_c &= \frac{m}{(1-p)^2}\left[(1-2p) + 2px - x^2\right] && \text{after maximum of the mean line} \end{aligned} \tag{B.2}$$

Note that for the mean line, two parabolic arcs are used, one before the maximum value of the mean line and one aft. Parameter p represents the location in percentage chord and m the maximum value in fraction chord. The systematic numbering can be summarized as:

First digit:	Maximum camber in percentage chord.
Second digit:	Location maximum camber in tenths of chord.
Third and fourth digit:	Profile thickness in percentage chord.

As an example, a NACA 4412 profile discretized in 120 panels can be seen in figure B.1. This time, the chordwise position is divided in equally spaced segments. A different distribution is explained in the last paragraph of this appendix.

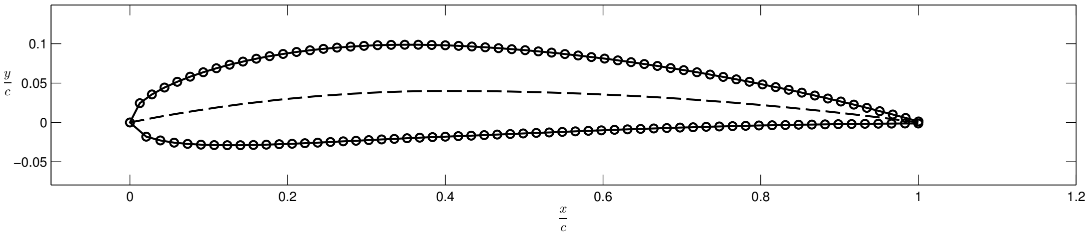

Figure B.1: NACA 4412 including camber line discretized with equally spaced segments.

NACA five digit series

For these type of airfoils, the same thickness distribution applies as given by equation B.1. This time, the mean line is given by equation B.3.

$$\begin{aligned} y_c &= \frac{1}{6}k_1\left[x^3 - 3mx^2 + m^2\left(3-m\right)x\right] && 0 \leq x \leq m \\ y_c &= \frac{1}{6}k_1 m^3\left(1-x\right) && m \leq x \leq 1 \end{aligned} \tag{B.3}$$

Now, parameters m and k_1 are presented in tables in Abbott and von Doenhoff [1959] for five positions of the maximum camber. The systematic numbering can be summarized as:

First digit:	Three halves times this number equals the design lift coefficient.
Second and third digit:	Divided by two – maximum camber position in percentage chord.
Fourth and fifth digit:	Profile thickness in percentage chord.

Figure B.2 illustrates a NACA 23012 with 160 panels equally spaced along the $x-$axis.

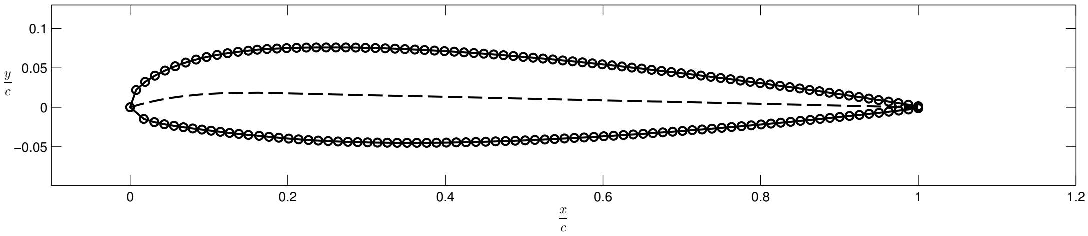

Figure B.2: NACA 23012 including camber line discretized with equally spaced segments.

Trailing edge gap

From the original definition of a NACA body, it may be noticed that the geometry has a finite trailing edge. For computational purposes it may be useful to have a zero trailing edge thickness. In ACTITRANS2D this has been modeled by adjusting the value before the fourth order term in B.1 to -0.10360 instead of -0.10150. This ensures that at $x = 1$, y_t becomes zero[10]. Note that many design tools use different techniques for this. To be strict, it should now be called a modified NACA profile since the original formulae are violated. To illustrate the effect of creating a zero trailing edge thickness, figure B.3 is included.

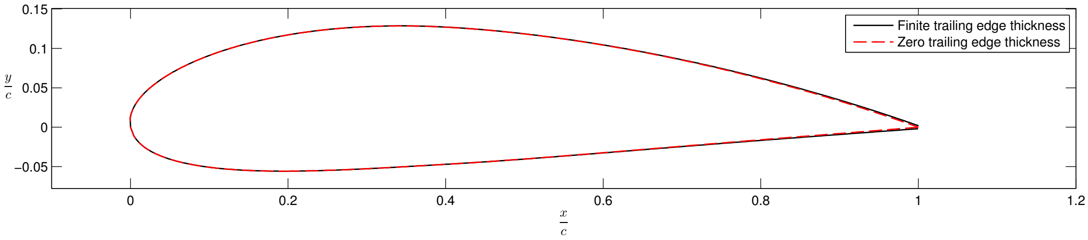

Figure B.3: Influence the NACA 4418 geometry after creating zero trailing edge thickness.

From figure B.3 it can be seen that the trailing edge region is influenced most (the rest is nearly the same).

Repaneling

In order to achieve better convergence, a different paneling could be applied. It would be beneficial to have more panels in the leading and trailing edge regions since the most severe fluctuations occur here. For this purpose, one can select a half cosine distributed paneling in ACTITRANS2D. To explain this concept, figure B.4 is created.

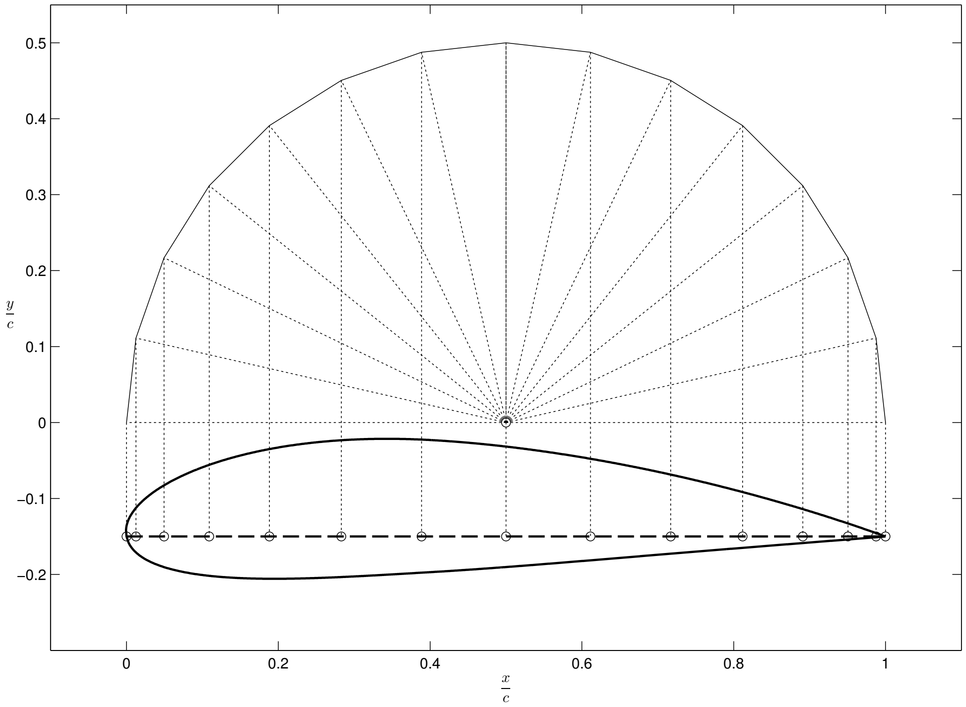

Figure B.4: Half cosine distribution on a NACA 4418 profile.

---

[10] From `http://www.mathworks.com/matlabcentral/fileexchange/19915-naca-4-digit-airfoil-generator` and `http://en.wikipedia.org/wiki/NACA_airfoil`. Both sources are referring that it has the least change to the overall shape of the airfoil.

For a uniformly distributed mesh, the chordwise position is divided in equally spaced segments. Mapping this position to the airfoil surface defines the panel points. Connecting these points will give the actual panels that are used in the Hess−Smith panel method.
Now, this distribution can be changed to get more panels in the leading and trailing edge regions. The chordwise points are now determined by equation B.4.

$$\frac{x}{c} = \frac{1}{2}\left(\cos\xi + 1\right) \qquad\qquad \pi \leq \xi \leq 2\pi \tag{B.4}$$

These points can be seen in figure B.4 as the circles on the chord of the profile. Formula B.4 can be imagined as first creating a half circle with a uniform step in the angle ξ. Then, these points on the circle can be mapped on the airfoil's chord as can be seen in figure B.4. Again, the corresponding points on the surface will define the panel points and connecting these yield the panels.
Illustration of the different panel distributions can be seen in figure B.5.

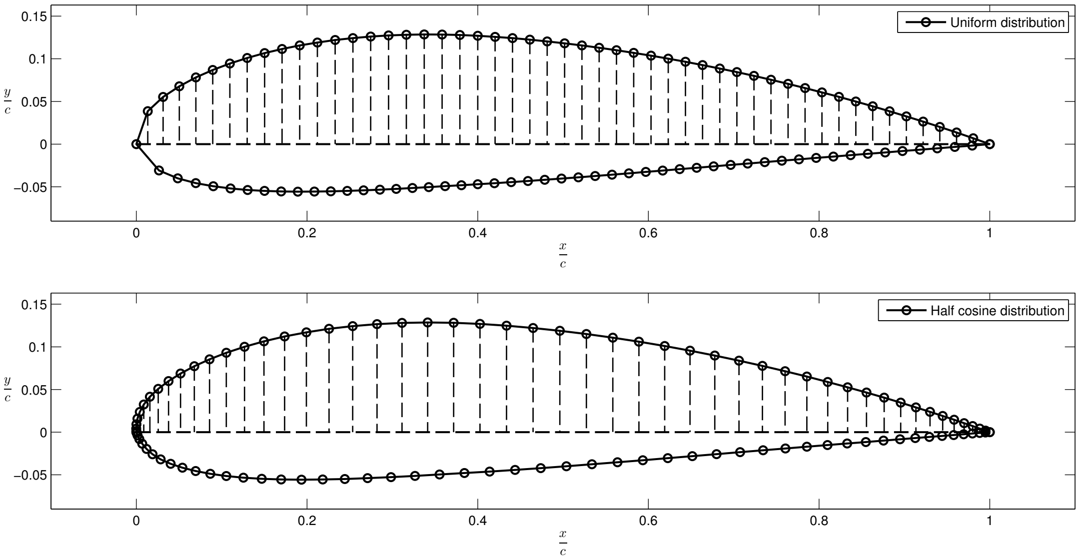

Figure B.5: NACA 4418 profile with 100 panels.

APPENDIX

C

Hess–Smith panel method

This appendix contains some more elaboration on the terms present in equations 2.2 and 2.3. In equation 2.2, A_{ij}^n and B_{ij}^n are called the influence coefficients. They denote the velocity induced at the $i-$th panel by a unit strength source or vorticity distribution imposed at the $j-$th panel. They are related to the airfoil geometry and panel arrangement by the following expressions:

$$
\begin{aligned}
A_{ij}^n &= \begin{cases} \dfrac{1}{2\pi}\left[\sin\left(\theta_i-\theta_j\right)\ln\dfrac{r_{i,j+1}}{r_{i,j}}+\cos\left(\theta_i-\theta_j\right)\beta_{ij}\right] & i\neq j \\ \dfrac{1}{2} & i=j \end{cases} \\
B_{ij}^n &= \begin{cases} -\dfrac{1}{2\pi}\left[\sin\left(\theta_i-\theta_j\right)\beta_{ij}-\cos\left(\theta_i-\theta_j\right)\ln\dfrac{r_{i,j+1}}{r_{i,j}}\right] & i\neq j \\ 0 & i=j \end{cases}
\end{aligned}
$$

with:

$$
\begin{aligned}
r_{i,j+1} &= \left[\left(x_{m_i}-x_{j+1}\right)^2+\left(y_{m_i}-y_{j+1}\right)^2\right]^{1/2} & r_{i,j} &= \left[\left(x_{m_i}-x_j\right)^2+\left(y_{m_i}-y_j\right)^2\right]^{1/2} \\
x_{m_i} &= \frac{1}{2}\left(x_i+x_{i+1}\right) & y_{m_i} &= \frac{1}{2}\left(y_i+y_{i+1}\right) \\
\theta_i &= \tan^{-1}\left(\frac{y_{i+1}-y_i}{x_{i+1}-x_i}\right) & \theta_j &= \tan^{-1}\left(\frac{y_{j+1}-y_j}{x_{j+1}-x_j}\right) \\
\beta_{ij} &= \tan^{-1}\left(\frac{y_{m_i}-y_{j+1}}{x_{m_i}-x_{j+1}}\right)-\tan^{-1}\left(\frac{y_{m_i}-y_j}{x_{m_i}-x_j}\right)
\end{aligned}
\tag{C.1}
$$

In equation 2.3, A is a square matrix of order $(N+1)$:

$$A = \begin{bmatrix} a_{11} & a_{12} & \cdots & a_{1j} & \cdots & a_{1N} & a_{1,N+1} \\ a_{21} & a_{22} & \cdots & a_{2j} & \cdots & a_{2N} & a_{2,N+1} \\ \vdots & \vdots & \vdots & \vdots & \vdots & \vdots & \vdots \\ a_{i1} & a_{i2} & \cdots & a_{ij} & \cdots & a_{iN} & a_{i,N+1} \\ \vdots & \vdots & \vdots & \vdots & \vdots & \vdots & \vdots \\ a_{N1} & a_{N2} & \cdots & a_{Nj} & \cdots & a_{NN} & a_{N,N+1} \\ a_{N+1,1} & a_{N+1,2} & \cdots & a_{N+1,j} & \cdots & a_{N+1,N} & a_{N+1,N+1} \end{bmatrix}$$

$\mathsf{x} = (q_1, \cdots, q_i, \cdots, q_N, \tau)^T$ and $\mathbf{b} = (b_1, \cdots, b_i, \cdots, b_N, b_{N+1})^T$. The elements of A follow from equation 2.2.

$$\begin{aligned} a_{ij} &= A^n_{ij} \qquad\qquad i = 1, 2, ..., N \\ a_{i,N+1} &= \sum_{j=1}^{N} B^n_{ij} \qquad\qquad j = 1, 2, ..., N \end{aligned} \tag{C.2}$$

By using the Kutta condition one can find the coefficients $a_{N+1,j}$ and $a_{N+1,N+1}$:

$$\begin{aligned} a_{N+1,j} &= A^t_{1j} + A^t_{Nj} \\ a_{N+1,N+1} &= \sum_{j=1}^{N} \left(B^t_{1j} + B^t_{Nj}\right) \end{aligned} \tag{C.3}$$

By using equation C.4, the influence coefficient matrix should now be fully defined. Note that this presents a very concise description of the Hess–Smith panel method. For further details see Cebeci [1999].

$$\begin{aligned} B^n_{ij} &= -A^t_{ij} \\ B^t_{ij} &= -A^n_{ij} \end{aligned} \tag{C.4}$$

The right hand side vector is determined by equation C.5.

$$\begin{aligned} b_i &= -V_\infty \sin\left(\alpha - \theta_i\right) \qquad\qquad i = 1, 2, ..., N \\ b_{N+1} &= -V_\infty \cos\left(\alpha - \theta_1\right) - V_\infty \cos\left(\alpha - \theta_N\right) \end{aligned} \tag{C.5}$$

APPENDIX

D

Conformal Mapping

As mentioned, conformal mapping is usually performed between two complex planes. In a nutshell, if lifting flow around a cylinder is imposed in one complex plane, making use of the von Kármán–Trefftz mapping can generate lifting airfoil flow in another complex plane. Knowing that the flow of an ideal fluid can be represented by either a scalar function $\phi\left(x,y\right)$ – the velocity potential – or the scalar function $\psi\left(x,y\right)$ – the stream function – and that they both have to satisfy Laplace's equation, one may write the velocity components as:

$$\begin{aligned} u &= \frac{\partial \phi}{\partial x} = \frac{\partial \psi}{\partial y} \\ v &= \frac{\partial \phi}{\partial y} = -\frac{\partial \psi}{\partial x} \end{aligned} \tag{D.1}$$

Contruction of the complex potential – $\Phi\left(z\right)$ – can be done by assigning the real part to be the velocity potential and the imaginary part to be the stream function:

$$\Phi\left(z\right) = \phi\left(x,y\right) + i\psi\left(x,y\right) \tag{D.2}$$

For lifting cylinder flow, the complex potential can be set up by superposition of a uniform, doublet and vortex flow in complex form. Using the properties of complex numbers named after Leonhard Euler[11] as well as the elementary flow solutions described in section 2.1 and equation D.2, one can write:

$$\begin{aligned} z &= x + iy = re^{i\theta} \\ &= r\left(\cos\theta + i\sin\theta\right) \\ r^2 &= x^2 + y^2 \end{aligned} \tag{D.3}$$

---

[11] 15 April 1707 – 18 September 1783, pioneering Swiss mathematician and physicist. One of the most productive of all times and responsible for many modern mathematical terminology.

$$\begin{aligned}
\text{Uniform:} \quad \Phi_u(z) &= V_\infty x + iV_\infty y \\
&= V_\infty r\cos\theta + iV_\infty r\sin\theta \\
&= V_\infty z \\
\text{Doublet:} \quad \Phi_d(z) &= \frac{\kappa}{2\pi}\frac{\cos\theta}{r} - i\frac{\kappa}{2\pi}\frac{\sin\theta}{r} \\
&= a^2 V_\infty \left(\frac{1}{r}\right)(\cos\theta - i\sin\theta) \\
&= a^2 V_\infty \left(\frac{\cos\theta + i\sin\theta}{z}\right)(\cos\theta - i\sin\theta) \\
&= \frac{a^2 V_\infty}{z} \\
\text{Vortex:} \quad \Phi_v(z) &= -\frac{\Gamma}{2\pi}\theta + i\frac{\Gamma}{2\pi}\ln r \\
&= \frac{i\Gamma}{2\pi}(\ln r + i\theta) \\
&= \frac{i\Gamma}{2\pi}\ln\left(re^{i\theta}\right) \\
&= \frac{i\Gamma}{2\pi}\ln(z) \\
\text{Total:} \quad \Phi(z) &= \Phi_u + \Phi_d + \Phi_v \\
&= V_\infty\left(z + \frac{a^2}{z}\right) + \frac{i\Gamma}{2\pi}\ln(z)
\end{aligned} \tag{D.4}$$

Note: $a = \sqrt{\frac{\kappa}{2\pi V_\infty}}$ equals the cylinder radius (Anderson [2007]).

An interesting property of the complex potential is that its derivative is the complex conjugate of the 'real' fluid velocity, $u + iv$. This can be shown when taking $\frac{d\Phi}{dz}$ where the increment dz is taken in $x-$direction:

$$\begin{aligned}
\frac{d\Phi}{dz} &= \frac{\partial\Phi}{\partial x} = \frac{\partial\phi}{\partial x} + i\frac{\partial\psi}{\partial x} \\
&= u - iv
\end{aligned} \tag{D.5}$$

Now, consider the von Kármán$-$Trefftz transformation between two planes (let the $\zeta-$plane resemble the cylinder and the $Z-$plane the corresponding airfoil), then the mapping function is given by:

$$\begin{aligned}
Z &= \frac{nl\left[(\zeta + l)^n + (\zeta - l)^n\right]}{(\zeta + l)^n - (\zeta - l)^n} \\
\frac{dZ}{d\zeta} &= 4n^2 l^2 \frac{\left[(\zeta - l)^{n-1}(\zeta + l)^{n-1}\right]}{\left[(\zeta + l)^n - (\zeta - l)^n\right]^2} \\
n &= 2 - \frac{\tau}{\pi}
\end{aligned} \tag{D.6}$$

where τ is a free parameter to specify the trailing edge angle and l is a real constant.

Now that the mapping and its derivative is known, determination of the fluid velocity in the

$Z-$plane (airfoil) can easily be derived from the fluid velocity in the $\zeta-$plane (cylinder) by making use of D.5:

$$\begin{aligned}[u-iv]_Z &= \frac{d\Phi}{dZ} = \frac{d\Phi}{d\zeta}\frac{d\zeta}{dZ} \\ &= \frac{[u-iv]_\zeta}{\frac{dZ}{d\zeta}}\end{aligned} \tag{D.7}$$

From D.7 it can be seen that all that is necessary to compute the flow around an airfoil is the velocity around the cylinder (from the complex potential in equation D.4) as well as the derivative of the mapping function.

To analyze an airfoil using the von Kármán–Trefftz transformation, first specify a cylinder in the $\zeta-$plane (see figure D.1) by setting the variables:

l : Chord length $\approx 4l$
α : Angle of attack
ϵ : Thickness parameter
κ : Camber parameter
τ : Trailing edge angle

and then use the relations (Masatsuka [2009], including an angle of attack):

$$\begin{aligned}\beta &= \sin^{-1}\left(\frac{l\kappa}{a}\right) \\ \mu &= l\left(\epsilon + i\kappa\right) \\ a &= l\sqrt{(1-\epsilon)^2+\kappa^2} \\ [u-iv]_\zeta &= V_\infty\left(e^{-i\alpha} + i\frac{2a\sin\left(\alpha+\beta\right)}{\zeta-\mu} - \frac{a^2e^{i\alpha}}{(\zeta-\mu)^2}\right)\end{aligned}$$

This concludes the most important aspects of conformal mapping using the von Kármán–Trefftz transformation.

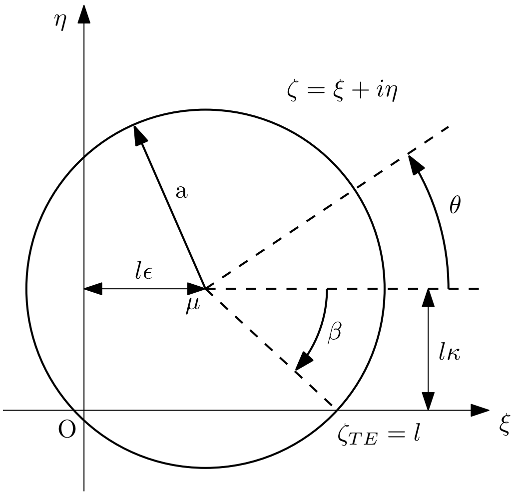

Figure D.1: Cylinder parameters in $\zeta-$plane that is mapped to an airfoil in the $Z-$plane (Masatsuka [2009]).

APPENDIX

E

Momentum Integral Equation with Mass Transfer

To obtain the momentum integral equation, some mathematical tricks should be applied to turn the partial differential equations of expression 3.16 to an ordinary diffential equation form of expression E.5. First of all, multiply the continuity equation with $(u_e - u)$ and subtract this from the x-momentum equation:

$$\begin{aligned} (u_e - u)\frac{\partial u}{\partial x} + (u_e - u)\frac{\partial v}{\partial y} &= 0 \\ u\frac{\partial u}{\partial x} + v\frac{\partial u}{\partial y} &= u_e\frac{du_e}{dx} + \frac{1}{\rho}\frac{\partial \tau}{\partial y} \end{aligned} \tag{E.1}$$

After subtraction, this will give the next result:

$$2u\frac{\partial u}{\partial x} - u_e\frac{\partial u}{\partial x} + v\frac{\partial u}{\partial y} + u\frac{\partial v}{\partial y} - u_e\frac{\partial v}{\partial y} - u_e\frac{\partial u_e}{\partial x} = \frac{1}{\rho}\frac{\partial \tau}{\partial y}$$

For reasons that will become clear soon, multiply this with -1:

$$-2u\frac{\partial u}{\partial x} + u_e\frac{\partial u}{\partial x} - v\frac{\partial u}{\partial y} - u\frac{\partial v}{\partial y} + u_e\frac{\partial v}{\partial y} + u_e\frac{\partial u_e}{\partial x} = -\frac{1}{\rho}\frac{\partial \tau}{\partial y} \tag{E.2}$$

Next, define the following relations:

$$\begin{aligned} \frac{\partial}{\partial x}\left(uu_e - u^2\right) + (u_e - u)\frac{\partial u_e}{\partial x} &= u\frac{\partial u_e}{\partial x} + u_e\frac{\partial u}{\partial x} - 2u\frac{\partial u}{\partial x} + u_e\frac{\partial u_e}{\partial x} - u\frac{\partial u_e}{\partial x} \\ &= u_e\frac{\partial u_e}{\partial x} + u_e\frac{\partial u}{\partial x} - 2u\frac{\partial u}{\partial x} \\ \frac{\partial}{\partial y}\left(vu_e - uv\right) &= v\frac{\partial u_e}{\partial y} + u_e\frac{\partial v}{\partial y} - u\frac{\partial v}{\partial y} - v\frac{\partial u}{\partial y} \\ &= u_e\frac{\partial v}{\partial y} - u\frac{\partial v}{\partial y} - v\frac{\partial u}{\partial y} \end{aligned}$$

By comparing these two relations with equation E.2, one can rewrite this as:

$$\frac{\partial}{\partial x}\left(uu_e - u^2\right) + \left(u_e - u\right)\frac{\partial u_e}{\partial x} + \frac{\partial}{\partial y}\left(vu_e - uv\right) = -\frac{1}{\rho}\frac{\partial \tau}{\partial y} \tag{E.3}$$

This equation is now integrated from $y = 0$ to $y = \infty$. The four terms will be evaluated separately:

$$\begin{aligned}
\int_0^\infty \frac{\partial}{\partial x}\left(uu_e - u^2\right)\mathrm{d}y &= \frac{\mathrm{d}}{\mathrm{d}x}\int_0^\infty u_e^2\frac{u}{u_e}\left(1-\frac{u}{u_e}\right)\mathrm{d}y \\
&= \frac{\mathrm{d}}{\mathrm{d}x}\left(u_e^2\theta\right) \\
&= 2u_e\theta\frac{\mathrm{d}u_e}{\mathrm{d}x} + u_e^2\frac{\mathrm{d}\theta}{\mathrm{d}x} \\
\int_0^\infty \left(u_e - u\right)\frac{\partial u_e}{\partial x}\mathrm{d}y &= \frac{\mathrm{d}u_e}{\mathrm{d}x}\int_0^\infty u_e\left(1-\frac{u}{u_e}\right)\mathrm{d}y \\
&= \frac{\mathrm{d}u_e}{\mathrm{d}x}\delta^* u_e \\
\int_0^\infty \frac{\partial}{\partial y}\left(vu_e - uv\right)\mathrm{d}y &= -u_e v_w \\
-\frac{1}{\rho}\int_0^\infty \frac{\partial \tau}{\partial y}\mathrm{d}y &= \frac{\tau_w}{\rho}
\end{aligned}$$

Substitution of these four terms into equation E.3 gives equation E.4:

$$2u_e\theta\frac{\mathrm{d}u_e}{\mathrm{d}x} + u_e^2\frac{\mathrm{d}\theta}{\mathrm{d}x} + \frac{\mathrm{d}u_e}{\mathrm{d}x}\delta^* u_e - u_e v_w = \frac{\tau_w}{\rho} \tag{E.4}$$

Division by u_e^2 gives:

$$\left(2\theta + \delta^*\right)\frac{1}{u_e}\frac{\mathrm{d}u_e}{\mathrm{d}x} + \frac{\mathrm{d}\theta}{\mathrm{d}x} = \frac{C_f}{2} + \frac{v_w}{u_e}$$

Or finally:

$$\frac{\mathrm{d}\theta}{\mathrm{d}x} + \left(2 + H\right)\frac{\theta}{u_e}\frac{\mathrm{d}u_e}{\mathrm{d}x} = \frac{C_f}{2} + \frac{v_w}{u_e} \tag{E.5}$$

APPENDIX

F

Asymptotic Suction Laminar Flat Plate

Starting from the $x-$momentum equation with $\dfrac{\partial u}{\partial x} = 0$ and zero pressure gradient:

$$v_w \frac{du}{dy} = \nu \frac{d^2u}{dy^2} \tag{F.1}$$

Assume solutions of the exponential form and substitute:

$$u = e^{\lambda y} \qquad \frac{du}{dy} = \lambda e^{\lambda y} \qquad \frac{d^2u}{dy^2} = \lambda^2 e^{\lambda y} \tag{F.2}$$

Solving the resulting equation for λ will lead to $\lambda = 0$ or $\lambda = \dfrac{v_w}{\nu}$. Take a linear combination of the two possibilties:

$$u\left(y\right) = c_1 + c_2 \cdot e^{\left(\frac{v_w}{\nu}\right)y} \tag{F.3}$$

and use the boundary conditions (note that $v_w < 0$ and when $y \to \infty$, $e^{\left(\frac{v_w}{\nu}\right)y} \to 0$):

$$\begin{aligned} y &= 0 \qquad & u &= 0 \\ y &\to \infty \qquad & u &\to u_e = u_\infty \end{aligned} \tag{F.4}$$

to solve for the constants, one can write:

$$\begin{aligned} u\left(y\right) &= u_\infty - u_\infty e^{\left(\frac{v_w}{\nu}\right)y} \\ \frac{u\left(y\right)}{u_\infty} &= 1 - e^{\left(\frac{v_w}{\nu}\right)y} \end{aligned} \tag{F.5}$$

From the Falkner-Skan transform, $y = \eta\sqrt{\dfrac{\nu x}{u_e}}$, one can convert to the same coordinates as used in ACTITRANS2D:

$$\frac{v_w y}{\nu} = v_w \eta \sqrt{\frac{x}{u_e \nu}} = \frac{v_w \eta}{u_e}\sqrt{\frac{u_e x}{\nu}} = F\eta\sqrt{Re_x} \tag{F.6}$$

And hence:

$$\frac{u\left(\eta\right)}{u_\infty} = 1 - e^{\left(F\eta\sqrt{Re_x}\right)} \tag{F.7}$$

The displacement and momentum thickness are derived from their definitions to become:

$$\begin{aligned}
\delta^* &= \int_0^\infty e^{\left(\frac{v_w}{\nu}\right)y} dy = \left[\frac{\nu}{v_w} e^{\left(\frac{v_w}{\nu}\right)y}\right]_0^\infty = -\frac{\nu}{v_w} = -\frac{u_e x}{Re_x}\frac{1}{v_w} = -\frac{x}{Re_x F} \\
\theta &= \int_0^\infty \left(e^{\left(\frac{v_w}{\nu}\right)y} - e^{\left(\frac{2v_w}{\nu}\right)y}\right) dy = \left[\frac{\nu}{v_w} e^{\left(\frac{v_w}{\nu}\right)y} - \frac{\nu}{2v_w} e^{\left(\frac{2v_w}{\nu}\right)y}\right]_0^\infty = -\frac{1}{2}\frac{\nu}{v_w} = \frac{1}{2}\delta^*
\end{aligned} \tag{F.8}$$

For the wall shear stress and skin friction coefficient it follows that:

$$\begin{aligned}
\tau_w &= \mu \left(\frac{\partial u}{\partial y}\right)_{\text{wall}} = \mu \left(-\frac{v_w}{\nu} u_\infty e^{\left(\frac{v_w}{\nu}\right)y}\right)_{\text{wall}} = -\rho v_w u_\infty \\
C_f &= \frac{\tau_w}{\frac{1}{2}\rho u_\infty^2} = -\frac{v_w}{u_\infty} = -2F
\end{aligned} \tag{F.9}$$

Bibliography

I.H. Abbott and A.E. von Doenhoff. *Theory of Wing Sections*. Dover Publications Inc., New York, United States of America, first edition, 1959.

J.D. Anderson. Ludwig prandtl's boundary layer. *American Institute of Physics, Physics Today - S-0031-9228-0512-020-1*, 2005.

J.D. Anderson. *Fundamentals of Aerodynamics*. McGraw-Hill, New York, United States of America, fourth edition, 2007.

E.F. Bellobuono. *Aircraft Endurance Improvement through Turbulent Separation Control*. PhD thesis, University of Naples Federico II, 2006.

F. Bertagnolio, N. Sorensen, J. Johansen, and P. Fuglsang. Wind turbine airfoil catalogue. *Riso National Laboratory - Roskilde - Denmark, Riso-R-1280(EN)*, 2001.

J. Bink. Boundary layer suction on wind turbine blades, experimental validation of the feasibility study. *Actiflow B.V., Internal Report*, 2010.

M. Birsanu. Aerodynamic tip design of a wind turbine equipped with boundary layer suction. Master's thesis, Delft University of Technology, 2011.

R. Campe. A two-dimensional model for the conceptual design of a lfc equipped sailplane. Master's thesis, Delft University of Technology, 2004.

T. Cebeci. *An Engineering Approach to the Calculation of Aerodynamic Flows*. Horizons Publishing, Long Beach, California, United States, first edition, 1999.

T. Cebeci. *Convective Heat Transfer*. Horizons Publishing, Long Beach, California, United States, second edition, 2002.

T. Cebeci. *Turbulence Models and their Application*. Horizons Publishing, Long Beach, California, United States, first edition, 2003.

T. Cebeci. *Analysis of Turbulent Flows*. Elsevier Ltd., Oxford, United Kingdom, second edition, 2004a.

T. Cebeci. *Stability and Transition: Theory and Application*. Horizons Publishing, Long Beach, California, United States, first edition, 2004b.

T. Cebeci and P. Bradshaw. *Momentum Transfer in Boundary Layers*. Hemisphere Publishing Corporation, Washington, United States of America, first edition, 1977.

T. Cebeci and J. Cousteix. *Modeling and Computation of Boundary-Layer flows*. Horizons Publishing, Long Beach, California, United States, second edition, 2005.

T. Cebeci, M. Platzer, H. Chen, K. Chang, and J.P. Shao. *Analysis of Low-Speed Unsteady Airfoil Flows*. Horizons Publishing, Long Beach, California, United States, first edition, 2005a.

T. Cebeci, J.P. Shao, F. Kafyeke, and E. Laurendeau. *Computational Fluid Dynamics for Engineers*. Horizons Publishing, Long Beach, California, United States, first edition, 2005b.

T. Cebeci and A.M.O. Smith. *Analysis of Turbulent Boundary Layers*. Academic Press, New York, San Francisco, London, first edition, 1974.

D. Coles. The law of the wake in the turbulent boundary layer. *Journal of Fluid Mechanics, vol. I, pages 191-226*, 1956.

G. de Oliveira. A novel approach to wind turbine airfoil design with boundary layer suction. Master's thesis, Delft University of Technology, 2011.

M. Drela. *Two-Dimensional Transonic Aerodynamic Design and Analysis using the Euler Equations*. PhD thesis, Massachusetts Institute of Technology, 1985.

M. Drela. Integral boundary layer formulation for blunt trailing edges. *American Institute of Aeronautics and Astronautics, 89-2166-CP*, 1989a.

M. Drela. Xfoil: An analysis and design system for low reynolds number airfoils. *Springer-Verlag - lecture notes in engineering 54*, 1989b.

A. Favre, R. Dumas, and E. Verollet. *Couche Limite sur Paroi Plane Poreus avec Aspiration*. Magasin C. T. O., Avenue de la Porte-d'Issy 2, Paris, first edition, 1961.

C. Ferreira. Implementation of boundary layer suction in xfoil and application of suction powered by solar cells at high performance sailplanes. Master's thesis, Delft University of Technology, 2002.

J.H. Ferziger and M. Perić. *Computational Methods for Fluid Dynamics*. Springer, Germany, third edition, 2002.

M. Gad-el-Hak. *Flow Control*. Cambridge University Press., Cambridge, United Kingdom, first edition, 2000.

M.R. Head. Entrainment in the turbulent boundary layer. *Aeronautical Research Council - Reports and Memoranda No. 1352*, 1960.

S.F. Hoerner. *Fluid-Dynamic Drag*. Hoerner Fluid Dynamics, California, United States, first edition, 1965.

R. Iglisch. Exact calculation of laminar boundary layer in longitudinal flow over a flat plate with homogeneous suction. *National Advisory Committee for Aeronautics - Technical Memorandum No. 1205*, 1949.

W.M. Kays, M.E. Crawford, and B. Weigand. *Convective Heat and Mass Transfer*. McGraw-Hill, New York, United States, fourth edition, 2005.

W.M. Kays and R.J. Moffat. The behaviour of transpired turbulent boundary layers. *Department of Mechanical Engineering - Stanford University, HMT-20*, 1975.

W.M. Kays, R.J. Moffat, and W.H. Thielbahr. Heat transfer to the highly accelerated turbulent boundary layer with and without mass addition. *Department of Mechanical Engineering - Stanford University, HMT-6*, 1969.

K. Masatsuka. *I do like CFD, VOL.1*. Katate Masatsuka, 2009.

J. McQuaid. Experiments on incompressible turbulent boundary layers with distributed injection. *Aeronautical Research Council - Reports and Memoranda No. 3549*, 1967.

A. A. Merchant. Design and analysis of supercritical airfoils with boundary layer suction. Master's thesis, Massachusetts Institute of Technology, 1996.

S. B. Pope. *Turbulent Flows*. Cambridge University Press, Cambridge, United Kingdom, first edition, 2000.

L. Prandtl. Motion of fluids with very little viscosity. *National Advisory Committee for Aeronautics - Technical Memorandum No. 452*, 1904.

H. Schlichting and K. Gersten. *Boundary Layer Theory*. Springer, Europe, eight edition, 2000.

E.L.M. Terry. Extension of the aerodynamic design program MSES for the simulation of boundary layer suction. Master's thesis, Delft University of Technology, 2004.

N.C.A. van den Berg. Two-dimensional turbulent boundary layer with distributed transpiration. *Literature Research. Delft University of Technology*, 2011.

L.L.M. Veldhuis. *Aircraft Aerodynamics Primer*. Lecture Notes AE4130 Aircraft Aerodynamics, Delft University of Technology, 2010.

A.E.P. Veldman. *Boundary Layers in Fluid Dynamics*. Lecture Notes in Applied Mathematics, University of Groningen, 2010.

A.R. Wazzan, C. Gazley Jr., and A.M.O. Smith. The $\mathrm{H}-\mathrm{Re}_x$ method for predicting transition. *RAND paper P-6581*, 1988.

F.M. White. *Viscous Fluid Flow*. McGraw-Hill, New York, United States, third edition, 2006.

L. Zwang. Boundary layer suction on a horizontal axis wind turbine. Master's thesis, Delft University of Technology, 2009.